Royal Holloway University of London

Theoretical and experimental study of the electronic structure of FeSe

---

Luke Charles Rhodes

A thesis submitted for the degree of doctor of philosophy

Declaration

I, Luke Charles Rhodes, hereby declare that this thesis and the work presented in it is entirely my own. Where I have consulted the work of others, this is always clearly stated.

Signed:
Date:

To my wife, Emma.

Acknowledgements

First, I would like to thank my supervisors, Matthias Eschrig and Timur Kim, for their endless help and guidance over the past three years.

I would like to acknowledge insightful discussions on the iron-based superconductors with Swagata Acharya, Lara Benfatto, Pabitra Biswas, Jakob Böeker, Sergey Borisenko, Matthew Bristow, Véronique Bruoet, Cephise Cacho, Andrey Chubukov, Amalia Coldea, Piers Coleman, Pavel Dudin, Daniil Evtushinsky, Frédéric Hardy, Tetsuo Hanaguri, Hideaki Iwasawa, Laura Fanfarillo, Rafael Fernandes, Peter Hirschfeld, Moritz Hoesch, Sungwon Jung, Phil D. C. King, Andreas Kreisel, Hiroshi Kontani, Benjamin Parrett, Pascal Reiss, Vincent Sacksteader, Takahashi Shibauichi, Christopher Trainer, Roser Valenti, Mark Van Schilfgaarde, Pavel Volkov, Peter Wahl and Chi Ming Yim who helped me build a greater understanding of the complicated field of the iron-based superconductors.

I wish to thank Amir Haghigirad for providing the crystals of FeSe, without which this thesis would not have been possible, and Saicharan Aswartham, Igor Morozov and Bernd Büchner for providing the crystals of NaFeAs.

Finally, I wish to express my thanks to Matthew Watson. His knowledge and insight had a large impact on the results and conclusions presented here.

Abstract

This thesis aims to study the superconducting properties of the iron-based superconductor FeSe by closely combining theoretical methods with data obtained from angle-resolved photoemission spectroscopy (ARPES).

In order to understand the unconventional superconducting state below $T_c = 8$ K, we first study the electronic structure of the normal state. Conventional *ab-intio* methods can only provide qualitative information on the electronic structure of the iron-based superconductors. We overcome this limitation by optimising the hopping parameters of a tight binding model directly to ARPES data of the tetragonal phase of FeSe at 100 K. This quantitatively accurate model of FeSe is then used to predict a large temperature dependence of the chemical potential within this system, which we confirm via ARPES measurements.

We then modify this tight binding model to account for the C_4 symmetry breaking effect of the nematic phase of FeSe, which occurs below $T_s = 90$ K. By performing a detailed study of ARPES data measuring the nematic state, we determine an order parameter which can quantitatively account for the magnitude and symmetry of the band shifts observed as the material is cooled below T_s. We also find that whilst theoretical models of FeSe suggest a Fermi surface that consists of one hole pocket and two electron pockets, only one of these electron pockets is detected below T_s within ARPES measurements of detwinned crystals. A similar phenomenon is also observed in NaFeAs. We then find additional evidence supporting this interpretation of FeSe by modelling Quasiparticle Interference experiments and comparing with experimental data.

We end by performing ARPES measurements on the superconducting gap of FeSe. We find a highly anisotropic gap structure which is qualitatively consistent with a pairing mechanism involving spin fluctuations. To support this interpretation, we model the momentum dependence of the superconducting gap using the ARPES-based tight binding model derived in the previous chapters. By using a model that only includes one hole pocket and one electron pocket, we obtain excellent agreement with the experimental results.

This thesis consists of a complete study of the electronic structure of bulk FeSe and provides detailed information and insight into the tetragonal, nematic and superconducting state of FeSe.

Publications

Below is a list of publications that I have personally contributed to during the course of this PhD. A "*" indicates that I was the first author.

Chapter 3

* "*Strongly enhanced temperature dependence of the chemical potential in FeSe*" PRB, **95**, 19511 (2017)

Chapter 4

– "*Evidence for unidirectional nematic bond ordering in FeSe*" PRB, **94**, 201107(R) (2016)

– "*Electronic anisotropies revealed by detwinned angle-resolved photoemission spectroscopy measurements of FeSe*" New J. Phys., **19**, 103021 (2017)

– "*Three-dimensional electronic structure of the nematic and antiferromagnetic phases of NaFeAs from detwinned angle-resolved photoemission spectroscopy*" PRB, **97**, 035134 (2018)

Chapter 5

* "*Finite k_z states in the Quasiparticle Interference measurements of FeSe*" - To be submitted

Chapter 6

* "*Scaling of the superconducting gap with orbital character in FeSe*" PRB, **98**, 180503(R) (2018)

Other

– "*Probing the reconstructed Fermi surface of antiferromagnetic $BaFe_2As_2$ in one domain*" - Submitted (2019) arXiv:1902.10266

Contents

1 | Introduction

Superconductivity, the phenomenon of a zero resistance phase of matter, has the potential to radically transform our capacity to generate, transport and use electrical power. Below a critical temperature, T_c, a superconducting material will conduct electricity without energy dissipation and therefore, in certain materials, can produce large magnetic fields without additionally generating heat.

Applications for these materials are numerous, ranging from high speed levitating trains [1] to the development of particle accelerators [2]. Some of the most notable achievements include the creation of Nuclear Magnetic Resonance (NMR), for chemical research and drug discovery [3], Magnetic Resonance Imaging (MRI) in healthcare [4] and the development of extremely sensitive magnetometry for the study of fundamental condensed matter physics [5]. On top of this non-extensive list of current applications, superconducting materials will be essential for the future development of nuclear fusion reactors [6], quantum computers [7] and loss free energy storage [8].

There is, however, one major challenge greatly limiting the use of superconducting materials. The highly desirable properties are generally only exhibited at very low temperatures, with most commercial superconducting materials having a T_c between 10 and 40 K [9, 10]. The requirement of such a low temperature greatly limits the areas in which these materials can be applied, as well as making the devices costly to keep cool. One of the main goals of condensed matter physics is to develop a material which can exhibit superconductivity at or above room temperature. Whilst this has not yet been achieved, there is currently no theoretical upper limit on the maximum temperature at which superconductivity can be exhibited [11] and thus the search continues.

In this thesis, I will continue the study of superconductivity by taking a close look at the family of materials known as the iron-based superconductors. Discovered in 2008, this group of iron-pnictide or iron-chalcogenide materials exhibit a wide range of superconducting transition temperatures, between 0-100 K [12], and appear to be

governed by a form of superconductivity that differs from most conventional superconducting materials [13]. I will focus on one of the simplest iron-based superconductors, FeSe. By studying the experimental electronic structure of this material in detail, I will be able to develop a quantitatively accurate theoretical description of this system. Then, by combining both theoretical calculations and experimental measurements on the electronic structure and superconducting gap of FeSe, I will present new insight into the nature of superconductivity within this material. This could eventually lead to a route for the development of stable superconductivity at higher temperatures.

1.1 Superconductivity

Superconductivity is centred around the concept of the Cooper pair. In the presence of an attractive interaction, two electrons close to the Fermi level, with opposite momentum and spin, can form an energetically favourable bound state [14]. The idea of a bound state arising from pairs of fermions was originally discussed by Leon Cooper in 1956 [14], and expanded on one year later by the nobel prize winning work of Bardeen, Cooper and Schrieffer (BCS) [15]. This work laid the foundation for the microscopic theory of superconductivity, providing a wave of clarity to a 40 year long mystery.

There are three characteristic features of superconductivity, which arise as a direct consequence of the Cooper pair; zero resistance, perfect diamagnetism and an energy gap in the density of states. The phenomenon of zero resistance was the first of these properties to be discovered, when Heike Kammerlingh Onnes cooled elemental mercury below $T_c = 4.15$ K in 1911 [16]. Onnes observed a smooth decrease of the resistivity of mercury with decreasing temperature, followed by a sudden disappearance of the resistance below T_c, as shown schematically in Fig 1.1(a).

The second universal feature of superconductivity is perfect diamagnetism. In 1933, Meissner and Ochsenfeld observed that cooling a superconductor below T_c would expel a magnetic field (**B**) from within the material [17], as shown in Fig. 1.1(b). This experimental result was made 20 years prior to the conceptualisation of the Cooper pair, yet was instrumental in the development of the theory. It solidified superconductivity as a true thermodynamical phase of matter, rather than a low temperature limit of a simple metal with perfect conductance. In the latter scenario, the surface of a material would be expected to produce Eddy currents, This would shield the bulk from any new external magnetic field, however, any intrinsic magnetisation already present in the sample would be expected to remain trapped inside. The observation of the expul-

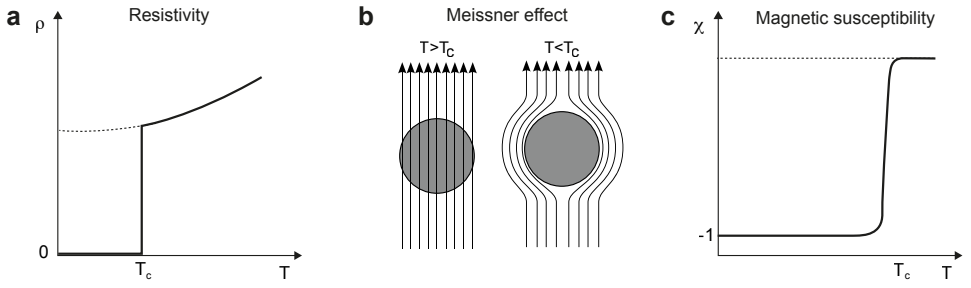

Figure 1.1: Macroscopic consequences of superconductivity. a) Cartoon of the resistivity (ρ) as a function of temperature indicating the transition to a zero resistance state at T_c. The thin dashed line describes a non-superconducting material. b) Cartoon of the Meissner effect, showing the expulsion of a magnetic field below T_c. c) Cartoon of the magnetic susceptibility, χ, as a function of temperature. At T_c, the value will change sharply to $\chi = -1$.

sion of the magnetic field, known as the Meissner effect, proved that the entire material had exhibited a phase transition, specifically to a diamagnetic state with $\mathbf{B} = 0$ [11]. Today, this is characterised by measuring a sharp change in the magnetic susceptibility at T_c to $\chi = -1$, as shown in Fig. 1.1(c). This dimensionless quantity, $\chi = \frac{\mathbf{M}}{\mathbf{H}}$, defines the ratio between the magnetisation of a material $\mathbf{M}$, and an external magnetic field $\mathbf{H}$, with $\mathbf{B} = \mu_0(\mathbf{M}+\mathbf{H})$[1]. For a perfect diamagnet, the bulk magnetisation of a sample is exactly opposite to the applied magnetic field.

This result led the brothers, Fritz and Heinz London, to propose the phenomenological London equation, relating a superconducting current, $\mathbf{J_s}$, to an external magnetic field [18],

$$\mathbf{J_s} = -\frac{n_s e}{m}\mathbf{A}. \tag{1.1}$$

Here, n_s is the density of superconducting electrons, e and m are the electron charge and mass, and $\mathbf{A}$ is the electromagnetic vector potential. London showed that if this equation was correct, then the magnetic field inside the superconducting material would fulfil the equation

$$\nabla^2\mathbf{B} = \frac{1}{\lambda^2}\mathbf{B}. \tag{1.2}$$

This can be solved to give $\mathbf{B}(\vec{r}) = B_0(\vec{r})e^{-\frac{\vec{r}}{\lambda}}$, such that the magnetic field will decay rapidly on entering a superconducting material, as observed by Meissner and Oschen-

[1] μ_0 is a constant describing the permeability of the vacuum.

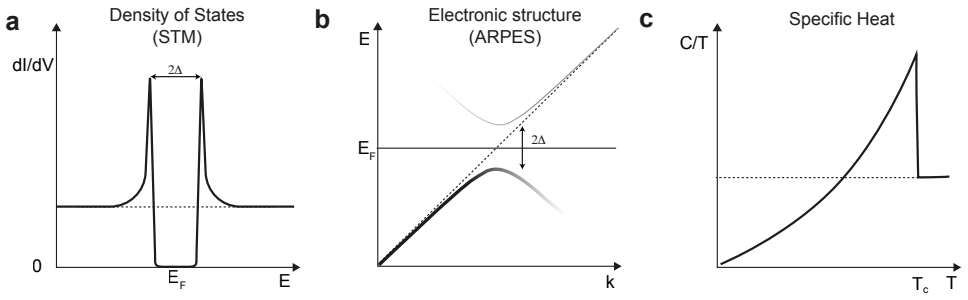

Figure 1.2: Consequences of an energy gap in experimental measurements. a) Cartoon of the density of states as a function of energy in the superconducting state as measured in a typical STS experiment. b) Cartoon of the electronic structure in the superconducting state showing the backfolding of the bands around E_F, note ARPES can only measure the occupied (lower) branch. c) Cartoon of the specific heat as a function of temperature, indicating a jump at T_c.

feld. The London equation also suggests a material specific penetration depth, λ, which could be measured experimentally [18].

Importantly, London pointed out that Eq. (1.1) is only true under the specific gauge $\nabla \cdot \mathbf{A} = 0$, which assumes that the wavefunction is only weakly affected by an external magnetic field [19]. Bardeen suggested that this gauge would imply the existence of an energy gap within the superconducting state [20]. Indeed, as Cooper pairs are a bound state, they do exhibit an energy gap (Δ) equivalent to the binding energy of the quasiparticle. As a result, microscopic Cooper pairs exhibit the macroscopic Meissner effect.

The presence of an energy gap also explains the sudden disappearance of resistivity at the onset of T_c. A finite energy is now required to produce excitations within the sample. As a consequence of this, low energy scattering pathways required for finite resistance are no longer available, and the material will exhibit a zero resistance state.

Generally, Δ can be measured using a variety of experimental methods, such as scanning tunnelling spectroscopy (STS), which probes the density of states around the Fermi level as shown in Fig. 1.2(a), and in photoemission via angle-resolved photoemission spectroscopy (ARPES) as shown in Fig. 1.2(b). Consequently, as the gap closing corresponds to a second order phase transition [15], the specific heat will also be expected to exhibit a jump at T_c, as shown in Fig. 1.2(c). This can also be used to characterise the superconducting transition.

The features discussed here are universal to all superconducting materials. They allow for a robust identification of a material in a superconducting state and provide a large number of macroscopic phenomena, which can be exploited for technological

applications. These measurable properties also provide a wide range of opportunities to study the specific details of the superconducting mechanism. This is crucial for the development of room temperature superconductivity, and today is the subject of intense research. In the next section, I will discuss the current understanding of the mechanisms with which Cooper pairs may form.

1.2 Pairing mechanisms

In the language of second quantisation[2], the Hamiltonian for a superconducting state can be defined as

$$\hat{H} = \hat{H}^0 + \hat{H}^{cp}, \tag{1.3}$$

$$\hat{H}^{cp} = \sum_{\mathbf{k}\mathbf{k}'} \Gamma(\mathbf{k},\mathbf{k}') c^{\dagger}_{\mathbf{k}\uparrow} c_{-\mathbf{k}\downarrow} c^{\dagger}_{\mathbf{k}'\downarrow} c_{-\mathbf{k}'\uparrow}. \tag{1.4}$$

Here, $\hat{H}^0$ describes the normal state Hamiltonian and $\hat{H}^{cp}$ describes the pair interaction, which gives rise to the formation of a Cooper pair. The operators $c^{\dagger}_{\mathbf{k}\sigma}$ and $c_{\mathbf{k}\sigma}$ describe the creation and annihilation of a state $\mathbf{k}$ with spin σ and $\Gamma(\mathbf{k},\mathbf{k}')$ describes the effective pairing interaction between two fermions with momentum $\mathbf{k}$ and $\mathbf{k}'$. The dominant question surrounding superconductivity is: *What is the form of the attractive interaction,* $\Gamma(\mathbf{k},\mathbf{k}')$*, that can facilitate the formation of Cooper pairs*? Typically, the answer to this question can be broken down into two categories; conventional superconductivity, governed by the electron-phonon interaction, and unconventional superconductivity, where the origin remains uncertain.

1.2.1 Conventional superconductivity

In the same paper that presented the consequences of Cooper pairs, Bardeen, Cooper and Schrieffer also proposed a theory for superconductivity mediated by phonons [15]. This idea was strongly influenced by the experimental observation of an isotope effect for elemental mercury, where T_c was observed to scale with the inverse of the square root of the isotopic mass, M,

$$T_c \propto \frac{1}{\sqrt{M}}. \tag{1.5}$$

[2]Discussed in section 2.1.

As the frequency of a phonon ω depends on the mass of the system, $\omega \propto \sqrt{\frac{k}{M}}$ where k is a spring constant, it followed that a superconducting mechanism dependent on phonons would also exhibit a similar mass scaling [21, 22]. Superconductivity would then be limited by the Debye frequency, ω_D, which defines the maximum energy of a phonon mode, and for simplicity is approximated to be momentum independent on the energy scale of $\varepsilon_k \approx \hbar\omega_D$ [14]. This allows for the pairing vertex to be simplified to

$$\Gamma(\mathbf{k},\mathbf{k}') = \begin{cases} V_{ph}, & |\varepsilon_k| < \hbar\omega_D \\ 0 & \text{otherwise.} \end{cases} \tag{1.6}$$

Here, V_{ph} is the electron-phonon coupling constant. This form makes (1.4) solvable, and analytical equations relating to properties of phonon-mediated superconductivity can be obtained. For example, at $T = 0$, the superconducting energy gap, Δ, is expected to obey the universal relation [15],

$$\frac{2\Delta}{k_B T_c} = 3.53, \tag{1.7}$$

regardless of the material composition. Here, k_B is the Boltzmann constant. In 1957 this result agreed extremely well for almost all known superconducting materials[3].

However, one of the most important equations derived from the BCS theory of superconductivity is

$$k_B T_c \approx \hbar\omega_D e^{-\frac{1}{N(0)V_{ph}}}. \tag{1.8}$$

This equation describes a superconducting transition temperature which is proportional to the magnitude of the Debye frequency, the density of states at the Fermi level, $N(0)$, and the electron-phonon interaction. The importance of this equation can not be understated, it provides a mathematical relationship between the superconducting transition temperature and external parameters as well as explain why conventional superconducting materials have a highly three dimensional cubic structure and a large density of states. It also suggests that lighter elements will have a larger T_c due to the inverse proportionality of ω_D and the mass of the ion [24]. Indeed, the intuition from this equation has culminated in the recent observation of superconductivity at $T_c = 203$ K in H_2S, under pressures exceeding 200 GPa [25], and $T_c = 260$ K in LaH_{10}, at 170 GPa [26, 27].

[3]Whilst Eq. (1.7) is only strictly true in the weak coupling limit, extensions to a strong coupling regime (i.e with large V_{ph}) have been derived which modifies the ratio to a universal curve [23].

The theoretical insight from conventional superconductivity is nothing short of remarkable and, thanks to modern technological improvements, suggests that superconductivity above 273 K may be reached within the coming years. However, the formation of light metallic hydrogen derivatives has so far only been possible under extreme pressure [28] and hence the applicability of room temperature superconductivity under a conventional phonon mediated mechanism remains limited. Luckily, there is another class of superconducting materials, which may be able to provide an alternative route to the room temperature superconductor.

1.2.2 Unconventional superconductivity

In 1979, superconductivity was discovered in the heavy fermion material $CeCu_2Si_2$ with a T_c of 0.5 K [29]. Whilst the temperature at which superconductivity occurred is relatively low, superconductivity had never before been observed in a strongly correlated material, nor in a material with a close lying magnetic instability. In fact these features were assumed to be detrimental to the phonon-mediated mechanism [15]. This was the first hint that other forms of superconductivity, beyond the phonon mediated mechanism, may be possible [30].

Interest in this field exploded with the discovery of superconductivity in copper oxide ceramic materials in 1986 [31]. These new materials, referred to generally as the cuprate superconductors, were formed of two-dimensional layered copper oxide sheets, and without doping were antiferromagnetic Mott insulators [32]. This is very distinct from the trends of phonon-based superconductors which were generally three-dimensional, non magnetic, metals. Excitingly, these materials exhibited T_c nearly an order of magnitude larger than conventional superconductors. Before this discovery, Nb_3Ge held the record for largest superconducting transition temperature with $T_c = 23.2$ K [33], yet the first discovered cuprate $Ba_xLa_{5-x}Cu_5O_{5(3-y)}$, measured a T_c of 30 K [31], which several months later was increased to 40.2 K under hydrostatic pressure [34]. Within a year $(Y_{1-x}Ba_x)_2CuO_{4-y}$ was reported with $T_c = 93$ K [35] and, in 1993, a Hg-Ba-Ca-Cu-O system boasted a T_c of 133 K at ambient pressure [36], which increased to 164 K under pressures of 30 GPa [37].

The cuprate materials appear to be in violation of many of the specific predictions made from phonon-mediated superconductivity. The isotope effect was observed to either negligibly alter T_c [38–40] or exhibit a shift largely dependent on the exact system and doping parameters [41]. Importantly, the theoretical gap to T_c ratio, suggested in Eq. (1.7), was much smaller than experimentally measured. $(Y_{1-x}Ba_x)_2CuO_{4-y}$, for

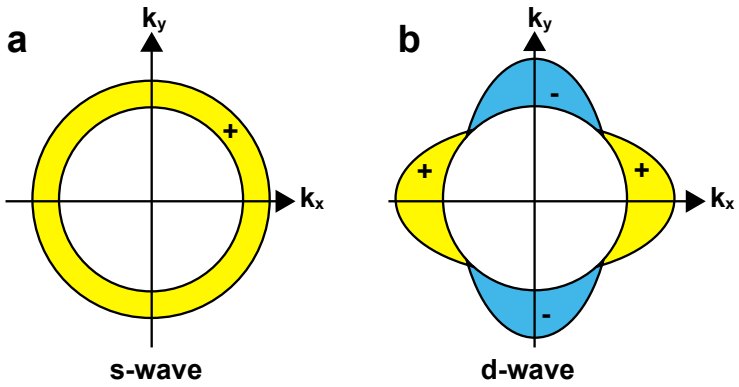

Figure 1.3: Comparison of the momentum dependence of the superconducting gap symmetry for a single band cuprate system. The Fermi surface in 2D is circular, described by the white circle. a) Momentum dependence of the superconducting gap describing an s-wave phonon-mediated mechanism of superconductivity. b) Momentum dependence of the superconducting gap describing a d-wave pairing symmetry. The yellow(+) and blue (-) regions indicate the phase of the superconducting order parameter.

example, exhibited $\frac{2\Delta_{max}}{k_B T_c} \approx 8$ [42], over twice as large as suggested for phonon mediated superconductors. Not only that, but the superconducting gap of the cuprates was discovered to be a momentum dependent quantity [43, 44], following the d-wave form,

$$\Delta(k_x, k_y) = \Delta_0[\cos(k_x) - \cos(k_y)]. \tag{1.9}$$

A cartoon of this is shown in Fig. 1.3. This form of pairing is very hard to reconcile with the isotropic, s-wave, gap suggested by phonon-mediated superconductivity [15].

The phase diagram of the cuprates, shown schematically in Fig. 1.4, also provides further evidence suggesting that these materials do not exhibit superconductivity purely from a phonon-mediated mechanism. Undoped cuprate materials are antiferromagnetic Mott insulators, which do not exhibit superconductivity at any temperature. However, upon doping with hole or electron carriers, this phase is quickly suppressed and a metallic system, which exhibits superconductivity, emerges. This produces a dome like feature with a maximum T_c at a critical doping value [45]. This is distinct from conventional phonon-based superconductors, which do not exhibit a large change in T_c from the addition or removal of carriers.

There is also experimental evidence for many other close lying competing phases in this region of phase space. A pseudogap state is observed below a critical doping value [46]. This region is characterised by a momentum dependent loss of coherent spec-

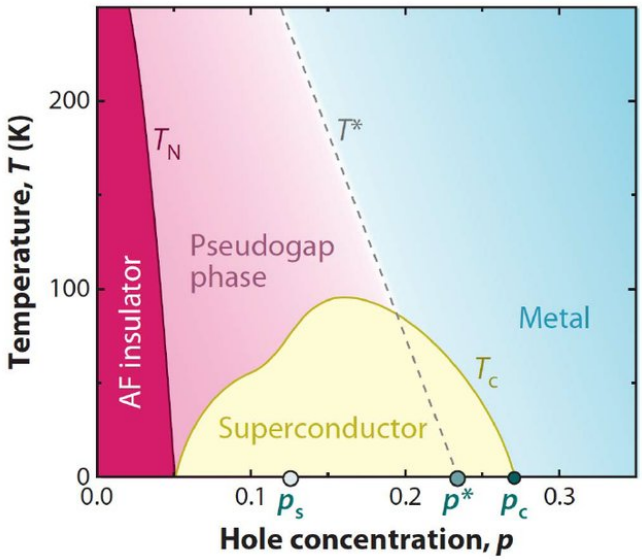

Figure 1.4: Cartoon phase diagram of the cuprate materials as a function of hole doping. Figure taken from Ref. [45].

tral weight, however, the microscopic origin of this phase is not currently understood [47]. On top of this, the observation of a charge density wave state [48], and a potential nematic, C_4 rotational symmetry breaking, state [49] have also been uncovered in close proximity to superconductivity, suggesting that many competing phases may influence the superconducting state. The observation of a superconducting dome, d-wave momentum dependence of the superconducting gap, and close lying magnetism all suggest that an alternative mechanism of superconductivity is at work.

1.2.3 Spin fluctuation theory

Many theories have been proposed to describe the exotic complexity of the cuprate phase diagram and capture the large values of T_c. These include using Van-Hove singularities to enhance the density of states at the Fermi level [50], the concept of a resonating valence bond [51] and the concept of electron-exciton coupling [11].

A leading theory for the rich phase diagram of the cuprate materials as a function of doping is based on the concept of fluctuating spins [30, 52]. Superconductivity only occurs in the cuprates once long range $\mathbf{Q} = (\pi, \pi)$ antiferromagnetic ordering has been suppressed. At doping values just beyond this critical point, although the spins of the fermions will not be static, they will have a tendency to fluctuate strongly in the direction of the magnetic ordering vector [53]. This has been proposed as a potential

mechanism for the creation of Cooper pairs [30].

Strong spin fluctuations would not be specific to superconductivity, but would more generally play a role in other features of the cuprate phase diagram. Phenomenologically, the spin susceptibility, which defines the tendency of a spin to fluctuate close to a magnetic instability, can be written as [54]

$$\chi(\mathbf{q},\omega) = \frac{\chi_{\mathbf{Q}}}{1+(\mathbf{Q}-\mathbf{q})\xi^2(T) - \frac{i\omega}{\omega_{sf}}}. \tag{1.10}$$

This equation describes a spin susceptibility function that is peaked at a momentum of $\mathbf{q} = \mathbf{Q}$ which at $\omega = 0$ exhibits a maximum susceptibility, $\chi_{\mathbf{Q}}$. The quantities ω_{sf} and $\xi^2(T)$ describe a frequency and length cutoff for the corresponding spin fluctuations. This phenomenological form successfully reproduces key features of the phase diagram of the cuprates. This includes the emergence of superconductivity and suppression of antiferromagnetism on doping [55], the inequivalence of the phase diagram for hole and electron doped systems [56, 57] and provides an explanation for T-linear resistivity observed in these materials up to temperatures as high as 700 K [56].

The equation for the pairing interaction via a spin fluctuation mediated mechanism can then be derived on the assumption that $\frac{\omega_{sf}}{E_F}$ is a small quantity [58][4]. Under this assumption, the pairing interaction takes the form

$$\Gamma(\mathbf{k},\mathbf{k}') = \frac{3}{2}U^2\chi^S(\mathbf{k}-\mathbf{k}') - \frac{1}{2}U^2\chi^C(\mathbf{k}-\mathbf{k}') + U \tag{1.11}$$

Here, U defines the strength of the Coulomb repulsion and the spin susceptibility $\chi^{C/S}(\mathbf{q})$ is defined as

$$\chi^{C/S}(\mathbf{q}) = \frac{\chi(\mathbf{q})}{1 \pm U\chi(\mathbf{q})}. \tag{1.12}$$

This spin susceptibility, dressed by the Coulombic interaction, describes the susceptibility of the spins in the charge (C,+) or spin (S,-) channel. The pairing also takes place at $\omega = 0$. A derivation of this equation is presented in Appendix B, and discussed in Chapter 6. For a cuprate model, this pairing vertex successfully predicts a $d_{x^2-y^2}$ order parameter for the superconducting gap [59] and correctly describes a superconducting dome as a function of doping [60]. However, these results have remained primarily numerical, and a concrete set of equations similar to those defined for the conventional superconductors has proved much harder to obtain. This is due to the

[4] where E_F is the Fermi energy

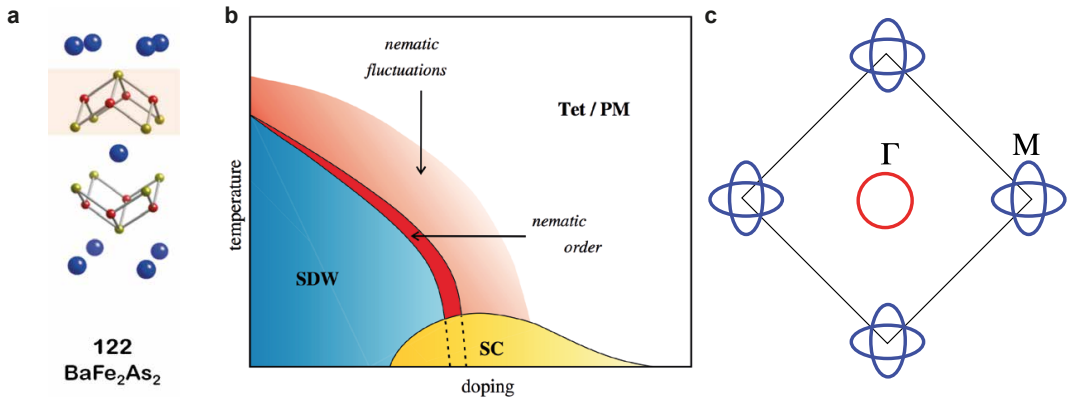

Figure 1.5: Properties of the iron-based superconductors. a) Crystal structure of $BaFe_2As_2$. Blue atoms are Ba, red atoms are Fe and yellow atoms are As. Figure taken from ref. [68]. b) Schematic phase diagram for electron doped $BaFe_2As_2$. Indicating the antiferromagnetic state (blue), the C_4 symmetry breaking nematic transition (red) and the superconducting state (yellow). The C_4 symmetric, paramagnetic region is also shown in white. Figure taken from Ref. [69]. c) Typical electronic structure of the iron-based superconductors, showing the electron pockets in blue and the hole pocket in red.

momentum dependent nature of the pairing vertex which strongly depends on the electronic states at the Fermi level. The spin fluctuation scenario also does not currently offer a description for the pseudogap state, which appears to be intrinsically related to superconductivity [46]. Whilst spin fluctuation theory successfully captures key experimental observables of the cuprate superconductors, more evidence is required to confirm if this mechanism is truly mediating superconductivity in the cuprate systems.

1.3 Iron-based superconductors

In 2008, a new family of superconductors were discovered, again with anomalously high T_c compared to most conventional phonon-based superconductors. Whilst these iron-based superconductors have so far not broken the 164 K record of superconductivity in the cuprates, they still show large values of T_c compared to other phonon-based superconductors. For example, $La(O_{1-x}F_x)FeAs$ exhibits a T_c of 28 K [61] and SmFeAsF has $T_c = 54$ K [62]. More creative manipulation even suggest that a monolayer of FeSe on $SrTiO_3$ can exhibit a $T_c \approx 100$ K[5].

[5] There is some controversy about the exact value of the superconducting transition in this system, ARPES measurements suggest $T_c \sim 65$ K [63–65]. However a single four point probe experiment suggests 100 K [66]. A discussion on this discrepancy is presented in Ref. [67].

On first glance, these new iron-based superconductors appear to share many similarities with the cuprates, including a 2D layered structure (Fig. 1.5(a)), an antiferromagnetic parent state and a superconducting dome that emerges on suppression of the magnetic state with doping (Fig. 1.5(b)). Along with the unusually high T_c, it seemed plausible that these materials could also be governed by a similar underling mechanism of superconductivity.

However, when one looks a bit closer at the iron-based superconductors, several key differences become apparent. The parent phase describes a semi-metal, rather than a Mott insulator, and exhibits striped $(\pi, 0)$ antiferromagnetic ordering rather than the Neel (π, π) antiferromagnetism observed in the cuprates [12]. The crystal structure, despite being layered, is only quasi-2D with the pnictide or chalcogenide atom sitting above or below the Fe-plane. Finally, the electronic structure no longer consists of one large $3d_{x^2-y^2}$ spherical Fermi surface, but rather of multiple localised hole and electron pockets, with $3d_{xz}$, $3d_{yz}$ or $3d_{xy}$ orbital character (Fig. 1.5(c)).

These differences, rather than being a hindrance, actually provide a fantastic opportunity to get to the heart of unconventional superconductivity. If the mechanism between these two families of materials is indeed the same, then the similarities and contrasts between the two sets of superconducting materials may provide additional information regarding the key ingredients of the unconventional superconducting mechanism [13].

The phase diagram, shown of Fig. 1.5(b), is typical of several different iron-based superconductors, such as NaFeAs and $BaFe_2As_2$ [69], and appears strongly reminiscent of the cuprate phase diagram of Fig. 1.4. A marked suppression of antiferromagnetism upon doping and the subsequent emergence of a superconducting dome is observed. The additional phases that are detected in the cuprate materials, such as the pseudogap state, are not present in these materials. Instead, a new nematic phase is often exhibited. This phase breaks the C_4 symmetry of the lattice and induces large anisotropic responses in the underlying electronic properties [70, 71]. Generally, the nematic phase occurs at temperatures either coinciding with, or at temperatures slightly higher than, the antiferromagnetic phase transition, and is strongly susceptible to doping. Whilst this initially suggests that nematicity is somehow related to the magnetic phase, the coexistence of magnetism and nematicity is not observed in FeSe, which exhibits a well defined nematic transition but no long range magnetic ordering [72]. The origin of this phase remains under debate [73] and will be studied in this thesis.

A major strength of the iron-based superconductors is the diverse phase space that

can be explored by chemical engineering. Whilst the typical systems of NaFeAs and $BaFe_2As_2$ exhibit superconductivity, nematicity and magnetism all within a single system, other iron-based superconductors have been synthesised which appear to probe individual sections of these phases. LiFeAs, for example, exhibits superconductivity at $T_c = 18\ K$ without the need for doping and, importantly, does not experience magnetic ordering or nematic ordering down to the lowest measured temperatures [74]. This material can then be probed to study superconductivity in the iron-based superconductors without additional competing phases. FeSe also does not exhibit long range magnetic ordering [75], but does show a well defined nematic transition at $T_s = 90$ K and exhibits superconductivity below $T_c = 8$ K. This provides a perfect system to study the nematic phase and it's interplay with superconductivity. The iron based superconductors have therefore created the opportunity to dissect the rich and varied phase space that occurs in close proximity to an unusual mechanism of superconductivity.

1.3.1 LiFeAs

LiFeAs is an ideal system for studying the superconducting properties of the iron-based superconductors. This material has a relatively high T_c of 18 K and exhibits no competing phases. ARPES measurements, shown in Fig. 1.6(a), describe a Fermi surface consisting of two hole pockets at the centre of the Brillouin zone; a large d_{xy} pocket and a small $d_{xz/yz}$ pocket, and two overlapping ellipses at the corner of the Brillouin zone [79]. The superconducting gap, measured as a function of angle around each of the four pockets, revealed a C_4 symmetric gap structure, with the largest gap ($\Delta \approx 5$ meV) residing on the smallest $d_{xz/yz}$ hole pocket. This is shown in Fig. 1.6(b). Unlike the cuprates, no nodes were detected, suggesting that the gap was not d-wave in symmetry [77]. However, it was theoretically proposed that there could be a sign change between the hole and electron pockets [80] which could arise as a consequence of an unconventional superconducting mechanism.

As the Fermi surface consists of multiple strongly correlated quasiparticle bands, an accurate model of the electronic structure has proved difficult to obtain. Density Functional Theory (DFT) calculations of LiFeAs are in qualitative agreement with the size and shape of the experimental electron-like pockets, as well as the large d_{xy} hole pocket [81–83]. However, the small $d_{xz/yz}$ hole pocket, with the largest superconducting gap, is greatly overestimated.

Attempts to overcome this discrepancy have been attempted by several alternative *ab-initio* calculations. The framework of DFT + Dynamic mean field theory (DMFT)

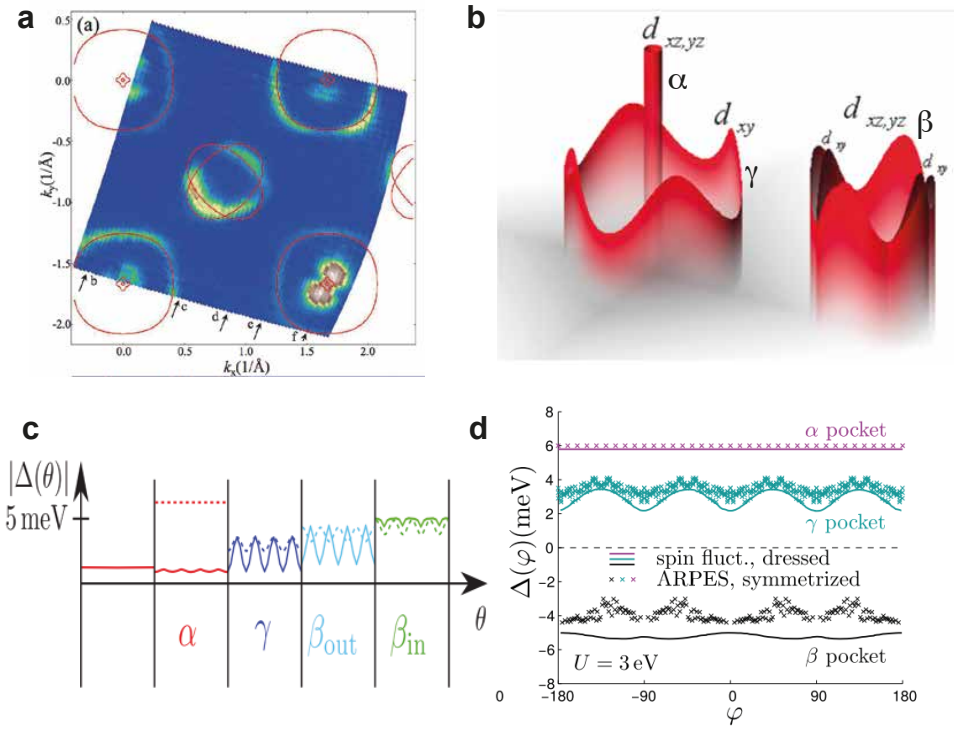

Figure 1.6: Superconducting properties of LiFeAs. a) Fermi surface map of LiFeAs taken from Ref. [76]. b) Schematic of the momentum dependence of the superconducting gap for the two hole bands (left) and two electron bands (right). Taken from Ref. [77]. The height indicates the size of the gap. c) Results of the calculated momentum dependence of the superconducting gap from Ref. [76]. The values are presented as a function of angle for the hole bands (α and γ) and the two electron bands (β_{out} and β_{in}). The dotted lines are experimental results from Ref. [77]. d) Revised calculation of the momentum dependence of the superconducting gap from Ref. [78], taking into account quasiparticle renormalisation.

has been attempted. This calculation is an extension of DFT, which captures local spin correlations. This approach was able to describe some of the bandwidth renormalisation, associated with the Fe d-bands at low energies, but was unable to reproduce the small size of one of the hole pockets [84–86]. Quasiparticle Self-consistent GW (QSGW) calculations have also been performed. This approach does not include local spin correlations, but does take into account non-local electron-electron correlations. This approach was partially able to account for the reduction in size of one of the hole pockets, compared to DFT, however, it could not fully account for the bandwidth renormalisation at low energies [87, 88]. Despite the various attempts to describe the electronic structure of LiFeAs, a model which can quantitatively captured the band

dispersions measured in experiment has, so far, not been generated from first principle theories.

To overcome this problem, Wang *et. al.* optimised a tight binding model directly to ARPES data of LiFeAs [76]. This approach bypassed the discrepancy between theory and experiment and provided a method to phenomenologically describe the superconducting properties of the system. Wang *et. al.* then calculated the momentum dependence of the superconducting gap using a multi-orbital extension of the spin fluctuation pairing vertex described in Eq. (1.11) [89]. Their results are shown in Fig. 1.6(c). They obtain qualitative agreement with the experimental results and produce a superconducting gap with s^{+-} symmetry. This suggests that whilst there are no nodes at the Fermi level, the superconducting gap may change sign between the hole and electron pocket, as previously suggested by Mazin *et. al.* [80]. However, the spin fluctuation scenario overestimated the anisotropy of the gap function for the individual bands, and greatly underestimated the relative magnitude of the gap at the inner $d_{xz/yz}$ hole pocket.

There are several potential reasons for this discrepancy, which have been debated within the literature. The first, was the neglection of spin orbit coupling in the tight binding model [76]. This consequence ensured that an extra hole band was present in the calculations, which is not observed experimentally [90]. Saito *et. al.* [91] pointed out that including a dressed electron phonon interaction into the spin fluctuation pairing, referred to as “orbital fluctuations", can result in the inner hole pocket exhibiting the largest gap. However, this approach suggests that the gap would not exhibit a sign change between pockets, i.e the gap will have s^{++} symmetry. Whilst ARPES is not sensitive to the sign of the gap, recent Bogoliubov Quasiparticle Interference (BQPI) experiments found evidence to support the notion of a sign change in LiFeAs [92, 93]. This suggests that the orbital fluctuation scenario may not be the correct interpretation [94]. Finally, Kreisel et. al. [78] suggested that the phenomenological tight binding model employed simply needed to take into account the orbital dependent quasiparticle weights from the strong coupling renormalisation. In this scenario, by reducing the quasiparticle weight of the bands from unity in the original calculation, of Fig. 1.6(c), to 0.5493 for the d_{xy} orbital and 0.5952 for the d_{xz} and d_{yz} orbitals, the gap function for each band can be almost completely reproduced[6].This is shown in Fig. 1.6(d). These numbers appear to be in reasonable agreement with DFT + DMFT studies [84]

[6]What is important here is not actually the value of Z, but the relative ratio of Z between the orbitals [78].

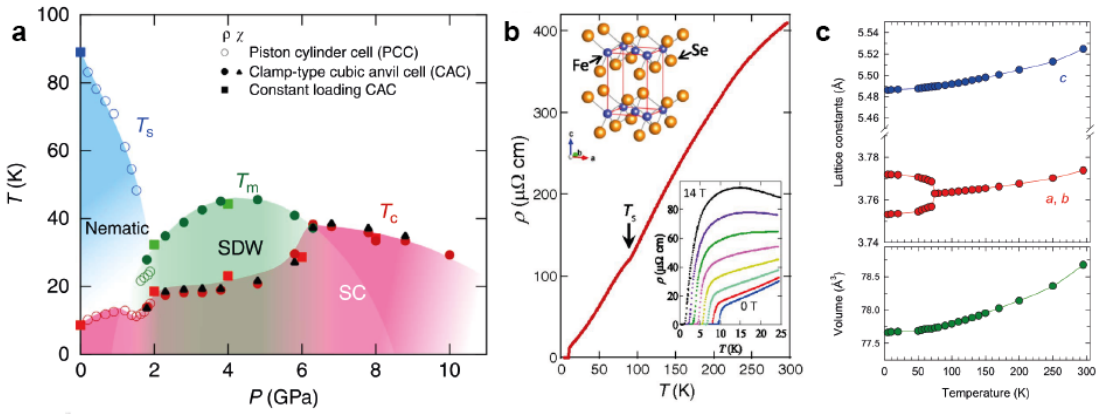

Figure 1.7: Physical properties of FeSe and it's electronic structure. a) Pressure vs temperature phase diagram of FeSe. Reproduced from Ref. [97]. b) Resistivity of FeSe as a function of temperature showing the nematic transition at 90 K, adapted from Ref. [98]. c) Lattice constants of FeSe as a function of temperature, blue describes the c-axis, red describes the a and b-axis, and green describes the total volume of the unit cell. Reproduced from ref. [99]. d) Fermi surface of FeSe predicted by DFT [100], e) Predicted by DFT + DMFT [101] and c) measured in ARPES [102].

and appear to be consistent with ARPES measurements, where the t_{2g} orbitals all have similar coherence [77]. However, these values discussed are not systematic, and are obtained to fit the experiment. A more rigorous calculation is still required to support this argument. As will be discussed in Chapter 5, this methodology does not hold for nematic materials such as FeSe [95].

The results for LiFeAs are tentatively in favour of a spin fluctuation pairing scenario, correctly capturing the sign change between the hole and electron pocket in the superconducting state as determined by BQPI. However, the fine details of this system have proved complicated to model. It is therefore important to study alternative systems, to see if more information related to the nature of superconductivity can be determined. For this reason I turn our attention towards FeSe. FeSe also does not exhibit long range magnetic order, however, it does experience a tetragonal to orthorhombic structural transition at 90 K. As a consequence, the C_4 symmetry of the crystal is broken, inducing relatively large changes to the electronic properties [72]. This effect is known to alter the electronic structure of FeSe [96], and will have to be carefully studied before it is possible to understand the superconducting state.

1.3.2 FeSe

The PbO-type crystal structure of FeSe, discovered in 2008 [103], exhibits superconductivity below $T_c \approx 8$ K and has been the subject of intensive study [104–107].

One reason for this is the highly tunable nature of superconductivity within this material. For example, under 8.9 GPa of applied pressure, T_c is observed to increase to a maximum value of 36.7 K [108]. This is shown in a pressure vs temperature phase diagram of Fig. 1.7(a). Intercalation with organic amide molecules [109], or alkali metals [110, 111], can also enhance T_c to the region of 30-46 K, depending on the exact chemical composition. On top of this, monolayers of FeSe, grown on $SrTiO_3$ exhibit a superconducting transition temperature of $T_c = 65$ K [67, 112, 113], 8 times larger than bulk FeSe. It is currently not understood why this material exhibits such a dramatic sensitivity of T_c, however, unlocking these mysteries may hold the key for understanding high temperature superconductivity.

Another reason for the extensive research into FeSe is that it provides an ideal system to probe the nematic state of the iron-based superconductors. At $T_s = 90$ K, a structural transition between a tetragonal, $P4/nmm$, and orthorhombic, $Cmma$, crystal structure is observed in bulk FeSe [99]. This is seen in the resistivity vs temperature plot of FeSe in Fig. 1.7(b) and the lattice constants measured by x-ray diffraction in Fig. 1.7(c). This structural transition, despite only inducing a small rotational symmetry breaking anisotropy in the lattice constants, is known to exhibit a large anisotropic response to the electron properties of the system, which has been measured in the resistivity of FeSe [114] and in the experimental electronic structure [96].

In many iron-based superconductors this structural transition is often accompanied by the stabilisation of long range striped antiferromagnetic ordering [73], however, FeSe does not exhibit long range magnetic order at any temperature under ambient pressure [75]. Thus this material provides an opportunity to probe the effects of the nematic phase, without the additional complication of magnetic ordering [72].

Despite the lack of long range ordering, magnetism is still important in FeSe. Neutron scattering experiments have revealed the presence of local spin fluctuations in both the tetragonal and orthorhombic state [115, 116], which implies a close lying magnetic phase. A spin density wave is observed in FeSe under pressure, where the nematic phase is suppressed and a magnetism emerges at pressures exceeding 2 GPa [97]. This spin density wave phase exhibits a dome like feature in the pressure vs temperature phase diagram, as shown in Fig. 1.7(a), and on the suppression of the magnetically ordered phase above 8 GPa gives rise to the enhanced values of T_c [97]. This property

suggests that despite the absence of long range magnetism, spin fluctuations may still play an important role in the superconducting mechanism.

At the time of starting this PhD, high quality single crystals of FeSe had just become available [75], with the first ARPES measurements of FeSe being performed in 2014 by Maletz *et. al.* [117]. However, the final details of the electronic structure, such as the evolution of the bands due to the nematic phase, was still being debated [100, 118–120]. Despite this, it was already clear that DFT, and extensions such as DFT + DMFT, overestimated the size and energy scales of the experimental band dispersions [101, 117]. For this reason, a majority of the thesis will focus on uncovering the fine details of the electronic structure of FeSe, to establish a reliable model to study the superconducting state.

1.4 Outline of thesis

The structure of this thesis is as follows. In Chapter 2, I will discuss the theoretical tools used throughout this thesis as well as the experimental apparatus of ARPES. In Chapter 3, I will develop a quantitatively accurate tight binding model of FeSe in the tetragonal phase by directly optimising the hopping parameters to experimental ARPES data. In Chapter 4, I will study the rotational symmetry breaking effects of the nematic phase and the consequence this has on the electronic structure of FeSe. I will pay particular attention to the limitations of conventional ARPES experiments when it comes to studying orthorhombic crystals. In Chapter 5, I will study the electronic structure of the nematic phase of FeSe as probed by the independent technique of Quasiparticle Interference (QPI). I will compute the predicted QPI patterns of FeSe in the nematic state, using the model for the electronic structure developed in Chapter 4, and compare with the experimental literature. Finally, in Chapter 6, I will measure the superconducting gap of FeSe using ARPES. I will use the tight binding model developed throughout the previous chapters to calculate the momentum dependence of the superconducting gap of FeSe, assuming that superconductivity is mediated by spin fluctuations, and compare with the experimental result. We then conclude the results of this study in Chapter 7 and discuss future work.

2 | Theory and Methodology

2.1 Second quantisation

The language of second quantisation will be used throughout this thesis [121, 122]. It provides a framework which allows for a precise description of many body systems. In this section, I will present a brief overview of the properties of second quantisation which will be important in the following chapters.

Consider a generic wavefunction,

$$\Psi = \prod_{i}^{n} \psi_i, \tag{2.1}$$

where the total wavefunction, Ψ, is defined as the product of n single particle wavefunctions, ψ. Typically, for this to describe a physical system, the wavefunction must be carefully modified to account for the symmetries of fermions or bosons with respect to particle interchange [123]. In the language of second quantisation, however, all possible states in a many body system can be defined within a “Fock" space [124],

$$\Psi = |\phi_n, \phi_{n-1}, ..., \phi_2, \phi_1\rangle\,. \tag{2.2}$$

Here, each ϕ describes the occupation of a specific single particle state in a many body system. In the language of second quantisation, ϕ can either equal 0 or 1 depending on the occupation of the state. It is possible to then define operators, which can act on wavefunctions in Fock space to either create ($c^\dagger$) or annihilate (c) a particle in a given state,

$$\begin{aligned} c_1^\dagger\,|0\rangle &= |\phi_1\rangle\,, \\ c_1\,|\phi_1\rangle &= |0\rangle \\ c_2^\dagger c_1^\dagger\,|0\rangle &= |\phi_2, \phi_1\rangle\,. \end{aligned} \tag{2.3}$$

Here, $|0\rangle$ is written as a definition for the vacuum, or a completely empty Fock space. From this, it is possible to write the full wavefunction as

$$\Psi = \prod_i c_i^\dagger |0\rangle , \tag{2.4}$$

which is the product of the creation operators that define the i occupied states. In the case of fermionic systems, the creation and annihilation operators obey the anticommutator relations,

$$\{c_\alpha^\dagger, c_\beta\} = \delta_{\alpha\beta} \qquad \{c_\alpha, c_\beta\} = \{c_\alpha^\dagger, c_\beta^\dagger\} = 0. \tag{2.5}$$

These symmetries automatically account for the Pauli exclusion principle as it enforces $c_\alpha^\dagger c_\alpha^\dagger |\Phi\rangle = 0$. Finally, the number operator

$$n_\alpha |\phi_\alpha\rangle = c_\alpha^\dagger c_\alpha |\phi_\alpha\rangle = \begin{cases} 0 & \text{if state is empty} \\ 1 & \text{if state is occupied} \end{cases} \tag{2.6}$$

is a useful tool to define whether a given state is occupied or vacant. From these mathematical formalisms, it is possible to concisely describe many body phenomena such as conduction [125], magnetism [53], and superconductivity [15].

2.2 Tight binding framework

The tight binding model is one of the simplest mathematical descriptions available to model electronic transport in a metallic system. In the language of second quantisation a generic tight binding Hamiltonian may be written as

$$H = -\sum_{<i,j>} t_{ij}(c_i^\dagger c_j + c_j^\dagger c_i). \tag{2.7}$$

This Hamiltonian simply defines the process of a fermion “hopping" from state i to state j, or state j to state i. We define t_{ij} as positive such that the hopping process lowers the total energy of the system by the value t_{ij}. It is possible to calculate this hopping parameter via the matrix element of the Hamiltonian ($\hat{H}$),

$$t_{ij} = \langle \phi_i | \hat{H} | \phi_j \rangle . \tag{2.8}$$

As the overlap between two orbitals is spatially dependent, t_{ij} will be largest for nearest

neighbour hoppings, and decrease as the distance between the states increases. This will eventually become negligible at a given radial cutoff such that it is possible to accurately describe a metallic system with relatively few parameters.

As an example, consider a non-interacting one dimensional toy model with only nearest neighbour hopping,

$$H = -\sum_n t(c_n^\dagger c_{n+1} + c_{n+1}^\dagger c_n). \tag{2.9}$$

Here, n describes the atomic site index. It is possible to solve this equation in momentum space via Fourier transforming the creation and annihilation operators:

$$c_x^\dagger = \sum_k e^{-ikx} c_k^\dagger \tag{2.10}$$

$$c_x = \sum_k e^{ikx} c_k. \tag{2.11}$$

By substituting $x = na$, where a is the lattice constant, the Hamiltonian becomes

$$H = -t\sum_k e^{ika} c_k^\dagger c_k - t\sum_k e^{-ika} c_k^\dagger c_k = -2t\sum_k \cos(ka) c_k^\dagger c_k \tag{2.12}$$

Such that the band dispersion which describes this Hamiltonian is given by $E(k) = -2t\cos(ka)$. We therefore see that if electrons can freely hop between atomic sites, and the band is only partially filled, our system will be able to conduct without occurring an energy penalty. Whilst this is only a toy model to describe the properties of a simple 1D system, this formalism can be extended, using the work of Slater and Koster [125], to develop tight binding models which can describe hopping processes between multiple orbitals and specific crystal geometries. Such a model will be employed in this thesis, and will be discussed in Chapter 3.

2.3 Green's Functions

Suppose there exists a linear differential equation

$$Lu(\mathbf{x}) = f(\mathbf{x}), \tag{2.13}$$

where L is a linear differential operator, $f(\mathbf{x})$ is a known function and $u(\mathbf{x})$ is unknown. We can define the Green's function as the solution to the similar equation,

$$LG(\mathbf{x},\mathbf{x}') = \delta(\mathbf{x}-\mathbf{x}'), \tag{2.14}$$

where $\delta(\mathbf{x}-\mathbf{x}')$ is the Dirac delta function. If $G(\mathbf{x},\mathbf{x}')$ can be found, given suitable boundary conditions, then it is possible to solve for $u(\mathbf{x})$ via

$$u(\mathbf{x}) = \int_{-\infty}^{\infty} d\mathbf{x}' \;\; G(\mathbf{x},\mathbf{x}')f(\mathbf{x}'). \tag{2.15}$$

In condensed matter theory, the linear operator is the Hamiltonian. In the language of second quantisation, the Green's function is defined

$$G(\mathbf{x},\mathbf{x}',t,t') = -i\,\langle\Psi_0|Tc_{\mathbf{x}}(t)c^{\dagger}_{\mathbf{x}'}(t')|\Psi_0\rangle\,. \tag{2.16}$$

This equation measures the response of the many body system upon the addition of a fermion at position $\mathbf{x}'$ at time t' and its removal at position $\mathbf{x}$ and time t. The time ordering operator T ensures that every operator is arranged in order of increasing time such that the largest time is on the left hand side, and the smallest time is on the right,

$$Tc_{\mathbf{x}}(t)c^{\dagger}_{\mathbf{x}'}(t') = \begin{cases} c_{\mathbf{x}}(t)c^{\dagger}_{\mathbf{x}'}(t') & (t > t') \\ -c^{\dagger}_{\mathbf{x}'}(t')c_{\mathbf{x}}(t) & (t < t'). \end{cases} \tag{2.17}$$

In a homogeneous system, the Green's function only depends on the difference of the position variable, $\mathbf{x}-\mathbf{x}'$. It is therefore possible to Fourier transform the Green's function into momentum space by using

$$c_{\mathbf{x}}(t) = \int d\mathbf{k} \;\; e^{i\mathbf{k}\mathbf{x}}c_{\mathbf{k}}(t), \tag{2.18}$$

$$c^{\dagger}_{\mathbf{x}}(t) = \int d\mathbf{k} \;\; e^{-i\mathbf{k}\mathbf{x}}c^{\dagger}_{\mathbf{k}}(t). \tag{2.19}$$

Applying Eq. (2.18) and (2.19) to Eq. (2.16) then gives

$$G(\mathbf{x},\mathbf{x}',t,t') = -\int d\mathbf{k}\int d\mathbf{k}' \;\; i\,\langle\Psi_0|Tc_{\mathbf{k}}(t)c^{\dagger}_{\mathbf{k}'}(t')|\Psi_0\rangle\, e^{i(\mathbf{k}\mathbf{x}-\mathbf{k}'\mathbf{x}')}. \tag{2.20}$$

As the momentum space representation is diagonal $c_{\mathbf{k}}(t)c^{\dagger}_{\mathbf{k}'}(t')$ is zero everywhere except $\mathbf{k}=\mathbf{k}'$, the Green's function may be written in terms of a single momentum,

$$G(\mathbf{x},\mathbf{x}',t,t') = \int d\mathbf{k} \;\; G(\mathbf{k},t,t')e^{i\mathbf{k}(\mathbf{x}-\mathbf{x}')}, \tag{2.21}$$

where

$$G(\mathbf{k},t,t') = -i\,\langle\Psi_0|T c_{\mathbf{k}}(t)c^{\dagger}_{\mathbf{k}}(t')|\Psi_0\rangle\,. \tag{2.22}$$

Finally, by expanding the time ordering operator, the Green"s function becomes

$$G(\mathbf{k},t,t') = -i\big[\Theta(t-t')\,\langle\Psi_0|c_{\mathbf{k}}(t)c^{\dagger}_{\mathbf{k}}(t')|\Psi_0\rangle - \Theta(t'-t)\,\langle\Psi_0|c^{\dagger}_{\mathbf{k}}(t')c_{\mathbf{k}}(t)|\Psi_0\rangle\,\big]. \tag{2.23}$$

Here, $\Theta(t-t')$ is the Heaviside function[1] . This is the fundamental Green's function for a non-interacting many body system. The first term of Eq. (2.23) describes forward time propagation and is referred to as the retarded Green's function, whilst the second term of Eq. (2.23) describes backward time propagation and is referred to as the Advanced Green's function. In the following section I will discuss the solution to Eq. (2.23) for a non-interacting homogeneous system, how this can extend to include interacting systems, and show a useful rearrangement of the Green's function which can be directly measured by experimental probes.

2.3.1 The Green's function of a non-interacting system

Eq. (2.23) can not be numerically computed in the current form. It is possible to derive a compact equation for the Green's function for a non-interacting homogeneous system, (2.23). To do this, the time dependence is removed from the second quantisation operators using the Heisenberg representation,

$$\begin{aligned} c_{\mathbf{k}}(t) &= e^{-i\varepsilon_{\mathbf{k}}t}c_{\mathbf{k}}, \\ c^{\dagger}_{\mathbf{k}}(t) &= e^{i\varepsilon_{\mathbf{k}}t}c^{\dagger}_{\mathbf{k}}, \end{aligned} \tag{2.24}$$

Here, $\varepsilon_{\mathbf{k}}$ defines the energy of the particle at momentum $\mathbf{k}$. Eq. (2.23) describes two possible processes, either the addition of an electron to the system above k_F, or the addition of a hole below k_F. Due to particle-hole symmetry this is equivalent to the direction of time that the Green's function is acting in [122]. $t < t'$ for the addition of an electron and $t > t'$ for the addition of a hole.

For $t < t'$, the Retarded Green's function can be rearranged to give

[1] $\Theta(t-t') = \begin{cases} 1, & t > t' \\ \frac{1}{2}, & t = t' \\ 0, & t < t' \end{cases}$

$$i\langle\Psi_0|c_{\mathbf{k}}^{\dagger}(t')c_{\mathbf{k}}(t)|\Psi_0\rangle = ie^{-i\varepsilon_{\mathbf{k}}(t-t')}\langle\Psi_0|c_{\mathbf{k}}^{\dagger}c_{\mathbf{k}}|\Psi_0\rangle = ie^{-i\varepsilon_{\mathbf{k}}(t-t')}f(\varepsilon_{\mathbf{k}}), \tag{2.25}$$

where it was noted that

$$\langle\Psi_0|c_{\mathbf{k}}^{\dagger}c_{\mathbf{k}}|\Psi_0\rangle = \langle\Psi_0|n_{\mathbf{k}}|\Psi_0\rangle = f(\varepsilon_{\mathbf{k}}). \tag{2.26}$$

Here, $f(\varepsilon_{\mathbf{k}})$ is the Fermi function, $[e^{-\varepsilon_{\mathbf{k}}/k_bT}+1]^{-1}$, the expectation value of the particle density $n_{\mathbf{k}}$.
For $t > t'$, the Advanced Green's function can be written as

$$i\langle\Psi_0|c_{\mathbf{k}}(t')c_{\mathbf{k}}^{\dagger}(t)|\Psi_0\rangle = ie^{-i\varepsilon_{\mathbf{k}}(t-t')}\langle\Psi_0|c_{\mathbf{k}}c_{\mathbf{k}}^{\dagger}|\Psi_0\rangle = ie^{-i\varepsilon_{\mathbf{k}}(t-t')}(1-f(\varepsilon_{\mathbf{k}})). \tag{2.27}$$

The final part of Eq (2.27) was obtained from the rearrangement of $\langle\Psi_0|c_{\mathbf{k}}c_{\mathbf{k}}^{\dagger}|\Psi_0\rangle$ using the anticommutator relations of Eq. (2.5),

$$\langle\Psi_0|c_{\mathbf{k}}c_{\mathbf{k}}^{\dagger}|\Psi_0\rangle = 1 - \langle\Psi_0|c_{\mathbf{k}}^{\dagger}c_{\mathbf{k}}|\Psi_0\rangle. \tag{2.28}$$

Thus the complete Green's function can then be written in momentum space as

$$G(\mathbf{k},t,t') = -i[(1-f(\varepsilon_{\mathbf{k}}))\Theta(t-t') - f(\varepsilon_{\mathbf{k}})\Theta(t'-t)]e^{-i\varepsilon_{\mathbf{k}}(t-t')}. \tag{2.29}$$

On the assumption that the Hamiltonian is time independent, the system only depends on $\tau = t - t'$. Thus, the Green's function can be converted into frequency space via another Fourier transform,

$$G(\mathbf{k},\omega) = -\int_{-\infty}^{\infty} d\tau\ \ G(\mathbf{k},\tau)e^{i\omega\tau} = G^{+}(k,\omega) + G^{-}(k,\omega), \tag{2.30}$$

where

$$\begin{aligned} G^{+}(\mathbf{k},\omega) &= \frac{(1-f(\varepsilon_{\mathbf{k}}))}{\omega - \varepsilon_{\mathbf{k}} + i\delta}, \\ G^{-}(\mathbf{k},,\omega) &= \frac{f(\varepsilon_{\mathbf{k}})}{\omega - \varepsilon_{\mathbf{k}} - i\delta}. \end{aligned} \tag{2.31}$$

Finally, the infinitesimally small $i\delta_{\mathbf{k}}$ can be redefined as $i\delta_{\mathbf{k}} = i\delta\mathrm{sgn}(\mathbf{k}-\mathbf{k_F})$ to ensure that the Green's function is always on the correct side of the complex axis. With this,

$G^+(\mathbf{k},\omega)$ and $G^-(\mathbf{k},\omega)$ can be combined to give the final Green's function of a non-interacting homogeneous system,

$$G^0(\mathbf{k},\omega) = \frac{1}{\omega - \varepsilon_{\mathbf{k}} + i\delta_{\mathbf{k}}}. \tag{2.32}$$

Eq. (2.32) is now a simple equation where ω defines the energy and $\varepsilon_{\mathbf{k}}$ is the non-interacting band dispersion at momentum $\mathbf{k}$. If the band dispersion can be calculated, such as with a tight binding model, it will be possible to compute the non-interacting Green's function of the system, which can be used to calculate experimental properties.

2.3.2 Self energy

The above solution to the Green's function describes an ideal gas of non-interacting fermions. This, however, ignores the electron and spin interactions, which occur in physical systems. To account for the interaction between fermions, an energy dependent effective potential is introduced. This is called the self energy and is denoted symbolically by $\Sigma(\mathbf{k},\omega)$. This potential describes all many-body scattering processes that may occur within a fermionic system. As there are an infinite number of these scattering processes, the Green's function for an interacting system may be written as a sum over all possible pathways

$$G = G^0 + G^0\Sigma G^0 + G^0\Sigma G^0\Sigma G^0 + G^0\Sigma G^0\Sigma G^0\Sigma G^0 + ... \tag{2.33}$$

Here, G^0 is the Green's function for the non-interacting system, described in Eq. (2.30). The dependences on $\mathbf{k}$ and ω have been dropped for simplicity.

As this is an infinite sum, Eq. (2.33) can be written in the form of a Dyson equation,

$$G = G^0 + G^0\Sigma G. \tag{2.34}$$

This can be solved to give

$$G = G^0[1 - \Sigma G^0]^{-1} = [[G^0]^{-1} - \Sigma]^{-1}. \tag{2.35}$$

By substituting Eq. (2.32) into Eq. (2.35), the Green's function of an interacting system can be defined as,

$$G(\mathbf{k},\omega) = \frac{1}{\omega - \varepsilon_{\mathbf{k}} - \Sigma(\mathbf{k},\omega) + i\delta_{\mathbf{k}}}. \tag{2.36}$$

Here, $\Sigma(\mathbf{k},\omega)$ is generally a complex quantity,

$$\Sigma(\mathbf{k},\omega) = \Sigma'(\mathbf{k},\omega) + i\Sigma''(\mathbf{k},\omega). \tag{2.37}$$

The real part of the self energy is described by $\Sigma'(\mathbf{k},\omega)$ and the magnitude of the imaginary part is described by $\Sigma''(\mathbf{k},\omega)$. This imaginary component contains information directly relating to the inverse scattering rate τ^{-1} of the interacting process. This is a temperature dependent quantity that tends to zero at low temperatures [121].

Eq. (2.36) is the generic equation for a Green's function that describes interacting systems. However, an exact description of $\Sigma(\mathbf{k},\omega)$ is challenging to compute. To gain some insight into Eq. (2.36) , it is convenient to study this function in the limit of low temperature, and for small ω. In these limits, $\Sigma''(\mathbf{k},\omega)$ is negligible, and $\Sigma'(\mathbf{k},\omega)$ may be expanded around $\omega = 0$ such that

$$\Sigma'(\mathbf{k},\omega) = \Sigma'(\mathbf{k},0) + \frac{d\Sigma'(\mathbf{k},0)}{d\omega}\cdot\omega + O(\omega^2) + ... \tag{2.38}$$

The terms that are quadratic or higher in ω can be neglected and Eq. (2.36) can be written as

$$G(\mathbf{k},\omega) = \frac{1}{\omega\cdot(1-\frac{d\Sigma'(\mathbf{k},0)}{d\omega}) - \varepsilon^0_{\mathbf{k}} - \Sigma'(\mathbf{k},0) + i\delta_{\mathbf{k}}}. \tag{2.39}$$

By factoring out $Z_{\mathbf{k}} = \frac{1}{1-\frac{d\Sigma'(\mathbf{k},0)}{d\omega}}$, the renormalised Green's function can be defined

$$G(\mathbf{k},\omega) = Z_{\mathbf{k}}\frac{1}{\omega - Z_{\mathbf{k}}(\varepsilon^0_{\mathbf{k}} - \Sigma'(\mathbf{k},0) + i\delta_{\mathbf{k}})}. \tag{2.40}$$

This quantity, $Z_{\mathbf{k}}$, is defined as the quasiparticle weight. It is a parameter which provides a method to write a Green's function of an interacting system in a form that is similar to a non-interacting formalism. The difference is that the bare band dispersion of the non-interacting system is modified to $Z_{\mathbf{k}}(\varepsilon^0_{\mathbf{k}} - \Sigma'(\mathbf{k},0))$ and the entire function is then renormalised by a factor of $Z_{\mathbf{k}}$. This form will be used in Chapter 3.

2.3.3 Single particle spectral function

The single particle spectral function is a quantity that can be directly measured via photoemission. It provides a link between experimental observables and the underlying Green's function of an interacting system. This function describes the probability of a the removal of a single fermion from a many body ground state, and can provide

direct information about the band dispersion of a system. To derive the single particle spectral function, the identity $1 = \sum_m |\Psi_m\rangle \langle\Psi_m|$ is inserted into Eq. (2.23),

$$\begin{aligned} G(\mathbf{k},t,t') = &-i\Theta(t-t')\sum_m \langle\Psi_0|\, c_\mathbf{k}(t)\,|\Psi_m\rangle\,\langle\Psi_m|\, c_\mathbf{k}^\dagger(t')\,|\Psi_0\rangle \\ &+i\Theta(t'-t)\sum_m \langle\Psi_0|\, c_\mathbf{k}^\dagger(t')\,|\Psi_m\rangle\,\langle\Psi_m|\, c_\mathbf{k}(t)\,|\Psi_0\rangle\,. \end{aligned} \tag{2.41}$$

Next, equivalent to Sec. 2.3.1, the time dependence is removed by converting to the Heisenberg notation for the creation and annihilation operators, as defined in Eq. (2.24). The Green's function is then also Fourier transformed into frequency space to obtain

$$G(\mathbf{k},\omega) = \sum_m \frac{|\,\langle\Psi_0^N|c_\mathbf{k}|\Psi_m^{N+1}\rangle\,|^2}{(\omega-\varepsilon_\mathbf{k})-i\delta} + \frac{|\,\langle\Psi_m^{N-1}|c_\mathbf{k}|\Psi_0^N\rangle\,|^2}{(\omega-\varepsilon_\mathbf{k})+i\delta}. \tag{2.42}$$

Here, the identities

$$\begin{aligned} \langle\Psi_0|\, c_\mathbf{k}^\dagger\,|\Psi_m\rangle\,\langle\Psi_m|\, c_\mathbf{k}\,|\Psi_0\rangle &\equiv |\,\langle\Psi_m^{N-1}|c_\mathbf{k}|\Psi_0^N\rangle\,|^2, \\ \langle\Psi_0|\, c_\mathbf{k}\,|\Psi_m\rangle\,\langle\Psi_m|\, c_\mathbf{k}^\dagger\,|\Psi_0\rangle &\equiv |\,\langle\Psi_0^N|c_\mathbf{k}|\Psi_m^{N+1}\rangle\,|^2, \end{aligned} \tag{2.43}$$

have been used. It is noted that the particle number of the set of excited states, Ψ_m, must contain one extra particle in the first term of Eq. (2.42) and one less particle for the second term, else the expectation value would equal zero. Thus, Eq. (2.42) can be interpreted as the probability of an excitation from a particle in the ground state Ψ_0 to a system with a single excitation of either an electron or a hole, where the excitation may occur via all possible pathways m.

The single particle spectral function, $A(\mathbf{k},\omega)$, may now be defined as the imaginary part of the Green's function,

$$A(\mathbf{k},\omega) = -\mathrm{Im}G(\mathbf{k},\omega) = \sum_m |\,\langle\Psi_m^{N-1}|c_\mathbf{k}|\Psi_0^N\rangle\,|^2\delta(\omega-\varepsilon_\mathbf{k}) \qquad (\text{for } \omega<0) \tag{2.44}$$

and

$$A(\mathbf{k},\omega) = -\mathrm{Im}G(\mathbf{k},\omega) = \sum_m |\,\langle\Psi_0^N|c_\mathbf{k}|\Psi_m^{N+1}\rangle\,|^2\delta(\omega-\varepsilon_\mathbf{k}) \qquad (\text{for } \omega>0). \tag{2.45}$$

By taking the imaginary part of the Green's function, it is possible to extract informa-

tion regarding to the probability of an excitation for a given system, this can then be calculated directly using either the non-interacting form of Eq. (2.32),

$$-\mathrm{Im}G^0(\mathbf{k},\omega) = \delta(\omega - \varepsilon_{\mathbf{k}}), \tag{2.46}$$

or the Green's function of an interacting system defined in Eq. (2.36),

$$-\mathrm{Im}G(\mathbf{k},\omega) = \frac{\Sigma''(\mathbf{k},\omega)}{[\omega - \varepsilon_{\mathbf{k}} - \Sigma'(\mathbf{k},\omega)]^2 + [\Sigma''(\mathbf{k},\omega)]^2}. \tag{2.47}$$

It can be seen that the single particle spectral function of a non-interacting system describes a delta peak located at $\omega = \varepsilon_{\mathbf{k}}$. For an interacting system, at finite temperatures, the delta peak has now evolved to describe a Lorentzian function, with a width proportional to the imaginary part of the self energy. The poles have also shifted from the bare band dispersion by a value equivalent to the real part of the self energy.

As I will show in the following section, it is possible to directly measure this single particle spectral function of Eq. (2.44) using the principle of ARPES [126] and thus gain direct information on the band dispersion and self energy of a system.

2.4 Angle-resolved photoemission spectroscopy

2.4.1 Theory of photoemission spectroscopy

The photoelectric effect, originally observed by Hertz in 1887 [127], is the phenomena of the ejection of electrons from a metallic surface upon irradiation with electromagnetic waves. The fundamental theory of photoemission was first formulated by Einstein in 1906 [128]. Following on from the recent observation of quantised energy in black body radiation [129], Einstein suggested a theory that could explain the interaction of light with electrons in a solid. When a photon with energy $h\nu > \phi$ is fired at a material, a photoelectron may be emitted from the surface. Here, $h\nu$ is the energy of the photon, and ϕ defines the work function of a material, which is a measure of the energy required to overcome the potential barrier between the surface of the material and the vacuum. This theory was fundamental to the formation of quantum mechanics, and the understanding of condensed matter systems. However, it was not until 1970 that the full mathematical framework for "The theory of photoemission for simple metals" [130] was defined. Here, not only was the conservation of energy of photoemission fully accounted for, but the mathematical framework also described the conservation

of momentum. From this, it was shown that if the momentum of an outcoming photoelectron could be measured, the **k**-resolved energy of a periodic material could be determined. This would then provide a means to experimentally study the electronic structure of solids. In this section, I will outline the theoretical and experimental principles behind the technique of angle-resolved photoemission spectroscopy (ARPES), which will be used throughout this thesis.

Process of Photoemission

The photoemission process occurs when an electron in the initial state, i, gets excited into a final vacuum state, f, through a perturbative interaction, H_{int}. The probability that an electron will transition between an N-electron ground state, $|\Psi_i^N\rangle$, to an excited final state, $|\Psi_f^N\rangle$, can be approximated by Fermi's golden rule,

$$W_{fi} = \frac{2\pi}{\hbar} |\langle \Psi_f^N | H_{int} | \Psi_i^N \rangle|^2 \delta(E_f^N - E_i^N - h\nu)\delta(\mathbf{k}_f - \mathbf{k}_i - \mathbf{G}). \tag{2.48}$$

Here, $E_f^N, \mathbf{k}_f$ and $E_i^N, \mathbf{k}_i$ are the final and initial state energy and momentum of the system. The delta functions ensure the conservation of energy and momentum in the transition. In the case of momentum conservation, the momentum due to the incident photon, $\mathbf{k}_{h\nu}$, is neglected, as it is generally smaller than the intrinsic crystallographic momentum for photon energies of less than 100 eV [126]. The reciprocal lattice vector, **G**, however is essential to the process of photoemission. Without this periodicity inducing a backfolding of states, no zero momentum transfer would be possible [130] and photoemission would not occur. The interaction Hamiltonian, H_{int}, describes the coupling between an electron and the electromagnetic field generated by the photon [131],

$$H_{int} = \frac{e}{2mc}(\hat{\mathbf{A}} \cdot \hat{\mathbf{p}} + \hat{\mathbf{p}} \cdot \hat{\mathbf{A}} - \frac{e}{c}\hat{\mathbf{A}}^{\mathbf{2}}). \tag{2.49}$$

Here, $\hat{\mathbf{p}} = -i\hbar\nabla$ is the quantum mechanical momentum operator, and $\hat{\mathbf{A}}$ is the electromagnetic vector potential. Assuming a low intensity of photons, $\hat{\mathbf{A}}$ will be small, thus the quadratic term of Eq. (2.49) can be neglected. This reduces the equation to

$$H_{int} = \frac{-i\hbar e}{2mc}(\hat{\mathbf{A}} \cdot \nabla + \nabla \cdot \hat{\mathbf{A}}). \tag{2.50}$$

Using the dipole approximation, which assumes that $\hat{\mathbf{A}}$ will be constant on the scale of atomic distances, the second term of Eq. (2.50) can be neglected. This is due to

the fact that the divergence of the electromagnetic vector potential will be zero[2]. For a photoemission induced excitation, the interaction Hamiltonian can then be defined as the product of the electromagnetic vector potential and the electronic momentum,

$$H_{int} = \frac{e}{mc}\hat{\mathbf{A}} \cdot \hat{\mathbf{p}}. \tag{2.51}$$

Physically, photoemission occurs as a single process [134], where the wavefunction must take into account, bulk states, surface states, vacuum states and all interactions and resonances inbetween. However, this is challenging to compute. In the regime of studying excitations measuring photoelectrons that have high kinetic energy (> 20 eV), a phenomenological, three-step model can be used to describe the photoemission process [126, 135]. In this approach, photoemission is described by three independent mechanisms. Firstly, the electron in an initial state is excited within the material. Secondly, the excited electron travels to the surface of the material and, finally, the excited electron escapes from the surface into the vacuum.

A photoelectron will scatter within the material on an average length scale known as the inelastic mean free path. On scattering, the momentum and energy information regarding the electronic structure will be lost. As a consequence of this, only photoelectrons originating from a length scale less than the inelastic mean free path will contain information regarding the momentum and energy of the material, which ensures that photoemission is a surface sensitive technique. The distance probed in the z-axis by photoemission can however be tuned by increasing the initial photon energy, which will increase the inelastic mean free path of the photoelectron.

The three-step model therefore suggests that most of the information regarding the probability of photoemission will be contained within the initial excitation of an electron. If photons with a large enough kinetic energy are used, the excitation of an electron from the initial to final state can be approximated as instantaneous. Known as the sudden approximation, this allows us to rewrite an (N)-electron wavefunction as a product of an (N-1)-electron wavefunction, and a photoelectron eigenstate, $\Psi^N = c_k^\dagger \Psi^{N-1}$. Here, $c_k^\dagger$ is the second quantisation creation operator which creates a single particle eigenstate for the photoelectron ϕ^k . The transition probability from Eq (2.48) can then be written as

[2]Note that this approximation only holds for excitations within the bulk. At the surface this may not be negligible [132, 133].

$$W_{fi} = \frac{2\pi}{\hbar} |\langle \phi_f^{\mathbf{k}} | \hat{\mathbf{A}} \cdot \hat{\mathbf{p}} | \phi_i^{\mathbf{k}} \rangle|^2 \sum_m |\langle \Psi_m^{N-1} | c_k | \Psi_i^N \rangle|^2 \delta(E_{kin} + E_m^{N-1} - E_i^N - h\nu). \quad (2.52)$$

Here, it is noted that the final state, f, may have been reached via several different excited states, m. Hence, Ψ_f^{N-1} and E_f^{N-1} are replaced with a sum over all the possible excited states, m. The conservation of momentum has also been accounted for by ensuring that $\phi_f^{\mathbf{k}}$ and $\phi_i^{\mathbf{k}}$ have the same momentum $\mathbf{k} = \mathbf{k}_f = \mathbf{k}_i - \mathbf{G}$.

Finally, an initial state will only be excited if it is populated. To account for this physical feature the transitional probability is multiplied by the Fermi function,

$$f(\omega, T) = \frac{1}{1 + e^{\frac{\omega}{k_B T}}}. \quad (2.53)$$

Here, T defines the temperature of the system and k_B is the Boltzmann constant. The final equation for the intensity of the photocurrent is then

$$I(\mathbf{k}, \omega) = M_{fi}^{\mathbf{k}} \cdot A(\mathbf{k}, \omega) \cdot f(\omega). \quad (2.54)$$

In Eq. (2.54), the component outside the sum over m, has been redefined to $M_{fi}^{\mathbf{k}} = |\langle \phi_f^{\mathbf{k}} | \hat{\mathbf{A}} \cdot \hat{\mathbf{p}} | \phi_i^{\mathbf{k}} \rangle|^2$. The rest of the equation is then equivalent to the single particle spectral function, $A(\mathbf{k}, \omega)$, defined in Eq. (2.44). Therefore, if a material is irradiated with photons of high enough kinetic energy, and the outcoming photoelectrons are measured, direct information regarding the single particle spectral function may be obtained. This will then be able to provide information regarding the imaginary part of the interacting Green's function, from Eq. (2.47), and the underlying electronic structure.

2.4.2 Matrix elements

The first term of Eq. (2.54) is the so-called matrix elements of photoemission. Whilst the single particle spectral function contains information regarding the energy and momentum of the electronic states within a material, the matrix elements encode information regarding the symmetry of the initial wavefunction.

$$M_{fi}^{\mathbf{k}} = |\langle \phi_f^{\mathbf{k}} | \hat{\mathbf{A}} \cdot \hat{\mathbf{p}} | \phi_i^{\mathbf{k}} \rangle|^2. \quad (2.55)$$

A property of Eq. (2.55) is that $M_{fi}^{\mathbf{k}}$ will only be finite if the integrand is totally

symmetric with respect to the scattering plane. This constraint implies that only certain combinations of $\langle \phi_f^{\mathbf{k}} |$, $\hat{\mathbf{A}} \cdot \hat{\mathbf{p}}$ and $| \phi_i^{\mathbf{k}} \rangle$ will be measurable.

The symmetry of both the initial state wavefunction, $| \phi_i^{\mathbf{k}} \rangle$, and the final state wavefunction, $\langle \phi_f^{\mathbf{k}} |$ are fixed. For the initial state wavefunction, the symmetry is constrained by the geometry of the crystal with respect to the scattering plane and can be either symmetric or antisymmetric depending on the initial state being excited. The final state wavefunction, however, must always be symmetric with respect to the scattering plane. If the final state wavefunction is not symmetric, there would be no overlap between a symmetric free electron in the vacuum and the final state wavefunction, thus it would not be possible for the electron to escape into the vacuum and no photoemission intensity will be detected.

The symmetry of the interaction Hamiltonian, $\hat{\mathbf{A}} \cdot \hat{\mathbf{p}}$, however, can be controlled. In an idealised experimental setup, the incoming photon beam and photoelectron detector will lie along the scattering plane, as presented in Fig. 2.1(a). In this scenario, it is possible to use linearly polarised photons, such that the electromagnetic field component is either symmetric with respect to the scattering plane or antisymmetric. This can be achieved using vertically polarised light (LV) or horizontally polarised light (LH) respectively. It is therefore possible to probe the symmetry of the initial wavefunction of a sample simply by switching the polarisation of light. The d-orbitals are shown in Fig. 2.1(b-f) to illustrate this principle. The $3d_{yz}$, $3d_{x^2-y^2}$ and $3d_{z^2}$ orbitals are all symmetric with respect to the scattering plane and will be observed under LV light. The d_{xz} and d_{xy} orbitals are antisymmetric with respect to the scattering plane and will be detected under LH light.

The arguments presented here weaken for states with finite momenta, and in reality the alignment of sample and photon beam may not be exact. Nevertheless, a majority of the intensity that would be associated with antisymmetric matrix elements will still be suppressed under linearly polarised light. This allows photoemission experiments to probe not only the energy and momenta of the electronic structure, but also the underlying orbital content of a band.

2.4.3 Experimental principle

Fig. 2.1(a) describes a schematic for the experimental setup of an ARPES experiment. A beam of photons is fired at the surface of a material. This induces photoelectrons, with a range of kinetic energies, to be ejected out of the material at all angles. By collecting these photoelectrons, within a specific energy range and given angles of θ

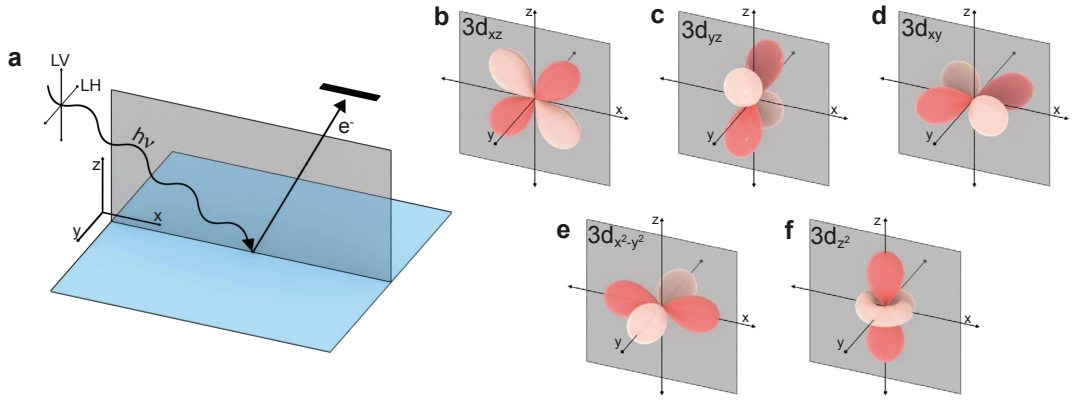

Figure 2.1: Schematic illustration of matrix elements and orbital symmetries. a) The photoemission setup, the scattering plane is shown in grey. The wavey line ($h\nu$) describes a photon, whilst the straight line describes a photoelectron. LV and LH describe the polarisation of light, either linear vertical or linear horizontal. The d-orbitals b) $3d_{xz}$ c) $3d_{yz}$ d) $3d_{xy}$ e) $3d_{x^2-y^2}$ f) $3d_{z^2}$ are also shown. The scattering plane in grey is presented to highlight the symmetry of the orbitals with respect to the plane.

and ϕ, it is possible to determine the binding energy of an electronic state within a material as well as the in-plane momentum of that state. This can be calculated via

$$E_{bind} = h\nu - \Phi - E_{kin} \tag{2.56}$$

$$\mathbf{k_x} = \frac{1}{\hbar}\sqrt{2mE_{kin}}\sin(\theta)\cos(\phi) \tag{2.57}$$

$$\mathbf{k_y} = \frac{1}{\hbar}\sqrt{2mE_{kin}}\sin(\theta)\sin(\phi). \tag{2.58}$$

Here, the binding energy, E_{bind}, is determined from the energy difference between the incident photon and outcoming photoelectron. $h\nu$ describes the energy of the photon beam, Φ defines the work function of a material, and E_{kin} is the measured photoelectron energy.

The in-plane momentum is determined by converting from the measurement geometry of spherical polar coordinates to a Cartesian coordinate system. Here, m defines the electron mass and $\hbar$ is the reduced Plancks constant. By rotating the surface of the sample, the angles θ and ϕ may be altered, and thus the electronic structure at any $\mathbf{k_x}$ and $\mathbf{k_y}$ may be measured.

At the surface of a material the z axis is no longer periodic and thus the out of plane momentum, $\mathbf{k_z}$, is no longer a good quantum number. Information regarding $\mathbf{k_z}$ may, however, still be obtained if the final state of the electron within the sample is assumed

to behave as a nearly free electron.

$$E_f(\mathbf{k}) = \frac{\hbar^2\mathbf{k}^2}{2m} - |E_0| = \frac{\hbar^2(\mathbf{k_x}^2 + \mathbf{k_y}^2 + \mathbf{k_z}^2)}{2m} - |E_0|. \tag{2.59}$$

Here, $E_f(\mathbf{k}) = E_{kin} - \Phi$, and E_0 is the bottom of the parabolic, nearly free electron, band. In this approximation, Eq. (2.59) can be rearranged to give an equation for $\mathbf{k_z}$

$$\mathbf{k_z} = \frac{1}{\hbar}\sqrt{2m(E_{kin}\cos^2(\theta) + V_0)}. \tag{2.60}$$

Here, $V_0 = |E_0| + \Phi$. This equation suggests that the $\mathbf{k_z}$ momentum can be altered by changing the initial photon energy and will also change as a function of angle. The implication of this is that a Fermi surface map measuring a full Brillouin zone at a fixed photon energy will not probe a single plane in $\mathbf{k_z}$. This must be accounted for if specific high symmetry points are of interest.

The surface sensitivity of photoemission will also induce an uncertainty into the measurement of $\mathbf{k_z}$. As photoemission experiments only probes a finite distance below the surface, proportional to the inelastic mean free path, there will be a finite broadening along $\mathbf{k_z}$ axis. In relatively two-dimensional materials, this will not greatly effect the measured in-plane electronic structure. However, for highly three-dimensional materials, the measured photoemission data may exhibit partial averaging in $\mathbf{k_z}$. From these principles ARPES can be used to probe the full three dimensional electronic structure of a material.

2.4.4 Synchrotron radiation and high resolution ARPES

The experimental work presented in this thesis has been performed at the I05 ARPES beamline at the Diamond Light Source in the United Kingdom. In this section I will outline the technical details used at this facility that allow for high resolution ARPES experiments.

The Diamond Light source is a synchrotron radiation facility, which accelerates electron up to 3 GeV within a storage ring. The storage ring consists of 24 straight sections with bending magnets at each corner to produce a closed loop which the electrons traverse. Insertion devices or bending magnets are additionally placed at each corner of the ring to generate the radiation required for experimental use. In the case of the I05 beamline an undulator insertion device has been fitted which produces radiation in the visible-ultraviolet (VUV) region between 18 eV and 240 eV [136]. This device is of APPLE II type and consists of four sets of $N = 34$ permanent magnets, as shown in

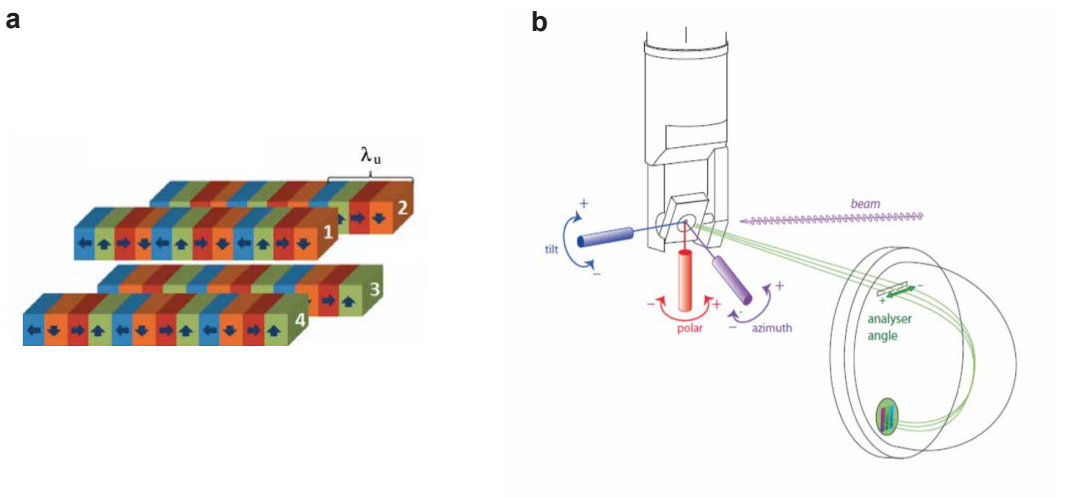

Figure 2.2: a) The APPLE II undulator, showing the four sets of superconducting magnets. Figure taken from Ref. [137]. b) Diagram of the sample manipulator and hemispherical analyser setup at the I05 beamline.

Fig. 2.2(a). This setup constrains the angular distribution of the electron beam such that the emitted photons have an angular spread of $\Delta\theta = \frac{1}{\sqrt{N}}\gamma^{-1}$. Here, $\gamma^{-1} = \sqrt{1-\frac{v^2}{c^2}}$ where v is the velocity of the electrons and c is the speed of light. These photons are mostly in phase and will therefore constructively interfere, producing flux N^2 times greater than is achievable with a single bending device.

The energy of the outcoming photons may be tuned by changing the distance between the upper and lower sets of permanent magnets. It is also possible to displace the upper and lower sets of magnets with respect to one another to enable the production of linear horizontal, linear vertical and circularly polarised light [138].

To further increase the energy resolution of the photon beam, a plane grating monochoromator is used, this device provides an energy resolving power of $\frac{\Delta_E}{E} = 20,000$ for photon energies of less than 100 eV [136]. The photon beam is then focused via a series of mirrors to produce a final photon spot size of 50 x 50 μm at the sample surface.

The surface of a sample is prepared via cleaving in ultra-high vacuum ($< 10^{-10}$ mbar). This process involves breaking the top of the sample by gluing a post to the crystal, and removing with force. In an ideal scenario, the freshly generated surface should be flat with no dirt adsorbed onto it. The sample is mounted on a manipulator with 6 degrees of freedom [136], allowing for precise movement of the sample in the x, y and z directions. The sample may also be rotated in the polar and azimuthal directions, and tilted to align the sample with respect to the photon beam, as shown in Fig. 2.2(b).

This provides the ability to orient the sample along a high symmetry direction, and map the **k**-space in two dimensions.

Finally, the outcoming photoelectrons are collected in a hemispherical analyser. The entrance of this device consists of an slit and preretarding lens. The entrance slit can be used to increase the energy resolution of the measurement, whereas the preretarding lens greatly reduces the energy of the photoelectrons without altering the spread of energies. The photoelectrons traverse a hemispherical pathway, where the photoelectrons are bent by a potential difference between two hemispherical plates separated by a fixed distance. Only electrons with a particular energy, $E_0 \pm \Delta E_0$, will be collected at the detector which may be tuned by changing the potential difference between the two hemispheres. The energy E_0 is known as the pass energy. A lower pass energy increases the energy resolution of the experiment at the expense of the intensity of measured photons. The total number of photoelectrons hitting the detector is then counted and converted into a data file of kinetic energy vs angle, which can be transformed into binding energy vs momentum as discussed in Section 2.4.3.

3 | Tight binding model for the tetragonal phase of FeSe

3.1 Introduction

We begin our study of the electronic structure of FeSe by looking at the tetragonal phase of the material. At high enough temperatures, all iron-based superconductors exhibit a paramagnetic state with tetragonal lattice symmetry [139]. This can therefore be thought of as a normal phase of the iron-based superconductors, from which the spontaneous orderings of nematicity, magnetism and superconductivity emerge.

DFT-based models qualitatively capture the band dispersions of the tetragonal phase of FeSe above 90 K, correctly describing a Fermi surface consisting of localised hole and electron pockets [140, 141]. However, these *ab-initio* calculations overestimate the energy scale of the band dispersions when compared with ARPES measurements [117]. The calculations describe a system where the maxima of the hole bands and minima of the electron bands are several hundred meV above or below the Fermi level [142]. This is in contrast to experiment measurements where the band maxima and minima are less than ± 50 meV from the Fermi level [100]. Moreover, partially due to this discrepancy, DFT based models of FeSe suggest a Fermi surface with three hole pockets at the centre of the Brillouin zone, whereas experimentally only two are observed [100].

One reason for this difference, between theory and experiment, is that DFT calculations do not account for spin fluctuations as a result of the electron-electron interaction, which becomes important in strongly correlated materials. The theoretical framework of DFT + Dynamic Mean Field Theory (DMFT) attempts to rectify this issue by self consistently including local spin fluctuations onto an already converged DFT-based electronic structure. Whilst this framework captures most of the renormalisation associated with the bandwidth of the 3d Fe bands of FeSe [84], the size of the hole and

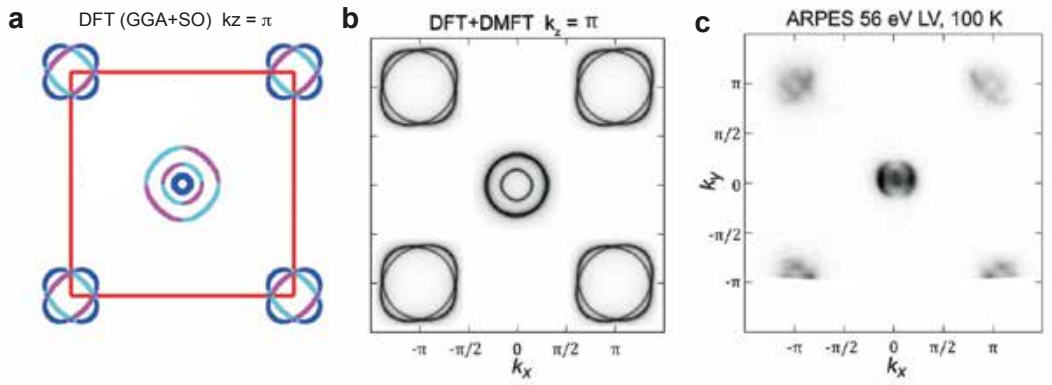

Figure 3.1: Comparison of the Fermi surface of FeSe at $k_z = \pi$. a) The Fermi surface predicted by a DFT based model [100]. b) The Fermi surface predicted by a DFT + DMFT based model [101]. c) The Fermi surface measured by ARPES at 100 K [101].

electron pockets at the Fermi level are still much larger than what is measured using ARPES [102]. The Fermi surface of FeSe suggested by DFT and DFT + DMFT calculations, as well as the Fermi surface measured by ARPES experiments is shown in Fig. 3.1.

In order to study the superconducting properties of FeSe, it is essential to have a model which can precisely describe the Fermi surface of the material. In this chapter, to overcome this limitation of *ab-initio* models, I will develop an ARPES-based tight binding description of FeSe. This model will be optimised directly to experimental ARPES data in the tetragonal phase at 100 K, which will provide a quantitative phenomenological description of the band dispersions. Using this model, I will study the temperature dependence of the chemical potential of FeSe in the tetragonal phase. I will show that this experimental model predicts a large shift to the chemical potential as the temperature is increased between 100 K and 300 K, a feature not captured by *ab-initio* models. I will then confirm this prediction by performing a temperature dependent ARPES study on FeSe. This model will provide the basis to study the emergent orderings within the nematic and superconducting state in the following chapters.

3.2 Tight binding model of FeSe

FeSe has a quasi-2D layered crystal structure, consisting of a 2D plane of Fe atoms connected by Se atoms. These Se atoms are staggered above and below the plane, as shown in Fig. 3.2(b), such that a single unit cell of FeSe consists of two Fe-atoms and two Se-atoms. In Fig. 3.2(a) we present a top-down view of FeSe showing several

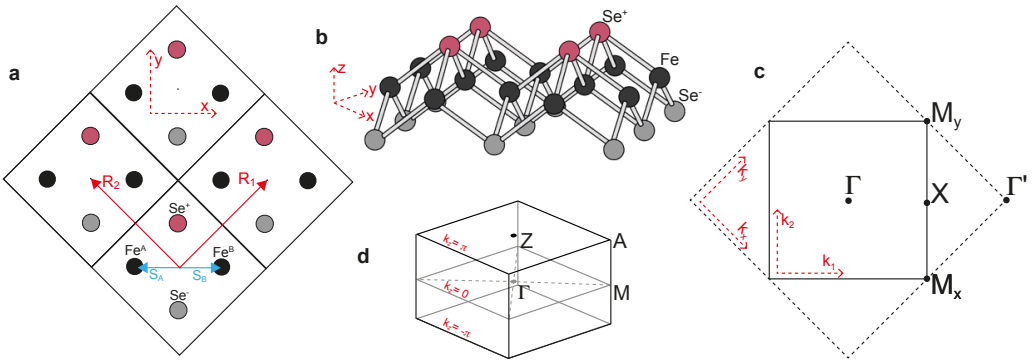

Figure 3.2: Crystal and electronic structure of the $P4/nmm$ space group. a) Top down view of the unit cell structure of FeSe. The boxes define a unit cell, black circles describe *Fe* atoms, whilst grey circles describe *Se* atoms. Red vectors describe the primitive lattice vectors, whilst the blue vectors describe the distance between the centre of the unit cell and an Fe atom. b) 3D crystal structure of a single layer of FeSe. c) 2D Brillouin zone of FeSe, the solid black line defines the 2-Fe Brillouin zone boundary with axes $k_1 = k_x + k_y$ and $k_2 = -k_x + k_y$. The dashed line describe an unfolded 1-Fe Brillouin zone, with axes k_x and k_y. In the 2-Fe notation (k_1, k_2) the high symmetry points are labelled $\Gamma = (0,0)$, $M_x = (\pi, -\pi)$, $M_y = (\pi, \pi)$ and $X = (\pi, 0)$ and $\Gamma' = (2\pi, 0)$. d) Three dimensional Brillouin zone description, defining the $k_z = \pi$ high symmetry points, $Z = (0, 0, \pm\pi)$ and $A = (\pi, \pi, \pm\pi)$.

adjacent unit cells, and the vectors which connect the atomic positions.

The primitive lattice vectors for the crystal are defined

$$\begin{aligned} R_1 &= R_x + R_y \\ R_2 &= -R_x + R_y \end{aligned} \tag{3.1}$$

These vectors correspond to the red vectors in Fig. 3.2(a). R_x and R_y describe the vector which connects neighbouring Fe atoms in the x and y direction.

In this tight binding model we will only focus on the d-orbitals of the Fe atoms, which are the bands present close to the Fermi level [140]. We can then define lattice vectors connecting the two Fe atoms, Fe^A and Fe^B, by

This tight binding model will only focus on the d-orbitals of the Fe atoms, which are present in the vicinity of the Fermi level [140]. Each unit cell of FeSe consists of two Fe-atoms, labelled Fe^A and Fe^B. The primitive lattice vectors of the individual atoms can then be defined

$$\begin{aligned} R_A &= n_1 R_1 + n_2 R_2 + S_A \\ R_B &= n_1 R_1 + n_2 R_2 + S_B \end{aligned} \tag{3.2}$$

Here, n_1 and n_2 are integers, and S_A and S_B describe the vector between the centre of the unit cell and either Fe atom A or Fe atom B. In momentum space, the 1st Brillouin zone is defined between $-\pi$ and $+\pi$ for the momentum vectors $k_1 = k_x + k_y$ and $k_2 = -k_x + k_y$, this is referred to as the 2-Fe unit cell. This produces a square Brillouin zone with high symmetry points Γ, M and X with coordinates $(k_1, k_2) = (0,0)$, (π,π) and $(\pi,0)$ in the $k_z = 0$ plane. At $k_z = \pm\pi$, the equivalent high symmetry points are labelled as Z, A and R as shown in Fig. 3.2(d).

Mathematically, it is possible to unfold the 2-Fe Brillouin zone, into an effective 1-Fe Brillouin zone, by making use of the non symmorphic glide symmetry of the $P4/nmm$ lattice [143]. This would produce the larger Brillouin zone, shown as the dashed boundaries in Fig. 3.2(c), with Brillouin zone boundaries at $\pm\pi$ in the k_x and k_y axis. Physically, ARPES measures the 2-Fe unit cell of FeSe, this will therefore be used for the optimisation of the tight binding model.

The general form of the tight binding model can then be generated by defining the creation and annihilation operators for fermions originating on either of the two Fe atoms.

$$c_A^{\alpha}(\mathbf{k}) = \sum_{R_A} e^{i\mathbf{k}R_A} c^{\alpha}(R_A) \qquad c_A^{\alpha\dagger}(\mathbf{k}) = \sum_{R_A} e^{-i\mathbf{k}R_A} c^{\alpha\dagger}(R_A) \tag{3.3}$$

$$c_B^{\alpha}(\mathbf{k}) = \sum_{R_B} e^{i\mathbf{k}R_B} c^{\alpha}(R_B) \qquad c_B^{\alpha\dagger}(\mathbf{k}) = \sum_{R_B} e^{-i\mathbf{k}R_B} c^{\alpha\dagger}(R_B) \tag{3.4}$$

These operators then define the creation ($c_{A/B}^{\alpha\dagger}(\mathbf{k})$) or annihilation ($c_{A/B}^{\alpha}(\mathbf{k})$) of a fermion in orbital α on Fe^A or Fe^B , with momentum $\mathbf{k}$. The glide symmetry of the $P4/nmm$ lattice provides a connection between the creation and annihilation operators of the two Fe atoms,

$$T_\tau P_z c_A^{\alpha}(\mathbf{k}) = (-1)^{\alpha} c_B^{\alpha}(\mathbf{k}). \tag{3.5}$$

This glide symmetry operator is executed by a translation, T_τ, of the vector $\tau = S^B - S^A$, followed by a reflection in the z axis (P_z). This operator will change the parity of the initial orbital depending on whether the orbital is symmetric or antisymmetric with

respect to reflection in the z axis. For the 3d orbitals

$$(-1)^{\alpha} = \begin{cases} +1, & d_{xy}, d_{x^2-y^2}, d_{z^2} \\ -1, & d_{xz}, d_{yz}. \end{cases} \tag{3.6}$$

It is then possible to define a linear combination of the creation and annihilation operators for the two Fe atoms,

$$c_E^{\alpha}(\mathbf{k}) = \frac{1}{\sqrt{2}}[c_A^{\alpha}(\mathbf{k}) + (-1)^{\alpha} c_B^{\alpha}(\mathbf{k})], \tag{3.7}$$

$$c_O^{\alpha}(\mathbf{k}) = \frac{1}{\sqrt{2}}[c_A^{\alpha}(\mathbf{k}) - (-1)^{\alpha} c_B^{\alpha}(\mathbf{k})]. \tag{3.8}$$

These new operators are decoupled with respect to the relative even (E) or odd (O) symmetries under the glide plane. A Hamiltonian which incorporates the glide symmetry of the $P4/nmm$ lattice can now be defined as,

$$H(\mathbf{k}) = \sum_{\alpha\beta}\sum_{\mathbf{k}} t_E^{\alpha\beta}(\mathbf{k}) c_E^{\alpha\dagger}(\mathbf{k}) c_E^{\beta}(\mathbf{k}) + t_O^{\alpha\beta}(\mathbf{k}) c_O^{\alpha\dagger}(\mathbf{k}) c_O^{\beta}(\mathbf{k}). \tag{3.9}$$

Here, the even and odd components of the Hamiltonian do not mix without the inclusion of spin orbit coupling [143]. The creation and annihilation operators of Eq. (3.9) can then be substituted into Eq. (3.7) and (3.8) to produce a Hamiltonian with the form,

$$\begin{aligned} H(\mathbf{k}) = \frac{1}{2}\sum_{\alpha\beta}\Big[& \sum_{\mathbf{k}} (t_E^{\alpha\beta}(\mathbf{k}) + t_O^{\alpha\beta}(\mathbf{k})) c_A^{\alpha\dagger}(\mathbf{k}) c_A^{\beta}(\mathbf{k}) \\ & + \sum_{\mathbf{k}} (t_E^{\alpha\beta}(\mathbf{k}) - t_O^{\alpha\beta}(\mathbf{k})) c_B^{\alpha\dagger}(\mathbf{k}) c_A^{\beta}(\mathbf{k}) (-1)^{\alpha} \\ & + \sum_{\mathbf{k}} (t_E^{\alpha\beta}(\mathbf{k}) - t_O^{\alpha\beta}(\mathbf{k})) c_A^{\alpha\dagger}(\mathbf{k}) c_B^{\beta}(\mathbf{k}) (-1)^{\beta} \\ & + \sum_{\mathbf{k}} (t_E^{\alpha\beta}(\mathbf{k}) + t_O^{\alpha\beta}(\mathbf{k})) c_B^{\alpha\dagger}(\mathbf{k}) c_B^{\beta}(\mathbf{k}) (-1)^{\alpha} (-1)^{\beta} \Big] \end{aligned} \tag{3.10}$$

This Hamiltonian can now be written as a 2x2 block matrix, where each block is a 5x5 matrix, H^{XY}, which describes the hopping process between any d-orbital on Fe^X and any d-orbital on Fe^Y.

$$H(\mathbf{k}) = \begin{pmatrix} H^{AA}(\mathbf{k}) & H^{AB}(\mathbf{k}) \\ H^{BA}(\mathbf{k}) & H^{BB}(\mathbf{k}) \end{pmatrix} \tag{3.11}$$

Due to the presence of time reversal symmetry(**T**) , $\mathbf{T}c^{\alpha}(\mathbf{k}) = c^{\beta}(\mathbf{k})^*$ [142], the Hamiltonian may be further simplified to,

$$H(\mathbf{k}) = \begin{pmatrix} H^{AA}(\mathbf{k}) & H^{AB}(\mathbf{k}) \\ H^{AB}(\mathbf{k})^* & H^{AA}(\mathbf{k})^* \end{pmatrix}. \tag{3.12}$$

This reduces the number of hopping parameters required by a factor of two. For this work, the momentum space formalism developed for FeSe by Eschrig and Koepernik [142] will be used. In Appendix A, the form of each element of the Hamiltonian is defined, and the hopping parameters used in the optimisation procedure are presented.

Finally, spin orbit coupling is included via

$$\hat{H}_{SOC}(k) = \begin{pmatrix} H(\mathbf{k}) + \hat{L}_z & \hat{L}_x + i\hat{L}_y \\ \hat{L}_x - i\hat{L}_y & H(\mathbf{k}) - \hat{L}_z \end{pmatrix} \tag{3.13}$$

where $\hat{L}_i$ is defined as

$$\hat{L}_i = \frac{\lambda}{2} \begin{pmatrix} \hat{l}_i & 0 \\ 0 & \hat{l}_i \end{pmatrix} \tag{3.14}$$

The 5x5 matrices $\hat{l}_x$, $\hat{l}_y$ and $\hat{l}_z$ are presented in Appendix A and discussed in Ref. [91]. The strength of the spin-orbit interaction,λ is fixed to $\lambda = 19$ meV throughout this thesis, which is in quantitatively agreement with experiment [144].

3.3 ARPES data of FeSe at 100 K

In Fig. 3.3, the ARPES data of the high symmetry points of FeS used in the optimisation procedure is presented. Fig. 3.3(a) describes the Γ point of FeSe at $k_z = 0$. Two hole bands can be observed, the outer hole band is seen to just cross the Fermi level, whereas the inner hold band has a maximum at -13 meV. At the $k_z = \pi$ Z point, of Fig. 3.3(c), a similar band dispersion is observed, except that both hole bands now cross the Fermi level. The two bands at $k_z = \pi$ are roughly 20 meV higher in energy than at the $k_z = 0$ position. These two bands consist of d_{xz} and d_{yz} weight respectively and are C_4 symmetric, such that rotating the sample 90 degrees will produce equivalent band positions with the d_{xz} and d_{yz} orbital weight swapped. These bands are also observed to be split by spin orbit coupling by a value of 20 meV [90, 91, 144]. For the electron states at the M and A point, the symmetry of the $P4/nmm$ crystal structure implies the presence of two degenerate sets of bands at the corner of the Brillouin zone [102, 145].

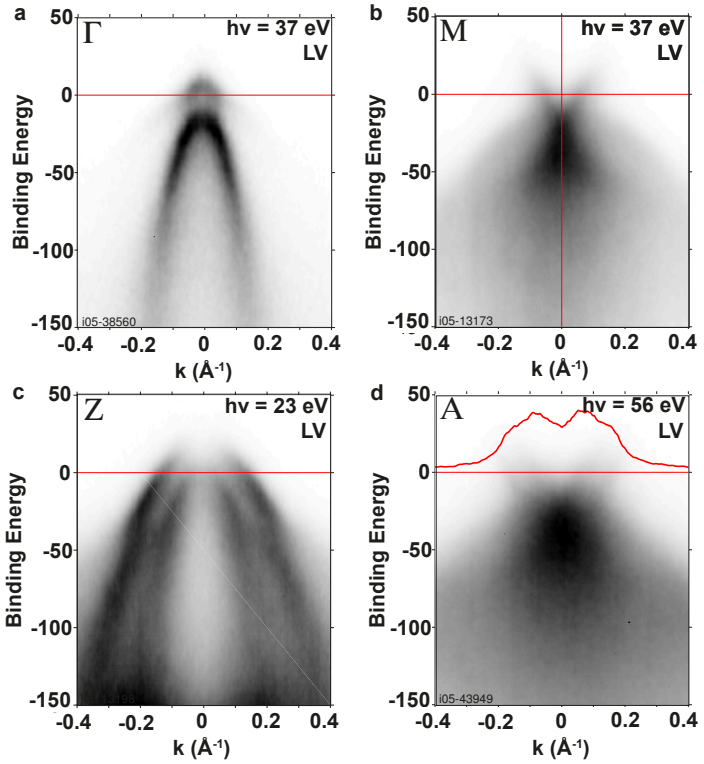

Figure 3.3: ARPES data from the four high symmetry points of FeSe in the tetragonal phase under Linear Vertical (LV) polarised light. a) ARPES data of the hole bands around the Γ point at 100 K with $h\nu = 37$ eV. b) ARPES data of the electron bands around the M point at 100 K with $h\nu = 37$ eV. c) ARPES data of the hole bands around the Z point at 120 K with $h\nu = 23$ eV. d) ARPES data of the electron bands at the A point at 100 K $h\nu = 56$ eV.

These degenerate states form saddle points, which give rise to two Van-Hove singularities. As a consequence, a large density of states is measured at the corner of the Brillouin zone, which can be seen at the $k_z = 0$, M point, in Fig. 3.3(b) and at the $k_z = \pi$, A point, in Fig. 3.3(d). This makes determining the exact band positions along the high symmetry axis less precise. However, two bands can be observed crossing the Fermi level at the A point. The inner band is of d_{yz} weight, whilst the outer band is of d_{xy} weight[1]. It is therefore possible to extract the estimated minimum binding energies for these two electron bands by approximating parabolic dispersions to these bands. By performing this analysis it suggests that there exists a 20 meV separation between the two bands. The d_{xy} saddle point has a binding energy of ∼-40 meV and the upper d_{yz}/d_{xz} saddle point has a binding energy of ∼-20 meV. This data will be used in the

[1]This d_{xy} band, however, is not resolved at the M point in this geometry due to matrix element effects.

optimisation of the tight binding model.

3.4 Optimisation of an ARPES-based tight binding model

Consider the equation for the single particle spectral function measured by ARPES,

$$A(\mathbf{k},\omega) = \frac{\Sigma''(\mathbf{k},\omega)}{[\omega - \varepsilon_{\mathbf{k}} - \Sigma'(\mathbf{k},\omega)]^2 + [\Sigma''(\mathbf{k},\omega)]^2}. \tag{3.15}$$

Here, $\Sigma'(\mathbf{k},\omega)$ and $\Sigma''(\mathbf{k},\omega)$ describe the real, and imaginary part of the self energy and $\varepsilon_{\mathbf{k}}$ is the bare band dispersion. Eq. (3.15) describes a Lorentizan equation which is peaked at $\varepsilon_{\mathbf{k}} - \Sigma'(\mathbf{k},\omega)$, and has a width proportional to $\Sigma''(\mathbf{k},\omega)$.

From this equation, it can be seen that all of the information regarding the momentum dependent band dispersion is contained within the peak position of the single particle spectral function. As discussed in Section 2.3.3, by neglecting the width of the spectral function peak $\Sigma''(\mathbf{k},\omega)$, and assuming the low energy, low temperature, limit, Eq. (3.15) can be rewritten as

$$A(\mathbf{k},\omega) = Z \cdot \delta(\omega - Z \cdot (\varepsilon^0_{\mathbf{k}} - \Sigma(\mathbf{k},0))) = Z \cdot \delta(\omega - E^{exp}(\mathbf{k})). \tag{3.16}$$

Where Z describes the quasiparticle weight, which is a real quantity between 0 and 1. This will simply renormalise the magnitude of the spectral function and, assuming that the quasiparticle weight of each orbital is approximately equivalent, can be neglected. From this equation, the experimentally measured single particle spectral function can be directly related to the experimental band dispersion $E^{exp}(\mathbf{k})$, without explicitly knowing the components of Z, $\varepsilon^0_{\mathbf{k}}$ and $\Sigma(\mathbf{k},0)$. A phenomenological tight binding description of the electronic structure which can correctly describes the E vs $\mathbf{k}$ experimental band dispersion can then be defined, without knowing the fine details regarding the self energy.

The ARPES-based hopping parameters were optimised by first rescaling the LDA-based hopping parameters defined by Eschrig *et. al.* [142] by a factor of 6. This is a phenomenological rescaling to ensure the bands are on the correct energy scale measured in experiment, as discussed by Mukherjee *et. al.* [146]. This is then followed by a least squares minimisation routine where the bands are fit to the peak positions extracted from ARPES data. This experimental data is presented as orange crosses in Fig. 3.4(e) and 3.5(a). The optimised hopping parameters are presented in Appendix A.

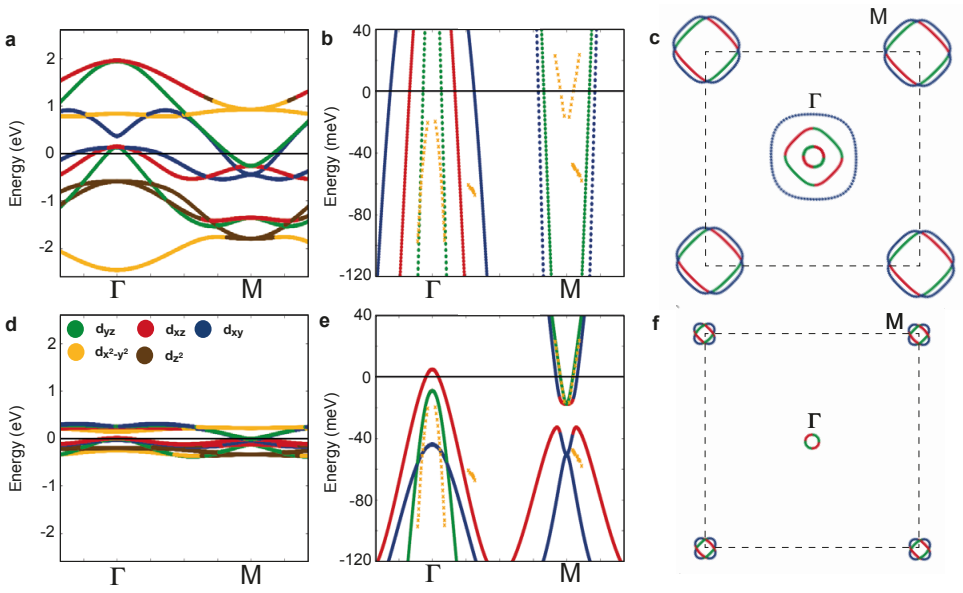

Figure 3.4: Comparison of the electronic structure at $k_z = 0$ predicted from a tight binding model of FeSe using either a DFT-based set of hopping parameters or the optimised ARPES-based set of hopping parameters. a) Band dispersion within a ± 2.5 eV energy scale for the DFT-based model. b) Close up band dispersion, around the Fermi level, for the DFT-based model. c) Fermi surface of the DFT-based model. d-f) Equivalent images for the ARPES-based model. The band colour indicate the maximum orbital contribution at a given momenta, as labelled in (d), and the orange crosses in (b) and (e) describe the experimental band positions extracted from the data in Fig. 3.3.

In Fig. 3.4, a comparison of the electronic structure predicted from two sets of hopping parameters is presented. The first set describes the DFT-based band dispersion, originally presented in Ref. [142], and the second set describes the experimentally optimised ARPES-based band dispersion. In Fig. 3.4(a), the band dispersions of the DFT-based tight binding model is shown. It describes a system with a d-orbital bandwidth of roughly 4 eV. On a smaller energy scale, three hole bands can be observed crossing the Fermi level, around the Γ point, and two electron bands crossing the Fermi level, around the *M* point. These band positions do not quantitatively agree with the ARPES data, presented as orange crosses. In Fig. 3.4(c), the Fermi surface predicted from the DFT-based hopping parameters is presented. The hole and electron pockets are predicted to be much larger than observed experimentally, with three hole pockets and square-like electron pockets.

Using the ARPES-based hopping parameters, the band dispersion now describes a much narrower d-orbital bandwidth of $\sim$600 meV, as shown in Fig. 3.4(d). In Fig.

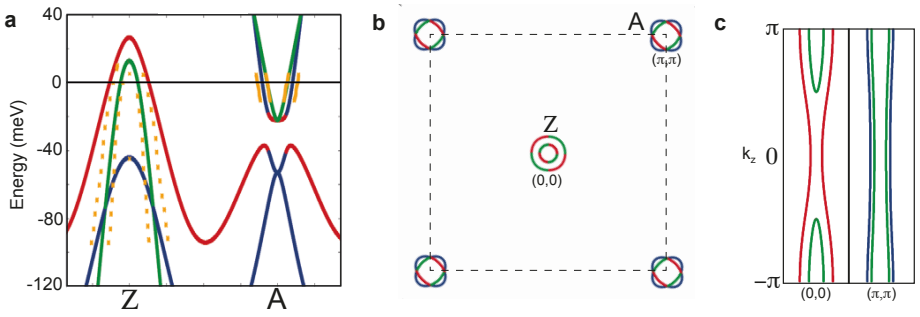

Figure 3.5: Calculated band structure in the $k_z = \pi$ plane for the ARPES-based tight binding model. a) Band dispersions along the $Z-A$ direction. b) Fermi surface at $k_z = \pi$. c) Fermi surface for the hole pocket (left) and electron pocket (right) as a function of k_z along the k_x axis.

3.4(e), the band dispersion is presented, which agrees quantitatively with measured ARPES data near the Fermi level. It is noted that, experimentally, this d_{xy} band is predicted to the the most renormalised, compared to a DFT framework, and should be less dispersive between the Γ and M point than described by this set of hopping parameters [102]. This is a fundamental limitation of the model used, however, for features within $\pm$50 meV of the Fermi level, the model is in very good agreement with experiment. The Fermi surface, presented in 3.4(f), correctly describes the very small hole and electron pockets, with a single hole pocket at the Γ point, in agreement with the experimental results.

This model also correctly describes the k_z dispersion of FeSe. In Fig. 3.5(a), the calculated $Z-A$ band dispersion is shown for the $k_z = \pi$ plane. Again, in very good agreement with the band dispersions extracted from experimental data, shown as orange crosses. The Fermi surface, presented in Fig. 3.5(b), also correctly describes the two hole pockets at this value of k_z [102]. Both the hole and electron pockets are larger than in the $k_z = 0$ plane, as shown in Fig. 3.5(c) where the calculated k_x vs k_z Fermi surface of the hole and electron pockets is shown.

This model will now be used throughout the remainder of the thesis.

3.5 Temperature dependence of the chemical potential in FeSe

The description of the electronic structure of FeSe, that has been developed here, describes a system where the top of the hole bands and bottom of the electron bands sit very close to the Fermi level. At the centre of the Brillouin zone, the two hole bands have band maximas of +7 meV and -13 meV at $k_z = 0$ and +30 meV and +10 meV at

$k_z = \pi$. At the corner of the Brillouin zone, the minimas are located at -26 meV and -46 meV at both $k_z = 0$ and $k_z = \pi$.

The shallow nature of the hole and electron pockets suggest that the temperature dependence of the chemical potential may become an important quantity. The chemical potential of a system is often assumed to be a constant value. This is a good approximation in systems where the density of states is relatively uniform around the chemical potential, like in the DFT-based tight binding model described in Fig. 3.4(b). However, when shallow bands are present, a change in temperature can produce an anisotropic population of thermally active hole and electron carriers, which will necessitate a shift in the chemical potential to conserve the charge of the system. This temperature dependent chemical potential shift has been measured in other iron-based superconductors such as $Ba(Fe_{1-x}Co_x)_2As_2$ [147], $Ba(Fe_{1-x}Ru_x)_2As_2$ [148] and $FeSe_{1-x}S_x$ [149].

As a quantitatively accurate tight binding model of FeSe is now present, it should be possible to predict the magnitude of the temperature dependent shift that will be observed in FeSe. In this section I will calculate the predicted changes to the electronic structure as a function of temperature between 100 K and 300 K. I will then perform a temperature dependent ARPES study to test this theoretical prediction.

3.5.1 Calculated temperature dependence of the chemical potential

To determine the evolution of the chemical potential, the total number of electrons, N, is calculated,

$$N = 2\sum_k \sum_\nu f(E_\nu(k) - \mu(T)). \tag{3.17}$$

Here, ν is the band index, $E_\nu(k)$ is the energy of the band ν at momentum $\mathbf{k}$, $f(E_\nu(\mathbf{k}) - \mu(T))$ is the Fermi function and $\mu(T)$ is the temperature dependent chemical potential. The value of the chemical potential at 100 K is set to $\mu(100\text{ K}) = 12$ meV in order to agree with the experimental Fermi cut off. Using this value, N was determined to be $12.00e^-$, in agreement with the total number of electrons available from two Fe^{2+} atoms in a 2-Fe unit cell.

As a function of temperature the number of electrons can not change, else the system would gain charge. Therefore N is fixed to $12.00e^-$ and Eq. (3.17) is solved self consistently for the chemical potential at a given temperature. In Fig. 3.6(a), the relative shift to the chemical potential is plotted as a function of temperature, as predicted from the ARPES-based tight binding model. This is compared with the

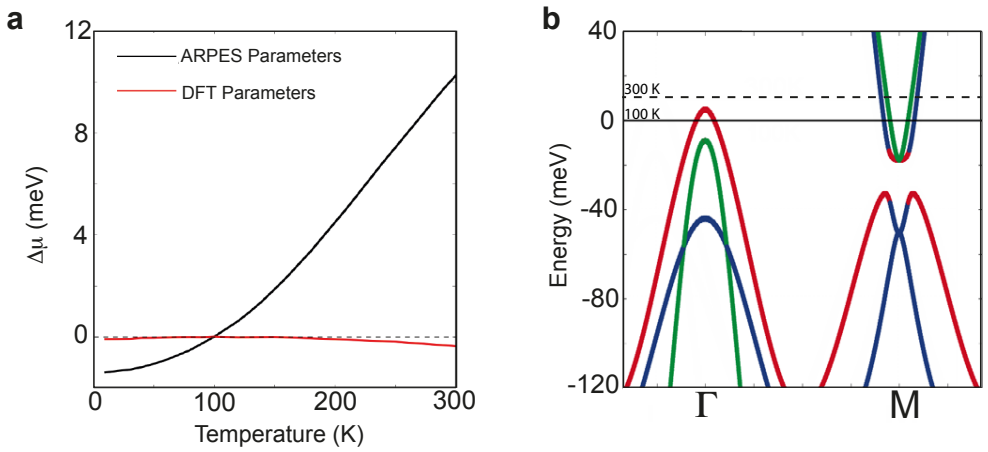

Figure 3.6: a) Shift of the chemical potential as a function of temperature predicted using the ARPES-based parameter set (black line), compared to a set of DFT-based hopping parameters (red line). $\Delta\mu$ is determined relative to the 100 K value. b) Band dispersions along $\Gamma - M$ indicating the predicted location of the chemical potential at 100 K and 300 K.

prediction from the same tight model using the DFT-based hopping parameters. The ARPES-based parameters predict a 10 meV increase to the chemical potential between 100 K and 300 K, whereas the DFT-based model suggests a negligible -0.4 meV shift. This highlights an important difference between these two models.

In FeSe, a 10 meV rigid shift to the chemical potential would imply that the maximum binding energy of the outer hole pocket at the Γ point will have moved entirely below the chemical potential by 300 K, as shown in Fig. 3.6(b). If this is true, the effect should be noticeable in ARPES measurements.

3.5.2 Temperature dependent ARPES study

To confirm this theoretical prediction, a temperature dependent ARPES study on single crystals of FeSe has been performed. If a rigid chemical potential shift does occur, the k_F value of the hole pocket should decrease with increasing temperature and, oppositely, the k_F value of the electron pocket should increase. In Fig. 3.7, the hole and electron pocket, close to the high-symmetry Z and A point, is measured for temperatures between 100 K and 300 K. A photon energy of 56 eV has been used, this corresponds to $k_z \approx \pi$, where the pockets are largest and should therefore be easiest to observe changes in k_F. At 100 K, the two hole pockets can be observed, which is correctly described in the ARPES-based model, shown in Fig. 3.5(b). The two over-

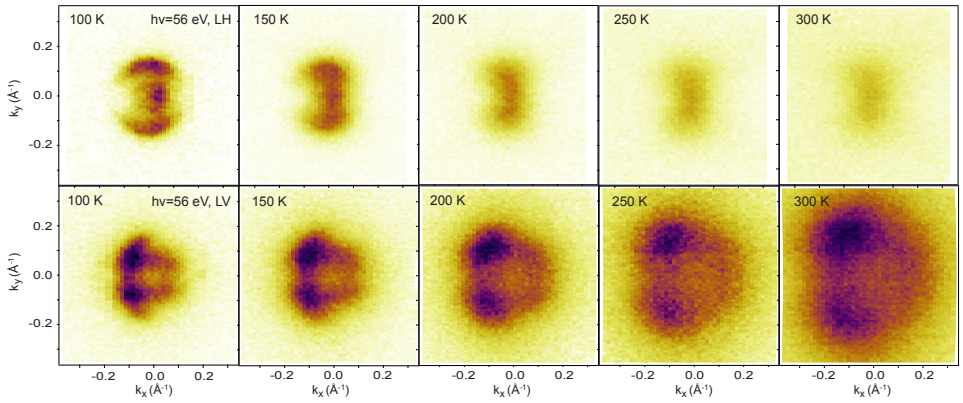

Figure 3.7: a) Temperature-dependent Fermi surfaces of the hole pocket (top row) and electron pocket (bottom row), taken at a photon energy of 56 eV between 100 and 300 K. The axes are defined relative to the centre of the pocket.

lapping ellipses of the electron pockets can also be seen. By $\sim$ 200 K the inner hole pocket has disappeared below the chemical potential, followed by the outer hole pocket by $\sim$ 300 K. Conversely, the electron pocket appears to get larger as the temperature increases. This is in agreement with a rigid shift of the chemical potential described by our model.

To confirm the loss of the hole pocket below the chemical potential, the experimentally extracted k_F values for the hole and electron pocket are plotted in Fig. 3.8(c,d). Assuming the hole band dispersions are quadratic, the k_F value of the hole pocket should decrease with a square root behaviour as a function of temperature. The square root function fitted to the data in Fig. 3.8(c) (blue lines) shows that both the inner and outer hole pocket are in agreement with this behaviour. For the electron pocket, the band dispersions in the vicinity of the chemical potential are approximately linear and, as a result, the k_F value is expected to be increase linearly with increasing temperature. This is in agreement with the results from Fig. 3.8(d).

To quantify the chemical potential shift, the energy distribution curves (EDC), taken at the centre of the high symmetry momenta of the Z and A point, are analysed in Fig 3.8(a,b). For the Z point, two main peaks are observed, a large d_{z^2} peak at $\sim$ 220 meV and a mixture of d_{xz}, d_{yz} and d_{xy} bands near the Fermi level. For the A point, only a single peak composed of a mixture of d_{xz}, d_{yz} and d_{xy} bands near the Fermi level is observed. For all bands there is a decrease in the maximum peak position as a function of temperature. By extracting the peak position for the d_{z^2} band at the Z point, which is composed of only a single band and is situated far away from the Fermi

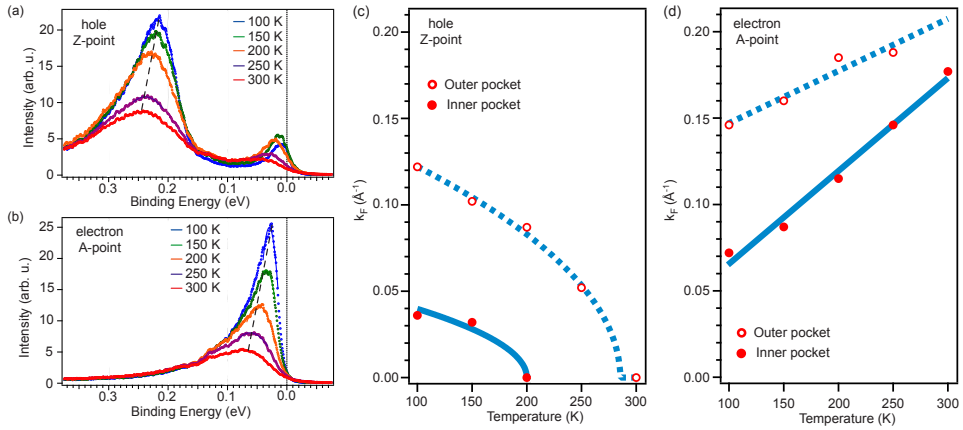

Figure 3.8: Data analysis of chemical potential shift. EDC taken along the high symmetry momentum of a) the Z-point and b) the A-point as a function of temperature. c) The extracted k_F values of the hole pocket (Z-point). d) The extracted k_F values of the electron pocket (A-point).

level, a linear decrease of $\sim$ -0.13 meV/K is extracted, leading to a 25 meV increase to the chemical potential between 100 K and 300 K. This is over twice as large as the 10 meV shift predicted from the ARPES-based tight binding model.

As the ARPES-based tight binding model accurately describes the important features that effects the temperature dependence of the chemical potential, it is unlikely that the discrepancy between the 10 meV theoretical chemical potential shift and the 25 meV experimental chemical potential shift arises from the numerical inaccuracies of the model. A more likely scenario is that a temperature-dependent self energy, that is neglected within these theoretical calculations, would account for the enhanced increase.

Such correlation effects could lead to a reduction of the coherent quasiparticle weight with increasing temperature which would decrease the density of states of the system. In this scenario a greater shift to the chemical potential will be required to ensure charge conservation. Evidence for the importance of the temperature dependence of the self energy has been shown in previous theoretical calculations of $BaFe_2As_2$ [150, 151]. The increase in the self energy can also be observed when studying the experimental band dispersions as a function of temperature. In Fig. 3.9 the width of the bands increases with increasing temperature, this implies that the imaginary part of the self energy has also increased. It is likely that the temperature dependence of the self energy can not be ignored at high temperatures.

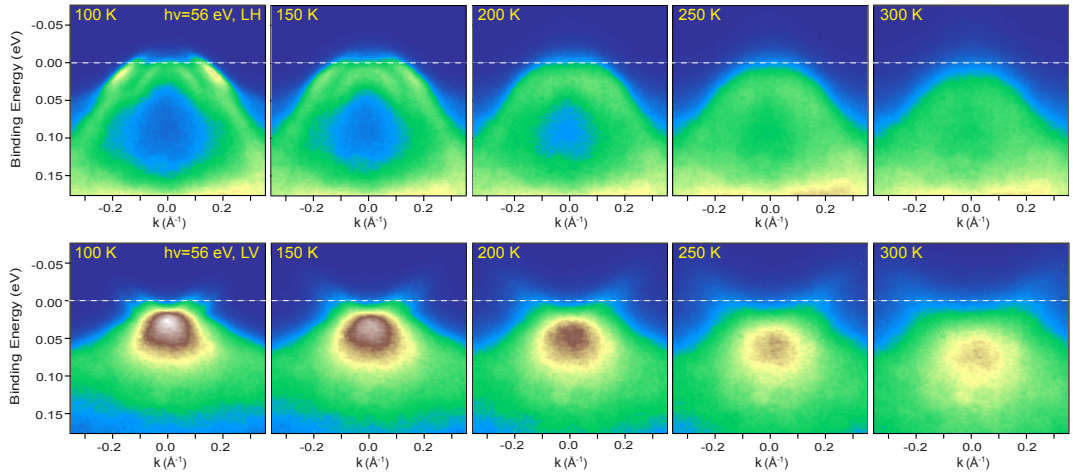

Figure 3.9: Temperature dependence of the band dispersions of FeSe between 100 K and 300 K. Top row - The Z point at $h\nu$ =56 eV using LH polarised light. Bottom row - The A point at $h\nu$ =56 eV using LV polarised light.

3.5.3 Doping effects of the chemical potential

Doping is another parameter which will affect the chemical potential and can be studied using the ARPES-based model. In Fig. 3.10(a) the calculated change in the chemical potential, predicted as a function of hole and electron doping, is presented. To model the influence of doping, the value of N, in Eq. (3.17), is altered. The doping is defined as a percentage of an electron such that 1% doping is equal to $0.01e^{-}$.

An asymmetric shift to the chemical potential between hole and electron doping is calculated. For electron doping values of 24%, a 100 meV increase to the chemical potential is predicted, assuming that the temperature is held constant at 100 K. Whereas 24% hole doping only produces a -60 meV shift to the chemical potential. This is a consequence of the fact that the density of states per meV is larger below the chemical potential than above, such that more states must be removed per meV to alter the chemical potential.

Interestingly, the hole and electron doped systems are predicted to have an opposite effect on the temperature dependence of the chemical potential. As shown in Fig. 3.10(b), the hole doped systems (as well as the undoped system) show an increase in the chemical potential at temperature increases whereas, for electron doped systems, the chemical potential decreases as a function of temperature. This can be understood in an analogous way to the neutral FeSe, as the system becomes more electron doped, there are less hole states to ensure a conservation of charge with increasing tempera-

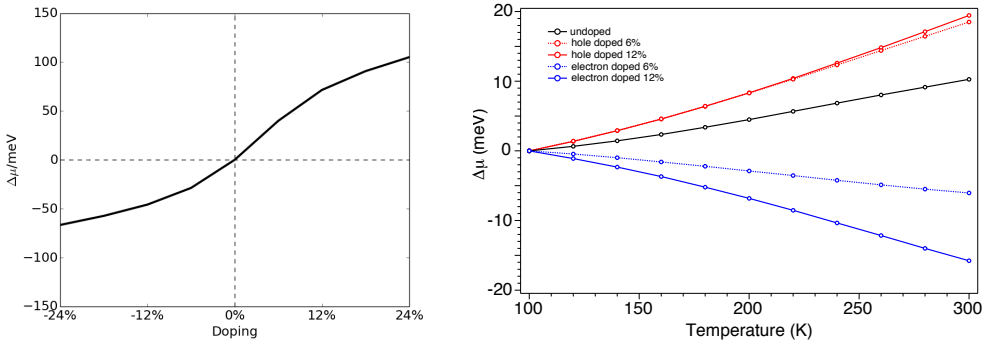

Figure 3.10: a) Calculated change to the chemical potential, Δ_μ, as a function of doping. The temperature is fixed to 100 K. b) Temperature dependence of the chemical potential for hole doped systems (red lines), the undoped system (black line) and electron doped systems (blue lines).

ture. To compensate, the chemical potential actually decreases to ensure that charge is conserved. This effect has been experimentally observed in the doping behaviour of the chemical potential in $Ba(Fe_{1-x}Co_x)_2As_2$ [147].

3.5.4 Comparison with experimental literature

During the preparation of the manuscript for the work presented in this chapter, Kushnirenko *et. al.* [152] presented a study of the temperature dependence of the electronic structure of FeSe . They report, an opposite shift in binding energy between 100 K and 300 K for the hole and electron bands. The hole bands are claimed to increase in binding energy by 25 meV and the electron bands are claimed to decrease by 25 meV. This conclusion disagrees with our experimental data, where both bands are observed to decrease by 25 meV, which we have interpreted as a rigid shift to the chemical potential.

In response to this disagreement, Pustovit *et. al.* [153] performed an independent study of the temperature dependence of the hole bands of single crystals of FeSe and a tellurium doped $Fe_{1.05}Se_{0.84}Te_{0.16}$ sample [154]. By studying the Z point, using photon energies of 21 eV, Pustovit *et. al.* observed that the hole bands continuously decreased in binding energy between 100 K and 250 K in both systems. This result is in agreement with our experimental conclusions and additionally the conclusions obtained from the sulphur doped $FeSe_{0.945}S_{0.055}$ measured by Adbel-Hafiez et. al. [149].

3.6 Discussion

The ARPES-based tight binding model, developed in this chapter, provides an accurate description of the low energy quasiparticle band dispersions of FeSe and, importantly, highlights the large discrepancy between a DFT-based model and experimental measurements. However, this model does have some limitations. This model can not explain what causes the large renormalisation between the non-interacting, bare band dispersion and the measured ARPES data. It is also not possible to comment on the reliability of the tight binding description of the bands above the Fermi level, or far below the Fermi level. That being said, for experimental features which depend on an exact description of the Fermi surface, such as superconductivity, this model will provide a precise description of the experimental electronic structure at low temperatures.

At high temperatures, the temperature dependence of the self energy has also been shown to be important when it comes to accurately describing the electronic structure of FeSe at room temperature [144]. This may be important for features of FeSe above 100 K, however, for properties that occur below 100 K, the low temperature limit will be adequate to describe the electronic structure of FeSe.

Despite most theoretical treatments to date ignoring the effects of the chemical potential, the large sensitivity of this property as a function of temperature may be important for the theoretical modelling of electron doped systems [155] and monolayers [67], where T_c can fluctuate between 8 K and 65 K. As this model underestimates the experimental temperature dependence of the chemical potential in bulk FeSe, it is likely that the predicted temperature dependence of the chemical potential in hole and electron doped systems will be even larger than the values that have been calculated here. The importance of the sensitive chemical potential in these systems can not be overlooked and, as we will be discussed in the next chapter, will directly affect the electronic structure of the low temperature nematic phase.

3.7 Conclusion

In this chapter I have developed a tight binding model which quantitative describes the experimentally observed band dispersions of FeSe in the tetragonal phase at 100 K. In particular this model captures the shallow bands around E_F which predicted a very sensitive chemical potential, not captured within a DFT-based framework. I have then experimentally confirmed this prediction by observing a 25 meV shift to the chemical

potential, between 100 K and 300 K, in ARPES measurements of FeSe [144]. This model can now be modified to account for the symmetry breaking effects of the nematic and superconducting states.

4 | Effect of nematicity on the electronic structure of FeSe and NaFeAs

4.1 Introduction

Below $T_s = 90$ K, FeSe exhibits a spontaneous, nematic, C_4 rotational symmetry breaking phase. This phase induces a structural transition between a tetragonal and orthorhombic lattice [99] and generates large anisotropic signatures in resistivity measurements [114], Knight shift experiments [156] and the electronic structure measured by both ARPES [100, 118–120] and QPI [157–159]. Currently the microscopic original of the rotational symmetry breaking state is not known [73], however, it has been suggested that it may originate from electronic degrees of freedom rather than from the lattice distortion [72]. This is due to the fact that the anisotropy of the lattice constants is only 0.3% [75] at low temperatures, which is much smaller than what would be necessary to produce the large anisotropic responses measured in experiment [145]. So far, both orbital [156, 160] and spin [116, 161] mechanisms have been proposed as the potential origin of nematicity, however no consensus has been reached [162].

In order to correctly model the superconducting properties of FeSe, the tight binding description must first correctly describe the electronic structure of FeSe within the nematic state. In this regard, following a similar philosophy to the previous chapter, this chapter will be spent studying the evolution of the electronic structure upon entering the nematic state, as measured by ARPES [102, 163].

The analysis of ARPES data of the nematic state of FeSe is, however, complicated by the newly formed orthorhombic lattice. This new crystal symmetry will induce structural domains within the sample, with each domain rotated by 90° with respect to its neighbour. These domains are typically smaller than the spot size of a conventional photon beam used in ARPES experiments [164]. As a consequence, ARPES data of the nematic state will generally consist of a superposition of photoelectrons arising

from two 90° rotated structures. This introduces ambiguity when determining which band arises from which domain.

It is possible to overcome this issue by applying uniaxial strain to the orthorhombic crystal. This will align a majority of the orthorhombic domains along the axis of strain allowing for the possibility to study the electronic structure where all the domains are in oriented in the same direction. Due to the technical challenges posed by measurements on crystals under uniaxial strain, most ARPES data of the nematic state of FeSe has been performed on twinned crystals, and the electronic structure of a single domain has had to be interpreted from this.

In this chapter, I will aim to understand the electronic structure of the nematic phase of FeSe by closely studying the recent experimental work on both unstrained (twinned) crystals [96, 102, 165] and strained (detwinned) crystals [163]. I will use this information to develop a phenomenological nematic order parameter which can quantitatively describe the experimental temperature dependent band shifts that are observed in ARPES data of twinned crystals.

I will then focus on the surprising anisotropy observed in ARPES measurements on detwinned crystals of FeSe. Whilst theoretical models of the nematic state of FeSe conventionally describe a Fermi surface consisting of one hole pocket and two electron pockets [145, 146], ARPES measurements on detwinned crystals reveal a Fermi surface consisting of one hole pocket and only one electron pocket. I compare this experimental result with the tight binding model and discuss what needs to be phenomenologically included in order to correctly describe the experimental measurements.

Finally, I discuss the electronic structure of detwinned crystals of NaFeAs, which exhibits a nematic phase at $T_s = 54$ K and an antiferromagnetic state at $T_s = 43$ K. A similar anisotropic behaviour at the Fermi surface of NaFeAs is observed, such that only one of the two electron pockets contributes to the Fermi surface below T_s. This suggests that the lack of a second electron pocket may be a generic feature of the nematic state.

The experimental data of FeSe presented in this chapter was obtained and processed by Matthew Watson and Timur Kim. The theoretical analysis however is my own. For the ARPES study of detwinned crystals of NaFeAs, I personally contributed to the experimental measurement of the sample.

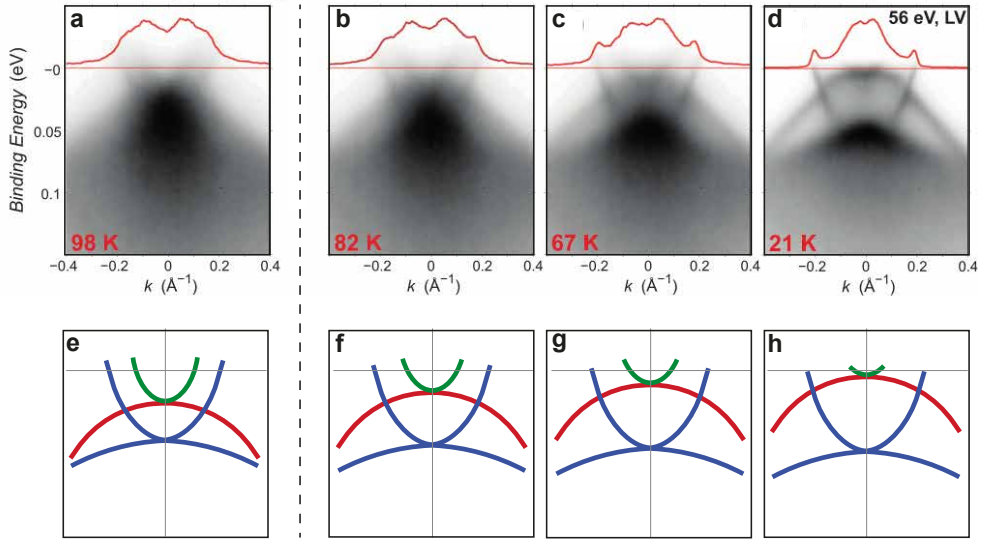

Figure 4.1: Temperature evolution of the M point of FeSe at 56 eV using LV polarised light, adapted from Ref. [102]. a) Tetragonal phase electronic structure at 98 K. b) Nematic phase electronic structure at 82 K. c) 67 K and d) 21 K. The MDC's integrated around the Fermi level are presented as red curves showing two distinct bands crossing the Fermi level at every temperature. e-h) Cartoons corresponding to the temperature dependent band dispersions suggested by the ARPES data. Here the colours correspond to the maximum orbital character of the band with red: d_{xz}, green: d_{yz}, blue: d_{xy}.

4.2 Temperature dependence of the electronic structure of FeSe

In this section, I will review the experimental ARPES data of the nematic state of FeSe, focusing on twinned crystals. in these unstrained crystals, careful temperature dependent studies of the electronic structure have been performed [96]. I will use this data to determine the magnitude and symmetry of the nematic order parameter that will reproduce the experimental electronic structure within the tight binding framework.

4.2.1 Electron bands

In the tetragonal phase, it was observed that two bands crossed the Fermi level at the M/A point of FeSe. This resulted in two degenerate saddle points separated by 20 meV [144]. The upper saddle point consisted of a d_{xz} and a d_{yz} degenerate band, and the lower saddle point consisted of two d_{xy} bands.

This was not entirely clear from previous data sets on FeSe [100, 118–120]. In these earlier reports, it was believed that the M/A point consisted of only a single saddle point, of degenerate d_{xz} and d_{yz} orbital character, and the lower d_{xy} saddle point was

unobservable. On cooling the sample down to low temperatures (< 20 K), these reports observed two bands at the M/A point separated by 50 meV [100, 118–120], which led the authors of these manuscripts to suggest that a 50 meV symmetry breaking nematic splitting of the the d_{xz} and d_{yz} states had occurred.

The re-evaluation of the electronic structure in the tetragonal phase, where both the d_{xz}/d_{yz} and d_{xy} bands are observed, called for a more detailed study of the temperature dependence of the M/A point [102]. In Fig. 4.1, the results of the temperature dependent study of the A point are shown. This data was measured using LV polarised light and with a photon energy of $h\nu = 56$ eV. At 98 K, in Fig. 4.1(a), two separate bands can be observed crossing the Fermi level, indicating two individual saddle points at the A point within the tetragonal phase, as discussed in Section 3.3. To clarify the electronic structure, in Fig. 4.1(e) a cartoon of the band dispersion corresponding to Fig. 4.1(a) is shown.

As the system is cooled below the nematic transition (Fig. 4.1(b-d)), the upper saddle point is observed to increase in binding energy, by around 20 meV. Conversely, the lower saddle point slightly decreases in binding energy by around 10 meV. At 21 K, two saddle points are still observed. This is illustrated in the cartoons of Fig. 4.1(f-h). A temperature dependent analysis of the data is also shown in Fig. 4.2(b).

From this data, it was determined that no symmetry breaking band splitting at the A point could be detected (within experimental resolution). Moreover, the 50 meV splitting, that had been reported in the literature [100, 118–120], appeared to arise from a combination of the already present 20 meV separation in the tetragonal state, an additional $\sim$20 meV upward shift to the upper saddle point and a 10 meV downward shift to the lower saddle point. In total, a 30 meV increase in separation of the two saddle points was detected.

It must be noted that Fig. 4.1 describes data obtained from a twinned sample of FeSe, therefore it is not possible to determine which bands arise from which orthorhombic domain. Nevertheless, if a d_{xz}/ d_{yz} band splitting had occurred, ARPES data on twinned crystals would be able to observe this effect by measuring a doubling of the bands at low temperatures. This would arise as the electron bands would no longer be C_4 symmetric and thus the two 90° rotated domains would produce two different band dispersions. This is not detected in this data set.

4.2.2 Hole bands

At the A point, it appeared that there was a 30 meV increase to the separation of the two degenerate saddle points, with a symmetry conserved upwards shift to the degenerate d_{xz} and d_{yz} states. For the hole bands, however, the d_{xz} and d_{yz} states are already split by the presence of a 20 meV spin orbit interaction [90, 100]. This pushes the d_{xz} state above the Fermi level, making it challenging to truly detect the maxima using photoemission. This challenge was overcome by Watson et. al. [165]. Here, the authors performed a Laser-ARPES study of FeSe at the Γ point, where the maxima of the hole band is only 7 meV above the Fermi level. This is shallow enough that thermally excited electrons can still populate the top of the hole band at finite temperatures, albeit with a reduced intensity. This allowed the authors to track the evolution of this band position upon entering the nematic phase. They concluded that the separation between the d_{xz} and d_{yz} bands increases from 20 meV at 100 K, to 37.5 meV at 10 K. Indicating a 17.5 meV increase to the splitting of these states.

This increase in splitting, however, is not equivalent to the strength of the nematic ordering. Due to the already finite spin orbit interaction, any additional ordering will add in quadrature with the magnitude of the spin orbit coupling,

$$\Delta E = \sqrt{\Delta_{SO}^2 + \Delta_{nem}^2}. \tag{4.1}$$

Thus, given that the bands at 10 K are split by $\Delta E = 37.5$ meV and assuming that the spin orbit interaction, Δ_{SO}, is temperature independent, and fixed at a value of 20 meV [90, 100], the authors concluded that the nematic ordering strength, Δ_{nem}, reached 29 meV at at 10 K. Their temperature dependent results for the Γ point are presented in Fig. 4.2(a).

Evidence for a chemical potential shift in the nematic state

In the same laser ARPES paper measuring the Γ point of FeSe, It was also observed that the d_{xy} band, located at around -40 meV at 100 K, decreases by 10 meV [165]. This is equivalent to the 10 meV decrease of the d_{xy} band observed at the A point [102]. A momentum independent shift at both the centre and corner of the Brillouin zone, hints at a possible change in the position of the chemical potential, induced by the nematic ordering. This would be similar to the temperature dependent shift observed in Chapter 3 [144]. On this assumption, the observed 20 meV increase to the degenerate d_{xz} and d_{yz} states at the A point would actually be a 30 meV increase, plus a 10 meV shift to

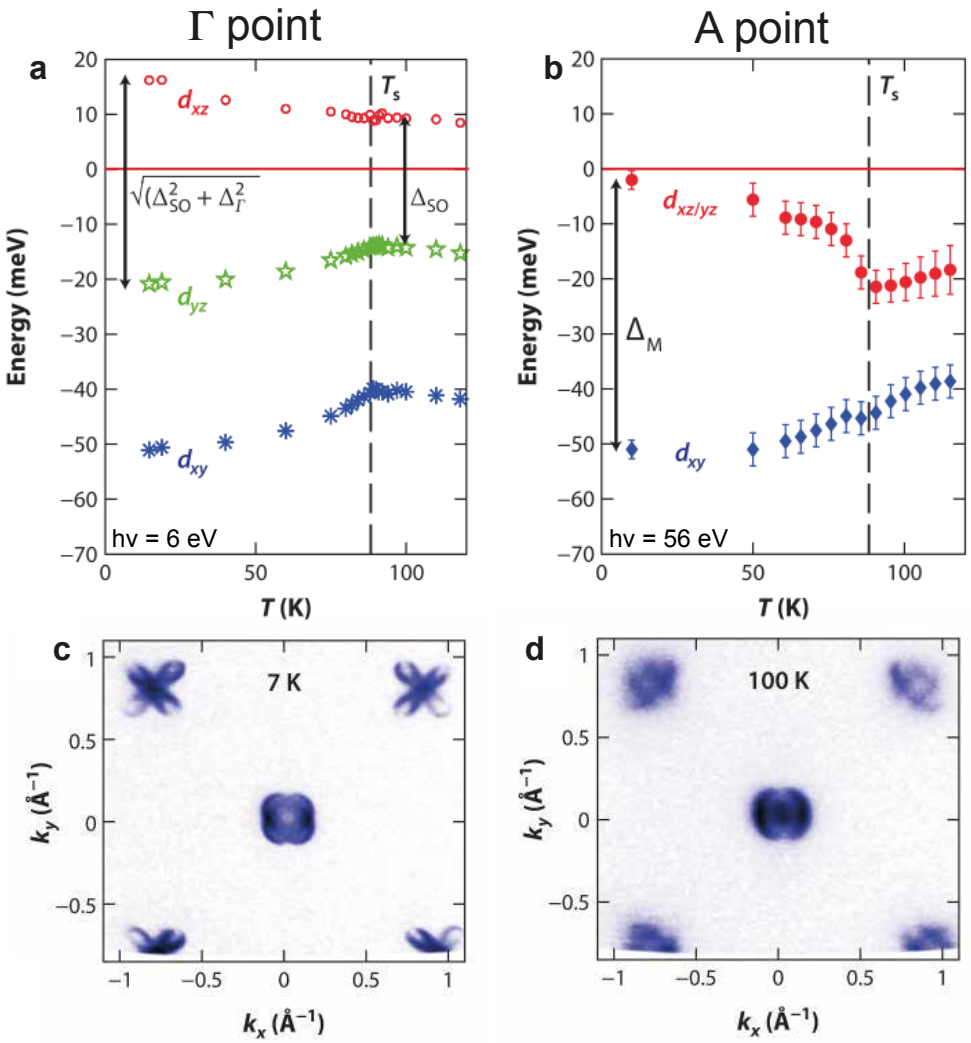

Figure 4.2: Summary of the temperature evolution of the electronic structure of FeSe. a) Temperature dependence of the hole bands of FeSe, reproduced from Ref. [165]. Here, red labels the d_{xz} band, green is the d_{yz} band and dark blue is the d_{xy} band. b) Temperature dependence of the electron bands, reproduced from Ref. [102]. Here, red labels the degenerate d_{xz}/d_{yz} state and dark blue labels the d_{xy} band. c) Fermi surface of a twinned sample of nematic FeSe at 7 K. d) Fermi surface of the tetragonal phase of FeSe at 100 K, reproduced from Ref. [163].

the chemical potential. This would then imply that the magnitude of nematic ordering at both the hole and electron pockets is of the order of 30 meV. I will therefore use this value as the energy scale for describing nematic ordering in FeSe.

4.2.3 Fermi surface

The Fermi surface of the tetragonal phase of FeSe has been previously discussed in Chapter 3. It consists of one or two hole pockets at the centre of the Brillouin zone, depending on k_z, and two overlapping oval shaped electron pockets at the corner of the Brillouin zone. On cooling the system into the nematic phase, the inner hole pocket, which is present at 56 eV ($k_z \approx \pi$) in Fig. 4.2(d), moves below the Fermi level due to the increased nematic splitting. The outer, spherical, hole pocket is observed to elongate to form an ellipse. In Fig. 4.2(c) two 90° rotated ellipses are observed at the centre of the Brillouin zone. This is a consequence of measuring a twinned crystal. Here, it is assumed that there is one ellipse per orthorhombic domain, this assumption will be tested in Sec. 4.4.

At the corner of the Brillouin zone, the two 90° rotated elliptical electron pockets have both evolved into peanut shaped features, where the ellipses have been pinched in at the sides, this corresponds to the symmetry preserved shift of the bands described in Fig. 4.2(b). As this is a twinned sample, a doubling of the bands due to the presence of the two orthorhombic domains would also be expected. However, only two electron pockets can be observed at 7 K. This would seem to imply that the electron pockets retain C_4 symmetry and that the states arising from both orthorhombic domains directly overlap. This claim will again be tested in Sec. 4.4.

The four figures of Fig. 4.2 completely describe the temperature dependence of the electronic structure of a twinned sample of FeSe. The observed symmetry of the band shifts, as well as the 30 meV nematic ordering energy scale will now be used to determine an order parameter that can describe the electronic structure of the nematic state.

4.3 Determination of the nematic order parameter for FeSe

A theoretical analysis of the symmetry breaking effects of nematic ordering has been studied in detail by Ref. [166, 167]. Here, the authors suggest a large number of possible forms the nematic order parameter could take, and the corresponding consequences each nematic order parameter may have on the electronic structure of FeSe. Now that a complete set of experimental data has been obtained, it is possible to apply the various forms of nematic ordering to the ARPES-based tight binding model, that describes the tetragonal phase, and compare the consequences with the experimental results.

The order parameters are included into the tight binding model as $H_{tb} + \Delta(T)h$

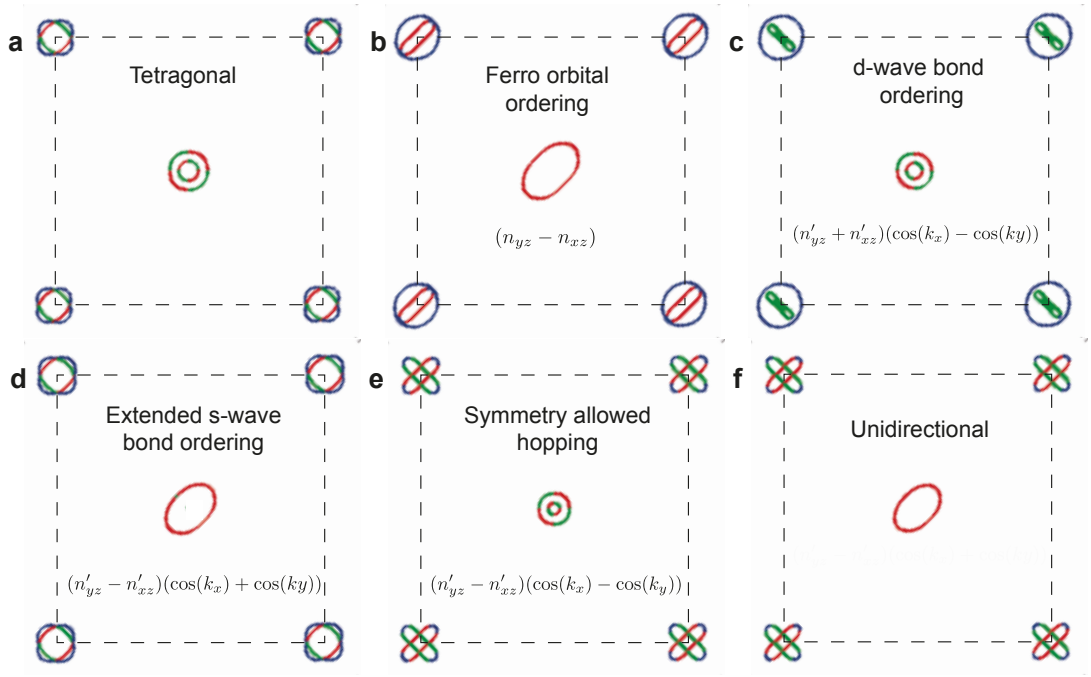

Figure 4.3: Comparison of the effects that nematic order parameters would have on the Fermi surface of FeSe. a) Modelled Fermi surface of the tetragonal phase of FeSe at $k_z = \pi$. b) Fermi surface with added ferro-orbital order with $\Delta_{nem} = 29$ meV. c) Fermi surface with added d-wave bond ordering with $\Delta_{nem} = 14.5$ meV. d) Fermi surface with an extended s-wave bond ordering term of $\Delta_{nem} = 14.5$ meV. e) Fermi surface with a symmetry allowed hopping, which only effects the electron pockets, $\Delta_{nem} = 29$ meV. f) The experimental nematic order parameter combining the orderings from (d) and (e), $\Delta_{nem} = 29$ meV. Here the colour describes the maximum orbital content of the band, green = d_{yz}, red = d_{xz} and blue = d_{xy}.

where $\Delta(T) = \Delta(0)\sqrt{1 - \frac{T}{T_s}}$, and $\Delta(0)$ =30 meV. The order parameter symmetry is defined as h. The most common types of nematic order suggested in the literature, these are

- Ferro orbital ordering : $h = (n_{yz} - n_{xz})$ [146, 168, 169]
- d-wave bond ordering : $h = (n'_{yz} + n'_{xz})(cos(k_x) - cos(k_y))$ [120, 167, 170]
- Extended s-wave bond ordering: $h = (n'_{yz} - n'_{xz})(cos(k_x) + \cos(k_y))$ [166, 167].

Here, $n_\alpha = c^\dagger_{\alpha i} c_{\alpha i}$ is the second quantization number operator for orbital α on atomic site i, in the 2-Fe unit cell, and $n'_\alpha = c^\dagger_{\alpha i} c_{\alpha j} + c^\dagger_{\alpha j} c_{\alpha i}$ defines the off diagonal bond operator between neighbouring sites.

In Fig. 4.3, the Fermi surfaces suggested from these various forms of nematic ordering are presented. In Fig. 4.3(a), the modelled Fermi surface of the tetragonal

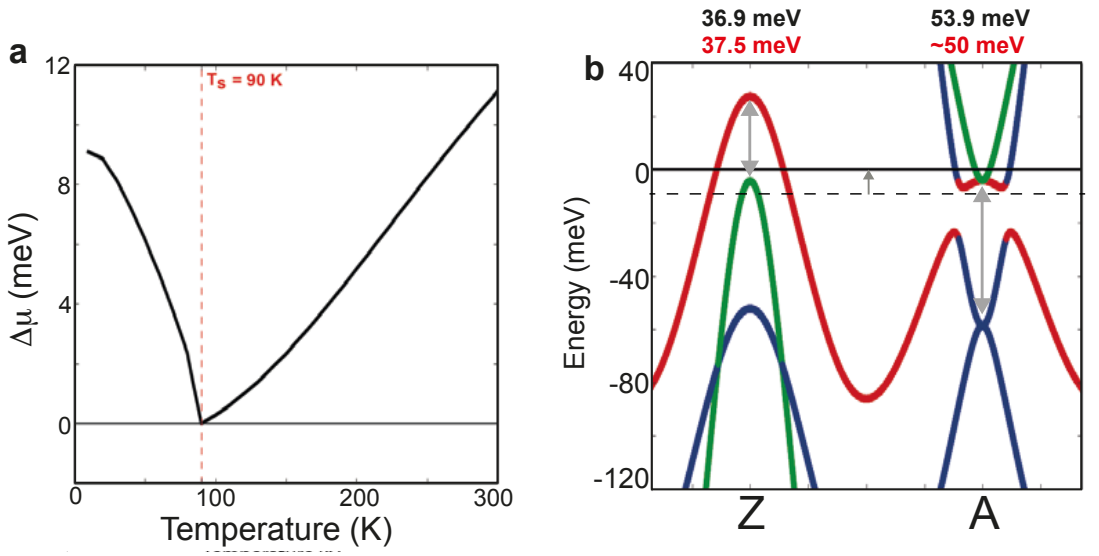

Figure 4.4: Model of FeSe with the phenomenological nematic order parameter. a) Calculated chemical potential shift of FeSe as a function of temperature compared to the 90 K value. Below 90 K the nematic order parameter is switched on with a mean-field temperature dependence $\Delta_{nem}(T) = \Delta_{nem}(0)\sqrt{1-\frac{T}{T_s}}$ where $\Delta_{nem}(0) = 29$ meV. b) Calculated band dispersions along the Z-A direction in the nematic phase, the black numbers above the high symmetry points correspond to the calculated band splittings, shown with a grey double headed arrow. The red values describe the experimental values. Here the colour describes the maximum orbital content of the band, green = d_{yz}, red = d_{xz} and blue = d_{xy}.

phase ($h = 0$) is shown for comparison. In Fig. 4.3(b), the predicted Fermi surface in the presence of a ferro-orbital ordering term is shown, which defines a momentum-independent splitting of the population of the d_{xz} and d_{yz} states. It can be seen that the hole pocket elongates into an elliptical shape, as suggested by experiment. However, this order parameter also induces a symmetry breaking effect at the electron pockets, giving rise to a small peanut shaped electron pocket and a large spherical electron pocket. This does not agree with the twinned Fermi surface presented in Fig. 4.2(c). In Fig. 4.5(c), the predicted Fermi surface in the presence of a d-wave order parameter is shown. Here, the hole states are not affected by the ordering, and remain spherical, whereas the electron pockets experience a degeneracy breaking splitting between the d_{xz} and d_{yz} states. This does not agree with our experimental results. In Fig. 4.3(d), the Fermi surface in the presence of an extended s-wave bond ordering term is shown. This form of symmetry breaking correctly accounts for the elongation of the hole pocket, but does not produce an effect the electron pockets.

Out of all the order parameters considered, none of the symmetry breaking terms

preserve the C_4 symmetry of the electron pockets. This is with the exception of the extended s-wave bond ordering term, which doesn't alter the electron pockets from the tetragonal state. To overcome this a symmetry allowed hopping term $\Delta_{nem}(n'_{xz} - n'_{yz})(\cos(k_x) - \cos(k_y))$ is introduced which correctly reproduces the shifts to the electron pockets observed in twinned crystals, but does not affect the hole states. This is shown in Fig. 4.3(e). By combining the extended s-wave bond ordering term of Fig. 4.3(d) with this symmetry allowed hopping term, we arrive at a form for the nematic order parameter which agrees with the experimental results. This is shown in Fig. 4.3(f).

The experimental nematic order parameter is defined

$$\frac{\Delta_{nem}}{4}(n'_{yz} - n'_{xz})(\cos(k_x) + cos(k_y)) + \frac{\Delta_{nem}}{2}(n'_{yz} - n'_{xz})(\cos(k_x) - cos(k_y)). \qquad (4.2)$$

Here, an additional factor of two in the symmetry breaking extended s-wave term has been included, which counters the doubling of the splitting which would otherwise occur between the hole bands. This then quantitatively reproduces the 37.5 meV splitting of the hole bands as observed in experiment [165]. If this additional factor of two was not required, then Eq. (4.2) could be simply reduced to $\Delta_{nem}(n'_{yz} - n'_{xz})\cos(k_x)$, which was reported in Ref. [102].

In Fig. 4.4(b), the band structure described by the tight binding model in the presence of the experimental nematic order parameter is presented. This model describes a 36.9 meV splitting between the hole bands, and a 53.9 meV gap between the saddle points of the electron bands. This quantitatively reproduces the experimental dispersions.

Finally, to test if the observation of a momentum independent downward shift of the d_{xy} band is a chemical potential effect, the shift to the chemical potential is calculated as a function of temperature. It is assumed that the nematic order parameter behaves with a mean field temperature dependence, which becomes finite below $T_s = 90$ K. By applying the temperature dependent experimental order parameter, and repeating the calculations from section 3.5.1, it is suggested that the chemical potential will increase by 9 meV between 90 K and 10 K. This is shown in Fig. 4.4(a). This value is in quantitative agreement with the downward shift observed for the d_{xy} band in Fig. 4.2(a) and (b). Therefore, the experimental nematic order parameter can account for all the observed features on the electronic structure, based on ARPES data of twinned crystals of FeSe. By applying Eq. (4.2) to the tight binding model developed in Chapter 3, we

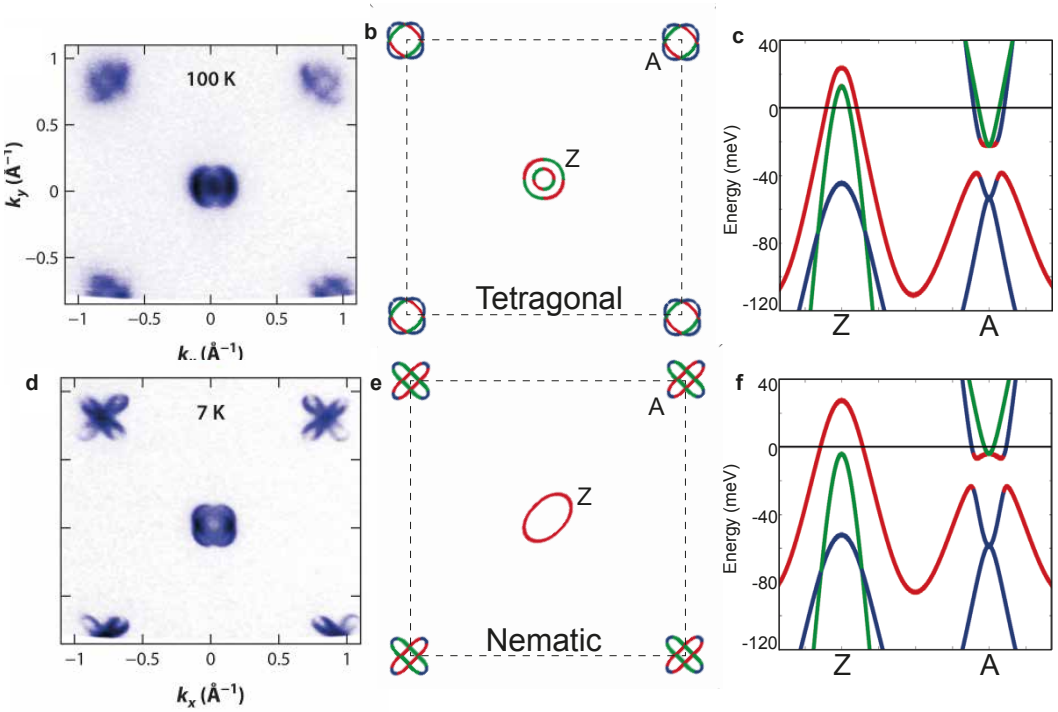

Figure 4.5: Summary of the ARPES-based tight binding model of FeSe. a) Experimental Fermi surface in the tetragonal phase of FeSe at 100 K. b) Calculated Fermi surface of FeSe in the tetragonal phase at $k_z = \pi$. c) Calculated band dispersions along the Z-A direction for the tetragonal phase. d) Experimental Fermi surface of a twinned crystal of FeSe within the nematic phase at 7 K. e) Calculated Fermi surface including the 29 meV experimental nematic order parameter. f) Calculated band dispersion for the nematic model of FeSe. Here the colour describes the maximum orbital content of the band, green = d_{yz}, red = d_{xz} and blue = d_{xy}.

now have a model which can quantitatively describe the low temperature electronic structure as described by ARPES experiments on twinned crystals of FeSe. This result is concluded in Fig. 4.5.

4.4 ARPES studies on detwinned crystals of the iron-based superconductors

4.4.1 Detwinning orthorhombic crystals

Domain structures occur to lower the total energy of a macroscopic system. In a ferromagnet, a single domain holds a large amount of magnetostatic energy, the stress of which can be greatly relieved if the system splits into two smaller domains aligned antiparallel to each other [171]. Equivalently, one single orthorhombic domain will

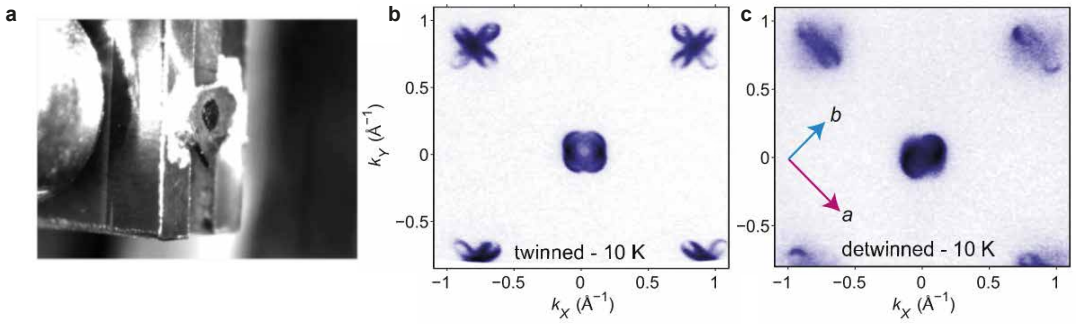

Figure 4.6: Comparison of a twinned and detwinned Fermi surface of FeSe. a) Photograph of the uniaxial strain device with attached sample. b) Fermi surface of a twinned crystal of FeSe at 10 K. c) Fermi surface of a detwinned crystal FeSe at 10 K, here strain has been applied along the *a*-crystallographic axis. Figures adapted from Ref. [163].

exhibit a large amount of strain on the macroscopic crystal, which can be alleviated by forming two smaller 90° rotated domains.

In FeSe, these domains are considerably smaller than a conventional photon beam used in ARPES. the corresponding photoemission data that is measured will be a superposition of both rotated domain structures. This is clearly seen in Fig. 4.2(c), where two 90° rotated ellipses are observed at the centre of the Brillouin zone at 7 K. The determination of the nematic order parameter has, so far, been entirely based around inferring the true electronic structure of nematic FeSe from this twinned data. However, it would be informative to confirm if this interpretation is also correct in a mono-domain sample.

It is possible to greatly reduce the population of one of the orthorhombic domains by introducing uniaxial strain [172]. Effectively, the orthorhombic domains will tend to align along the axis of strain. This provides a method to significantly reduce the population of the 90° rotated electronic structure measured in photoemission experiments and study the contribution of the electronic structure of FeSe without twinning effects. To confirm the validity of the nematic order parameter, I will now study the experimental ARPES data of detwinned crystals of FeSe [163].

4.4.2 Uniaxial strain device

Fig. 4.6(a) presents a photograph of the uniaxial strain device employed to study detwinned crystals. The strain is applied mechanically, the device consists of two pillars separated by a small distance, with the corners of the crystal glued to each crystal.

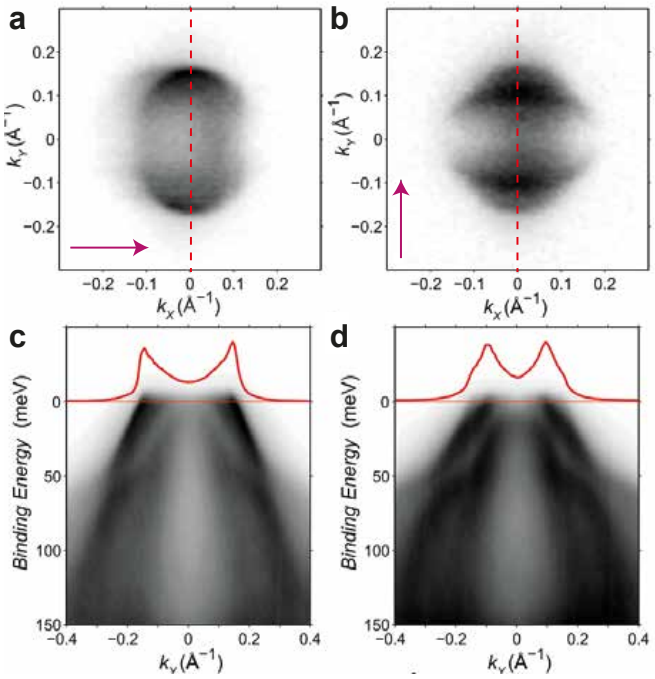

Figure 4.7: Fermi surface and band dispersions of detwinned crystals of FeSe at the hole pocket using a photon energy of 23 eV and LH polarisation. a) Fermi surface measured with the strain parallel to the k_x axis. b) Fermi surface measured with the sample rotated 90° degrees, corresponding to the second orthorhombic orientation. c,d) Band dispersions corresponding to the cuts taken along the dashed red lines in (a,b). The MDC's integrated around the Fermi level are also presented. Figure adapted from Ref. [163].

Whilst most of the strain on the sample occurs via thermal contraction of the device, additional strain can be applied via the screw if the degree of detwinning does not look sufficient. The Fermi surface of FeSe measured on an unstrained crystal, and a strained crystal are presented in Fig. 4.6(b) and Fig. 4.6(c). This shows the effect of detwinning the crystal via uniaxial strain.

4.4.3 ARPES study of detwinned crystals of FeSe

Hole pocket

In Fig. 4.7, the band dispersion and Fermi surface located around the centre of the Brillouin zone, are presented. This data was taken at 23 eV, corresponding to the Z point, using LH polarised light. In Fig. 4.7(a), a single elliptical hole pocket can be observed, which indicates that the sample has been successfully detwinned. In Fig. 4.7(b), the Fermi surface measured at the same location on the sample after rotating

the sample 90° is presented. This corresponds to the spectral weight arising from the second orthorhombic orientation. Here, the majority of the spectral weight has shifted to be aligned along the k_x axis. This confirms that the second orthorhombic orientation is being measured. It can seen in Fig. 4.7(b), that this sample is not 100% detwinned and that some spectral weight from the elliptical hole pocket of the minority domain can still be detected. This can also be seen in the cuts presented in Fig. 4.7(c) and 4.7(d), where two hole bands can be observed crossing the Fermi level. In Fig. 4.7(c) a majority of the spectral weight is present on the outer band, corresponding to one domain, whilst the spectral weight in Fig. 4.7(d) is localised on the inner band from the other domain. This is most clearly seen in the MDC's taken at the Fermi level.

By comparing the relative ratios of the intensity of the outer and inner bands from both domains, it is possible to extract the degree of detwinning of the sample. In the sample studied here it was determined that this population of the domain along the axis of strain was 80% of the total spectral weight. However, a 20% contribution from the second domain is still present [163].

The observation of only one hole pocket in detwinned crystals of FeSe agrees with the assumptions made on twinned crystals of FeSe, and agrees with the tight binding model described in Fig. 4.5(e,f).

The electron pocket

In Fig. 4.8, ARPES measurements of the electron pocket at 56 eV, corresponding to the A point, are presented using LV polarised light. In a single domain, one electron pocket can be observed at the Fermi surface, as shown in Fig. 4.8(a). The band dispersion, taken though the centre of the A point, along the k_y axis, is presented in Fig. 4.8(d). This also confirms that only one electron band can be observed. This electron band is very shallow, with a minima less than -5 meV below the Fermi level. Apart from the shallow electron band only the broad d_{xy} state at -50 meV can be observed.

In Fig 4.8(b), the Fermi surface from the second orthorhombic orientation is presented. Again, only one electron pocket can be observed. However, by taking a cut along k_y, in Fig 4.8(e), a deeper electron band of dxy orbital character can be observed. There is also a hole-like band, with a maximum binding energy which is equivalent to the electron-band minima in Fig. 4.8(d). This corresponds to a saddle point at the high symmetry axis, where the band rotates by 90°.

This information does not agree with the tight binding model, presented in Fig. 4.5(e,f), where two electron pockets are expected to be present at the Fermi level, and

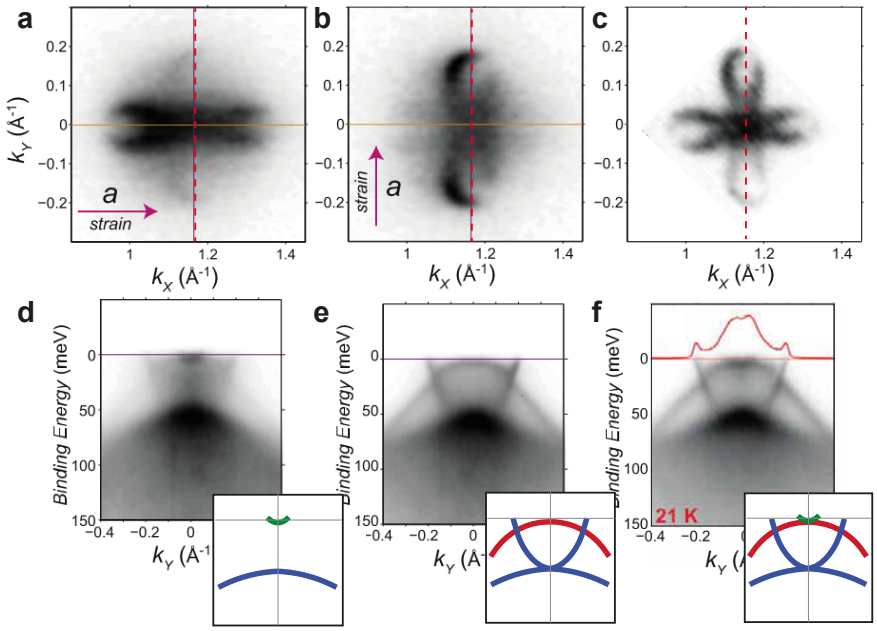

Figure 4.8: Fermi surface and band dispersions of detwinned crystals of FeSe at the electron pocket using a photon energy of 56 eV and LV polarisation. a) Fermi surface of the A point with the strain parallel to the k_x axis. b) Equivalent Fermi surface measured after the sample is rotated 90° corresponding to the second domain. c) Twinned Fermi surface of the A point for comparison, showing both electron pockets. d-f) Band dispersions of (a-c) taken along the dashed red lines. A cartoon of the band dispersion for each image is shown in the bottom right hand corner. Here the colour describes the maximum orbital content of the band, green = d_{yz}, d_{xz} and blue = d_{xy}. Figure adapted from Ref. [163].

the band dispersions were expected to exhibit C_4 rotational symmetry. Moreover, a Fermi surface consisting of only a single electron pocket is inconsistent with any form of nematic ordering which only shifts or splits the band dispersions from the tetragonal state [163]. In the tetragonal state, at 100 K, two electron pockets are detected in ARPES studies [100, 102]. If a band shift or splitting occurred to remove one of the electron pockets from the Fermi level, this would have been observed within ARPES data on twinned crystals. Instead, two bands which were present in the tetragonal state, are simply no longer observed at temperatures below the nematic transition. Potentially, this could originate from a Fermi surface reconstruction, or a momentum and orbital dependent incoherence. However, the origin of this will require further study.

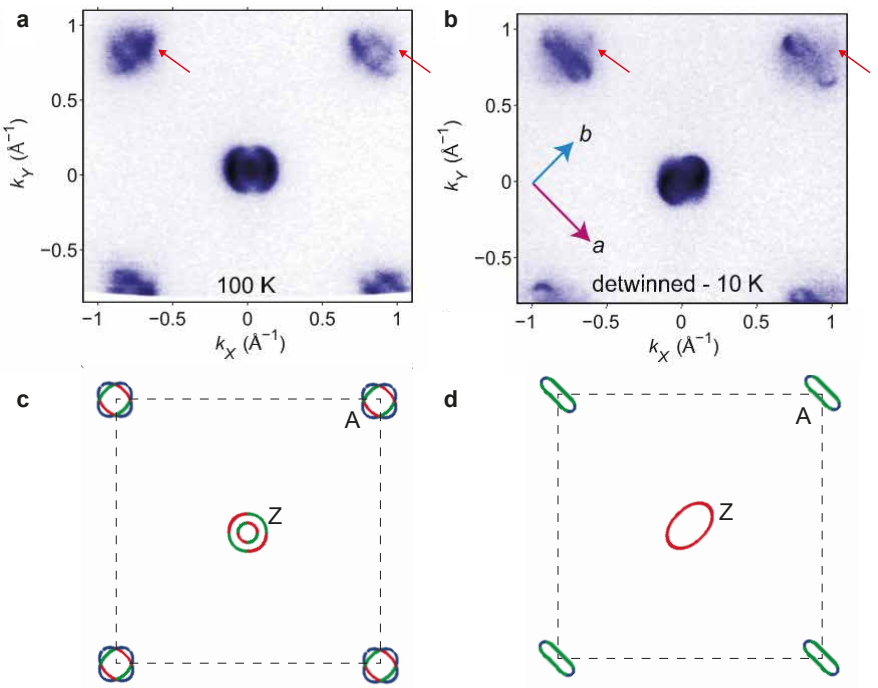

Figure 4.9: Summary of the Fermi surface of FeSe. a) In the tetragonal phase, where two electron pockets are observed. b) In the nematic phase where only one electron pocket is measured. The red arrows point to the position where the second electron pocket is predicted to be by theoretical models. c,d) Calculated Fermi surface of FeSe from the optimised tight binding model corresponding to (a) and (b).

4.4.4 *Developing a "one electron pocket" model of FeSe*

The data that has been obtained on detwinned crystals of FeSe suggests that the Fermi surface consists of one elliptical hole pocket and one peanut shaped electron pocket.

Currently, the experimental tight binding model describes a system of FeSe with one elliptical hole pocket and two peanut shaped electron pockets. A method to remove the bands not detected within ARPES experiments must therefore be defined. This is challenging for several reasons; the first reason is that the fundamental symmetry of the *Cmma* crystal structure of orthorhombic FeSe implies that two electron pockets must be present. The bands at the high symmetry M/A point consist of saddle points, rather than maxima and minima. A shift to the binding energy of the saddle point, either above or below the Fermi level, would not lower the number of bands crossing the Fermi level. The second reason, is that the limits of the changes to the electronic structure are not explicitly known. It is not known if the bands predicted to exist in tight binding descriptions, are incoherent down to a specified energy or if there is a momentum dependence to this incoherence. It is also a possibility that some unknown

reconstruction of the Fermi surface has occurred to remove the bands entirely.

From the data discussed in Fig. 4.8 it is possible to claim that the d_{xz} hole-like band in the k_x direction around the M point is not present down to below -50 meV and within the momenta of ± 0.4 Å^{-1} around the M point in the k_x direction. The same conclusion is obtained with the d_{xy} electron band that is predicted to cross the Fermi level.

If the states within this energy and momentum range are ignored, then it is possible to reproduce a tight binding description of FeSe that describes the experimental measurement. However, this limits the tight binding model to properties that only depend on binding energies in the region of 0 to -50 meV. Caution must therefore be applied when applying this model to higher binding energies.

A comparison between the experimental and modelled Fermi surface of FeSe, in both the tetragonal and nematic state, is presented in Fig. 4.9. Fig. 4.9(a) shows the experimental Fermi surface of the tetragonal state of FeSe at 100 K. This consists of two overlapping elliptical electron pockets at the corner of the Brillouin zone (A point), and two spherical hole pockets at the centre (Z point). This is directly reproduced from the tight binding model, derived in Chapter 3. The Fermi surface of the tetragonal ARPES-based model is shown in Fig. 4.9(c). In Fig.4.9(b) the Fermi surface measured at 10 K in a detwinned crystal of FeSe is shown. This consists of only one elliptical hole pocket and one peanut shaped electron pocket. In Fig. 4.9(d), the Fermi surface described by the updated tight binding model is presented. This includes the 29 meV nematic order parameter, described in Sec. 4.4.2. It also neglects the bands that are not observed in detwinned ARPES. This then correctly reproduces the shape of the Fermi surface and the binding energy of the bands as seen in ARPES experiments [102, 165].

Here, I would like to stress that the physical origin for this description of the electronic structure of FeSe is unknown. However, as I will discuss in the following chapters, this experimental phenomenology will have dramatic consequences on the experimental properties of FeSe.

4.4.5 ARPES studies of detwinned crystals of NaFeAs

The experimental observation of only one electron pocket at the Fermi level of FeSe had not been suggested prior to the experiment of Watson. et. al. [163]. However, it is natural to now ask whether this “one electron pocket" description is a generic feature of the nematic phase, or specifically linked to FeSe.

To provide some insight to this question ARPES measurements were performed on

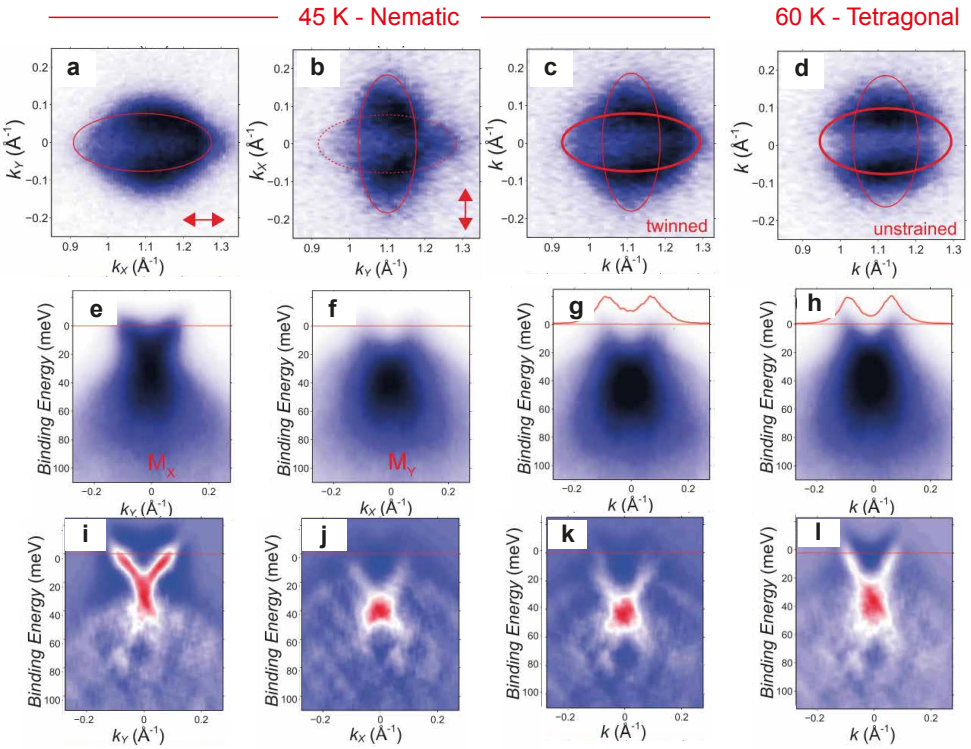

Figure 4.10: ARPES data of the electron pocket of detwinned crystals of NaFeAs in the nematic phase at 45 K and tetragonal phase at 60 K. a) The Fermi surface of a single domain with strain pointing along the k_x axis. b) The Fermi surface of the second domain with strain point along the k_y axis. c) Fermi surface of a twinned orthorhombic sample. d) Fermi surface of a sample in the tetragonal phase. e-h) Cuts along the k_y axis corresponding to the Fermi surface of a-d). i-l) Second derivative images of (e-h) highlighting the differences between the orthorhombic domains.

a detwinned crystal of NaFeAs[1]. NaFeAs, has the same $P4/nmm$ crystal structure as FeSe and exhibits a nematic transition at the lower temperature of $T_s = 54$ K. A striped antiferromagnetic phase also occurs below $T_N = 43$ K [174]. There is therefore an 11 K window where nematicity is finite, but magnetic ordering has not stabilised. In Fig. 4.10, Fermi surface maps and band dispersions of the electron pocket of NaFeAs, within the nematic-only window at 45 K, are presented. The nematic ordering is less pronounced here than in FeSe, only 9 K below T_s, however, a marked anisotropy between the single domain of Fig. 4.10 (a,e,i) and the 90 degree rotated domain of Fig. 4.10 (b,f,j) can be observed. This indicates that a majority of the spectral weight is from only one electron pocket, analogous to the effect seen in Fig. 4.8 for FeSe.

[1]Unlike the previous discussion on detwinned crystals of FeSe, I personally contributed to the experimental results presented here [173].

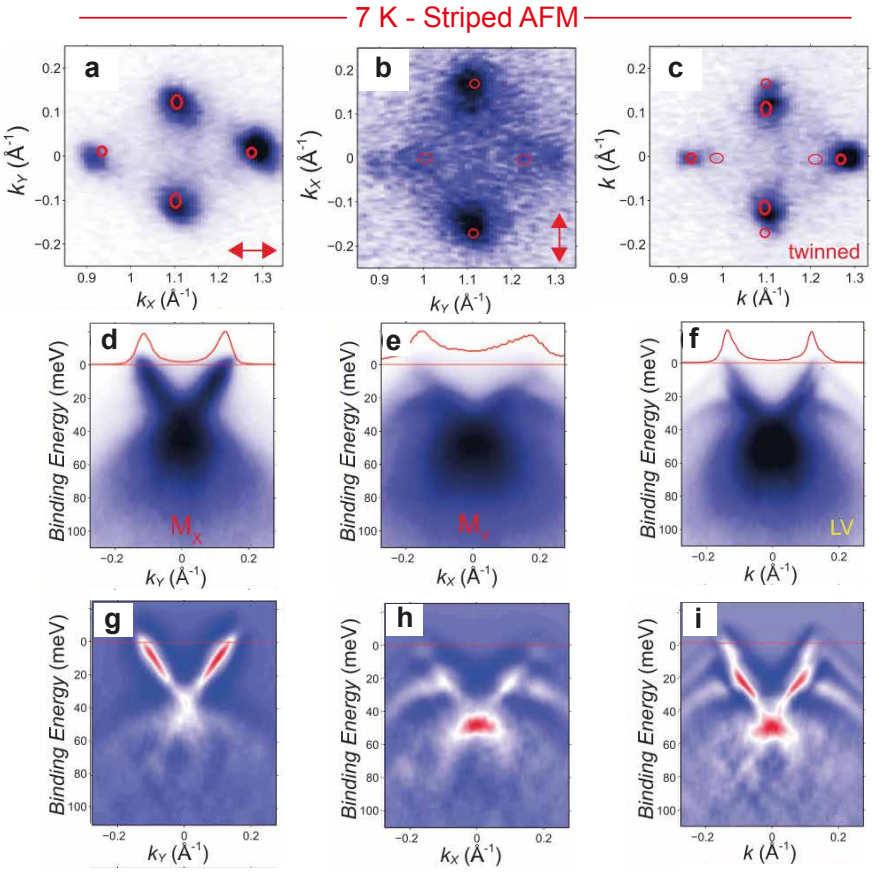

Figure 4.11: ARPES data of the electron pocket of detwinned crystals of NaFeAs in the antiferromagnetic phase at 10 K. a) Fermi surface of a single domain with strain pointing along the k_x axis. b) Fermi surface for the second domain with strain point along the k_y axis. c) Fermi surface of a twinned orthorhombic sample. d-f) Cuts along the k_y axis corresponding to the Fermi surface of a-c). g-i) Second derivative images of d-f) highlighting the differences between the orthorhombic domains.

On entering the antiferromagnetic phase, the unit cell of the NaFeAs doubles to include the newly stabilised up and down spin configuration. As a consequence, the momentum space Brillouin zone halves in size. The electron pockets fold onto of the hole pockets, and hybridise [173]. This hybridisation leads to an entirely reconstructed Fermi surface, shown in Fig. 4.11. Despite the added complication, the anisotropy between the two domains (Fig. 4.11 (a,d,g) and Fig. 4.11 (b,e,h)) still remains. This indicates that only the single electron pocket, observed in the nematic phase of Fig. 4.10 is present in the hybridisation.

This result provides evidence to suggest that a Fermi surface composed of only one electron pocket might be a generic feature of the nematic phase. However, this

experiment must be repeated with more materials to confirm this hypothesis.

4.5 Discussion

The observation of only one electron pocket at the Fermi surface of the nematic phase of FeSe and NaFeAs is unconventional and unexpected. Currently, no theory of the nematic phase suggests such a dramatic anisotropy of the band structure, nor does the symmetry of the Fermi surface agree with ab-initio calculations or tight binding models of a *Cmma* crystal structure [145].

Considering that two electron pockets are observed in the tetragonal phase of FeSe, it is natural to assume that two electron pockets should also be observed at temperatures below the structural transition. The exact band positions may have potentially shifted or split from the tetragonal values, but all bands should be present in some capacity. However, no band shift, splitting or nematic order parameter can account for this observed anisotropy. If an electron band simply rose above the Fermi level at the M point, a new hole pocket would appear, due to the nature of the saddle point at this momenta. Instead the states associated with one of the electron pockets are simply not observed.

This phenomenon was completely masked from conventional ARPES studies on twinned crystals due to the apparent C_4 symmetry of the electron pockets. This now leaves the interpretation of a nematic order parameter more ambiguous. In Fig. 4.3, certain nematic order parameters were ruled out on the basis that they did not agree with the symmetry of the electron pocket. Whilst ferro-orbital ordering (Fig. 4.3(b)) still does agree with the detwinned ARPES data, it is now not possible to rule out some combination of extended s-wave bond ordering (Fig. 4.3(d)) and d-wave bond ordering (Fig. 4.3(c)), assuming that the d_{xy} and d_{xz} bands do not contribute to the electron pocket below the nematic transition. This is not equivalent to an orbital dependent incoherence, however, as both d_{xz} weight and d_{xy} weight can still be detected at other momenta within the Brillouin zone [95].

There is additional evidence in favour of a one hole pocket and one electron pocket Fermi surface within the nematic state of FeSe. Hardy *et. al.* [175] has presented measurements of the Sommerfeld coefficient of FeSe from specific heat experiments. Quantum oscillation experiments on 2D materials are able to extract the effective mass of quasiparticle bands at the Fermi surface [176, 177], which can be used to calculate the Sommerfeld coefficient. Hardy *et. al.* showed that the Sommerfeld coefficient

measured from specific heat studies of FeSe could accurately be reproduced from the effective masses obtained from quantum oscillation studies. However, it could only be reproduced when a Fermi surface consisting of one hole pocket and one electron pocket was assumed.

The amount of uniaxial strain applied to the sample depends on the thermal contraction of the strain device [102]. Thus a temperature dependence of the electron bands, as performed on twinned samples in Fig. 4.1, is not possible as it would alter the amount strain applied to the crystal, making our results unsystematic. A peizostack based device, compatible with ARPES, may be able to rectify this issue [178]. Alternative methods may be required to probe the disappearance of the electron pocket as a function of nematic ordering.

It is unlikely that the non-observation of the theoretically predicted second electron pocket is induced by the application of uniaxial strain. No other differences between the electronic structure of a twinned crystal and a detwinned crystal are observed. Moreover, the amount of strain applied should not cause any external change to the band structure until most of the domains have been aligned along the axis of strain [179]. The sample studied in this chapter was only 80% detwinned [163]. To confirm that strain is not important, it is necessary to use alternate experimental probes which can resolve the momentum dependent electronic structure of a single domain of an iron-based superconductors. This will be addressed in the next chapter.

Finally, whilst the lack of observation of the second electron pocket was unexpected, this phenomena could be the key signature of the nematic phase. The loss of an electron pocket is likely to induce large anisotropic effects in experimental observables such as conductivity, resistivity, and magnetism, which all depend on available scattering channels at the Fermi level [72]. If this is the case, it calls for theoretical efforts to develop a microscopic model which can account for the loss of the specific bands within the nematic state, and consequently the lack of observation of a second electron pocket. This may provide the insight required to understand nematicity, and potentially superconductivity in the iron-based superconductors.

4.6 Conclusion

In this chapter I have studied in detail the consequences of nematicity on the electronic structure of FeSe. I have determined that a 30 meV nematic order parameter is required to describe the shift to the bands observed in ARPES studies on twinned crystals. I then

determined a nematic order parameter which could quantitatively describe the change to the electronic structure.

By studying the data of detwinned crystals of FeSe, it was concluded that two bands, which were present in the tetragonal state, can no longer be detected in the nematic state. As a consequence the theoretically predicted electron pocket pointing along the *b* crystallographic axis is not present at the Fermi surface. This phenomenon was also observed in detwinned crystals of NaFeAs, suggesting that a one electron pocket Fermi surface may be a generic signature of the nematic phase of the iron-based superconductors.

This anisotropy, whist unconventional, may be able to explain many of the experimentally observed anisotropic responses of FeSe, and other iron-based superconductors. As I will show in the Chapter 6, this loss of the second electron pocket will have consequences on the superconducting state.

5 | Calculation of the Quasiparticle Interference spectrum of the nematic state of FeSe

5.1 Introduction

In Chapter 4, we studied the electronic structure of the nematic state of FeSe using ARPES. It was noted, that two bands, which were present in the tetragonal state, were no longer detected below 90 K. As a consequence of this, the Fermi surface of the nematic state was observed to consist of one hole pocket and one electron pocket. This measurement, however, disagreed with ab-initio calculations [145] and the generic symmetry arguments of tight binding models for the *Cmma* lattice [142, 146], where one hole pocket and two electron pockets are suggested to be present.

Until this discovery of a “one electron pocket" Fermi surface in FeSe [163], it was always assumed that two electron pockets would contribute to the Fermi surface within the nematic state. In fact, to date, all theoretical calculation of the nematic state of FeSe has been performed on a model which is composed of two individual electron pockets [78, 94, 146, 170, 180–183]. For theoretical calculations which are sensitive to the Fermi surface topology, such as calculations involving the superconducting gap [89], a “one electron pocket" model of the electronic structure would provide a dramatically different description of physical observables, compared to the conventional “two electron pocket" model [95]. It is therefore crucial to study the experimental electronic structure of FeSe in more detail, in order to distinguish between the the apparent contradiction between ARPES data on detwinned crystals [163] and previous theoretical assumptions.

For this reason we turn our attention to the technique of Quasiparticle Interference (QPI). QPI is a scanning tunnelling spectroscopy (STS) based technique, which probes

the local density of states on the individual atom scale. By measuring the density of states as a function of position, (r_x, r_y), centred around a scattering site, it is possible to extract information about the scattering vectors, $\mathbf{q} = \mathbf{k} - \mathbf{k}'$, associated with a material.

This experiment therefore is an independent yet complimentary technique to ARPES, which is not limited by photoemission-based selection rules. Moreover, the atomic-level precision of STS based experiments allows QPI to probe the electronic structure of FeSe within a single orthorhombic domain. This overcomes one of the limitations of ARPES, where there data collected on orthorhombic crystals is a superposition of two 90° rotated lattices.

In this chapter, I will calculate the scattering vectors that are measured by QPI experiments. By comparing the calculated dispersions suggested by the experimentally determined “one electron pocket" model of FeSe with a conventional “two electron pocket" model, I will be able to determine whether QPI experiments support or contradict the unusual conclusion obtained from ARPES studies on detwinned crystals. I will also address the issue of finite k_z states within measurements of QPI. Whilst most theoretical calculations describing QPI assume a 2D, $k_z = 0$, model for the electronic structure, I find that $k_z = \pi$ states also need to be accounted for to describe the experimental QPI measurements of FeSe.

5.2 Methodology

5.2.1 STM

Scanning tunnelling microscopy (STM) utilises the quantum mechanical effect of tunnelling. By bringing two metallic objects a small but finite distance apart, electrons from the surface can transfer between the two. In STM, one metallic object is the material of interest, whilst the other is an (almost) atomically sharp tip of a conductive material. By inducing a bias voltage into the tip, a current can be induced between the two objects. The measured current can then be related to the density of states of the material at the surface.

Assuming a spherical s-wave tip, and Bardeen’s theory of tunnelling [184], it is possible to equate the tunnelling current, $I(V, \mathbf{r})$, to the density of states at the sample,

$$I(V, \mathbf{r}) = \frac{4\pi e}{\hbar} e^{-s\sqrt{\frac{8m\phi}{\hbar^2}}} n_t(0) \int_{-eV}^{0} n_s(\varepsilon, \mathbf{r}) d\varepsilon. \tag{5.1}$$

Here, $n_t(0)$ is the density of states for the tip (which is assumed to be independent

of the bias voltage, V) and $n_s(\varepsilon, \mathbf{r})$ is the density of states of the sample at a given energy and position. The exponential depends on the distance between the sample and tip, s, and the work function of the sample, ϕ.

The derivative of Eq. (5.1), with respect to energy, provides a direct measure of the density of states of the sample,

$$\frac{dI(V,\mathbf{r})}{d(-eV)} = -\frac{4\pi e}{\hbar} e^{-s\sqrt{\frac{8m\phi}{\hbar^2}}} n_t(0) n_s(-eV,\mathbf{r}). \tag{5.2}$$

It is important to keep the sample to tip distance (s) constant. Not only does this ensure that the tip does not collide with the surface, but, as the current is exponentially sensitive to s, it also ensures that the measured current is directly proportional to the density of states. To achieve a constant value for s, STM measurements are typically performed with a feedback mechanism. This adjusts the z position of the tip such that the current is held constant. This chosen current is locked in by applying an initial bias voltage, V_0, such that,

$$I_0(V,\mathbf{r}) = \frac{4\pi e}{\hbar} e^{-s\sqrt{\frac{8m\phi}{\hbar^2}}} n_t(0) \int_{-eV_0}^{0} n_s(\varepsilon,\mathbf{r}) d\varepsilon. \tag{5.3}$$

This can then be fed into a feedback loop which allows the position of the tip to be adjusted to ensure a constant current at a given bias voltage.

By combining equation (5.1) and (5.3), the measured current is now independent of the prefactors associated with the density of states,

$$I(V,\mathbf{r}) = I_0 \frac{\int_{-eV}^{0} n_s(\varepsilon,\mathbf{r}) d\varepsilon}{\int_{-eV_0}^{0} n_s(\varepsilon,\mathbf{r}) d\varepsilon}. \tag{5.4}$$

The derivative of Eq. (5.4) then gives,

$$g(V,\mathbf{r}) = \frac{dI(V,\mathbf{r})}{dV} = I_0 \frac{-e n_s(-eV,\mathbf{r})}{\int_{-eV_0}^{0} n_s(\varepsilon,\mathbf{r}) d\varepsilon}. \tag{5.5}$$

By applying an additional voltage V, and measuring the current, It is possible to obtain a direct measure of the density of states, $g(V,\mathbf{r})$. Eq. (5.5) is a standard quantity that can be measured by experimental equipment. However, as the denominator of this equation has a complicated dependence on the density of states, which can be influenced by the choice of V_0, if one is not careful it is possible to obtain qualitatively different results for $g(V,\mathbf{r})$, depending on the initial bias voltage [185]. There are several methods used to overcome this issue, for the case of the experimental work of

FeSe [158, 159] the Feenstra function has been used. The Feenstra function, $L(V,\mathbf{r})$, is defined as,

$$L(V,\mathbf{r}) = \frac{\frac{dI}{dV}}{I/V} = V\frac{-en_s(-eV,\mathbf{r})}{\int_{-eV}^{0} n_s(\varepsilon,\mathbf{r})d\varepsilon}. \tag{5.6}$$

Eq. (5.6) is the result of dividing Eq. (5.5) by Eq. (5.4). This is now independent of the initial bias voltage, V_0, and thus will in theory produce the same result regardless of experimental setup. This is the function that I will calculate in this chapter.

5.2.2 Local density of states in the presence of a point like defect

In order to model the momentum resolved local density of states (LDOS), measured by experiment, we must describe a system with a local perturbation which gives rises to spatial modulations in the density of states. These perturbations can arise from the presence of impurities and can be calculated by using a T-Matrix formalism.

In this section, I will derive the equation for the LDOS of a system with a single impurity. It is assumed that the impurity produces a scalar scattering potential, $\hat{V}$, and is located at a single site, $\mathbf{r}_\alpha$, which can be modelled by a point-like delta function. The Hamiltonian of this system is defined,

$$\hat{H}(\mathbf{r}) = \hat{H}^0(\mathbf{r}) + \hat{V}\delta(\mathbf{r}_\alpha). \tag{5.7}$$

Here, $\hat{H}^0(\mathbf{r})$ describes the initial Hamiltonian of the system and $\hat{V}\delta(\mathbf{r}_\alpha)$ describes the localised impurity.

Green's Function

The retarded Green's function, $\hat{G^R}(\mathbf{r},\mathbf{r}',\omega)$, for the Hamiltonian described in Eq. (5.7) can be written in the form of a Dyson equation,

$$\hat{G^R}(\mathbf{r},\mathbf{r}',\omega) = G^0(\mathbf{r}-\mathbf{r}',\omega) + G^0(\mathbf{r}-\mathbf{r}_\alpha,\omega)\hat{V}G^R(\mathbf{r}_\alpha,\mathbf{r}',\omega). \tag{5.8}$$

This equation relates the real space, non-interacting Green's function, which only depends on the difference of the co-ordinates $\mathbf{r}$ and $\mathbf{r}'$, to the interacting system. $\hat{G^R}(\mathbf{r},\mathbf{r}',\omega)$ can then be expanded into an infinite series,

$$\begin{aligned}\hat{G^R}(\mathbf{r},\mathbf{r}',\omega) = & G^0(\mathbf{r}-\mathbf{r}',\omega) \\ & + G^0(\mathbf{r},\omega)\hat{V}G^0(-\mathbf{r}',\omega) \\ & + G^0(\mathbf{r},\omega)\hat{V}G^0(0,\omega)\hat{V}G^0(-\mathbf{r}',\omega) \\ & + G^0(\mathbf{r},\omega)\hat{V}G^0(0,\omega)\hat{V}G^0(0,\omega)\hat{V}G^0(-\mathbf{r}',\omega) \\ & + ...\end{aligned} \tag{5.9}$$

Here, $\mathbf{r}_\alpha = 0$ has been set to zero for simplicity. This infinite series can be written in the compact form,

$$\hat{G^R}(\mathbf{r},\mathbf{r}',\omega) = G^0(\mathbf{r}-\mathbf{r}',\omega) + G^0(\mathbf{r},\omega)T(\omega)G^0(-\mathbf{r}',\omega). \tag{5.10}$$

The T-matrix, $T(\omega)$, is defined

$$T(\omega) = \hat{V}[1 + G^0(0,\omega)\hat{V} + (G^0(0,\omega)\hat{V})^2 + (G^0(0,\omega)\hat{V})^3 + ...]. \tag{5.11}$$

This is then equivalent to,

$$T(\omega) = \frac{\hat{V}}{\hat{1} - \hat{V}G^0(\mathbf{r}=0,\omega)} = \frac{\hat{V}}{\hat{1} - \hat{V}\sum_{\mathbf{k}} G^0(\mathbf{k},\omega)}. \tag{5.12}$$

Moreover, the Fourier transform relationship, $G^0(\mathbf{r}=0,\omega) = \sum_{\mathbf{k}} G^0(\mathbf{k},\omega)$, makes it possible to calculate this T-matrix in momentum space. The Fourier transform of the retarded Green's function from Eq. (5.10) is then

$$\hat{G^R}(\mathbf{k},\mathbf{k}',\omega) = G^0(\mathbf{k},\omega) + G^0(\mathbf{k},\omega)T(\omega)G^0(\mathbf{k}',\omega). \tag{5.13}$$

Finally, the non-interacting Green's function in momentum space is defined as,

$$G^0(\mathbf{k},\omega) = \frac{1}{(\omega + i\delta^+) - H^0(\mathbf{k})}. \tag{5.14}$$

LDOS

The LDOS is defined as

$$N(\mathbf{q},\omega) = -\frac{1}{2\pi i} Tr\{\sum_{\mathbf{k}} G(\mathbf{k},\mathbf{k}-\mathbf{q},\omega) - G^*(\mathbf{k},\mathbf{k}+\mathbf{q},\omega)\}. \tag{5.15}$$

For the special case of a single impurity, within a centrosymmetric crystal, this can be simplified to

$$N(\mathbf{q},\omega) = -\frac{1}{\pi}\mathrm{Tr}\{\mathrm{Im}\sum_{\mathbf{k}} G(\mathbf{k},\mathbf{k}+\mathbf{q},\omega)\}. \tag{5.16}$$

This allows us to write the LDOS for a system as a sum of the non-interacting density of states, $N^0(\omega)$, plus a perturbation term , $\delta N(\mathbf{q},\omega)$, due to the presence of the impurity,

$$N(\mathbf{q},\omega) = N_0(\omega) + \delta N(\mathbf{q},\omega). \tag{5.17}$$

Here, $N_0(\omega)$ and $\delta N(\mathbf{q},\omega)$ are defined as,

$$N_0(\omega) = -\frac{1}{\pi}\mathrm{Tr}\{\mathrm{Im}\sum_{\mathbf{k}} G^0(\mathbf{k},\omega)\} \tag{5.18}$$

$$\delta N(\mathbf{q},\omega) = -\frac{1}{\pi}\mathrm{Tr}\{\mathrm{Im}\sum_{\mathbf{k}} G^0(\mathbf{k},\omega)T(\omega)G^0(\mathbf{k}+\mathbf{q},\omega)\}. \tag{5.19}$$

We can then take the inverse Fourier transform of Eq. (5.17) to obtain the LDOS in real space,

$$N(\mathbf{r},\omega) = \sum_{\mathbf{q}} N(\mathbf{q},\omega)e^{i\mathbf{qr}}. \tag{5.20}$$

Eq. (5.20) is equivalent to $n_s(\varepsilon,\mathbf{r})$ of Eq. (5.1). Therefore, to match the form of the experimental data that is presented in the literature, the Feenstra function (Eq. (5.6)) can be calculated by

$$L(\mathbf{r},\omega) = \frac{N(\mathbf{r},\omega)}{\frac{1}{\omega}\sum_{\omega'=0}^{\omega'=\omega} N(\mathbf{r},\omega')}. \tag{5.21}$$

In the following work, I present the Fourier transform of Eq. (5.21), $L(\mathbf{q},\omega)$, to model the QPI experiments of FeSe.

5.2.3 Tight binding model

In this chapter, I will compare two models of the electronic structure of FeSe within the nematic state. The first model is a conventional tight binding model that we developed in Chapter 4, which describes a Fermi surface consisting of one hole pocket and two electron pockets. The Fermi surface of this model is presented in Fig. 5.1(a) and will be referred to as the “2eP" model. The second model describes a Fermi surface with

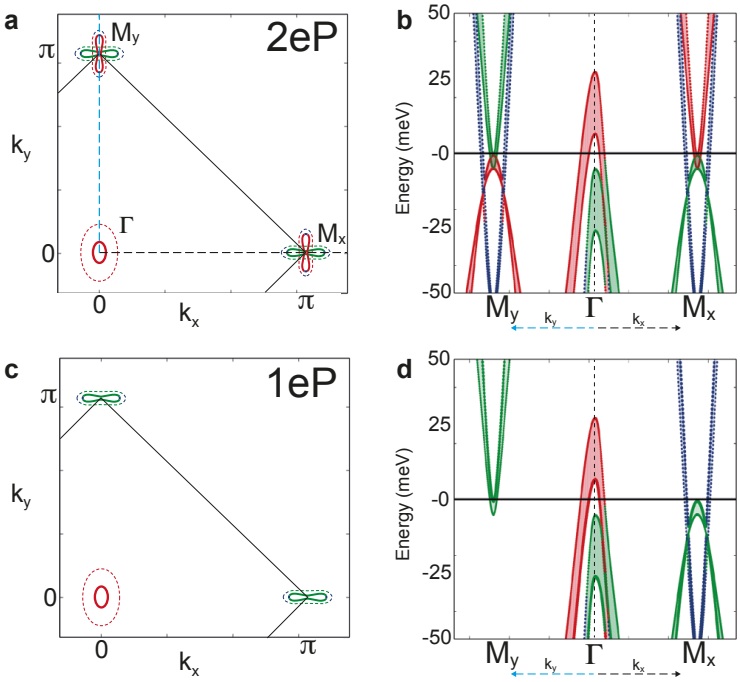

Figure 5.1: Fermi surface and band dispersions for the two tight binding models that will be studied in this chapter. a,b) Fermi surface and band dispersion for the two-electron-pocket (2eP) model of FeSe. solid lines in (a) describe the $k_z = 0$ Fermi surface, dashed lines describe $k_z = \pi$. the shaded region in (b) shows states with finite k_z momenta. c,d) Equivalent calculations for the one-electron-pocket (1eP) model of FeSe. Here, the colours describe the maximum orbital character of the bands: green = d_{yz}, red = d_{xz} and blue = d_{xy}.

one hole pocket and one electron pocket. The Fermi surface of this model is presented in Fig. 5.1(c) and will be referred to as the "1eP" model.

The 2eP model is similar to many tight binding models used within the literature [78, 170, 181, 182]. Whilst there is still some disagreement about the exact theoretical form of the momentum dependence of the nematic order parameter, with some models using a d-wave bond ordering term as described in Fig. 4.3(c) [170, 181], each model of FeSe consists of a Fermi surface with one hole pocket and two electron pockets. The 2eP model in this study includes the nematic order parameter developed in Chapter 4 (Eq. (4.2)), which quantitatively reproduces the ARPES band dispersions for twinned crystals.

Additionally, In this chapter we have reduced the contribution of spin orbit-coupling around the M point, which was slightly overestimated in Chapter 4. The reason for this overestimation is that we are including the bare spin-orbit interaction within a renormalised tight binding model. Thus, it is possible that the in-plane spin orbit interaction

(L_x and L_y) will be different from the out of plane spin orbit interaction (L_z). In order to capture the states between 0 and -25 meV around the M point we therefore modify the in-plane spin orbit coupling strength, such that λ_z remains at 19 meV, whereas $\lambda_{x/y}$ is reduced to 5 meV. Here, λ_i is the prefactor infront of the spin-orbit matrix L_i. This is discussed in Appendix A.

The band structure, at both $k_z = 0$ and $k_z = \pi$, is presented in Fig. 5.1(b). The states around the M_x and M_y points are C_4 symmetric, with the d_{xz} and d_{yz} orbital characters swapping under a 90° rotation. The bands at the M/A point are also highly two-dimensional and exhibit a negligible shift in binding energy between $k_z = 0$ and $k_z = \pi$. In contrast, both the inner and outer hole bands, at the Γ/Z point, increase in binding energy by 20 meV between $k_z = 0$ and $k_z = \pi$. The $k_z = \pi$ hole pocket at the Fermi surface (shown in Fig. 5.1(a) with dashed lines) is also much larger than that the hole pocket at $k_z = 0$ (Fig. 5.1(a) with a solid line).

The Green's function used for this system is defined as

$$G_0(\mathbf{k},\omega) = \frac{1}{(\omega + i\Gamma)\hat{\mathbb{I}} - \hat{H}^0(\mathbf{k})}. \tag{5.22}$$

Here, $\hat{\mathbb{I}}$ is the identity matrix, ω defines the energy, $\mathbf{k}$ is the momentum, $\hat{H}^0(\mathbf{k})$ is the Hamiltonian of the tight binding description and Γ is a broadening parameter which is set to 1.25 meV to model the experimental broadening observed in measurements of FeSe [159].

The bands in the 1eP model have equivalent binding energies to the 2eP model, the only difference is that the d_{xz} band near the M point along both the k_x and k_y axis have been removed. On top of this, the d_{xy} band that is located along the k_y axis near the M point have also been removed. The equivalent d_{xy} band along the k_x axis, however, remains. As a consequence one of the electron pockets, described by the conventional 2eP tight binding model, is no longer present. The band dispersion of the 1eP model is presented in Fig. 5.1(d).

Here, to suppress the bands that are not observed in experiment, the Green's function of the 2eP model is modified with a matrix of orbital weights, $\hat{Z}(\mathbf{k})$,

$$G_0(\mathbf{k},\omega) = \frac{\hat{Z}(\mathbf{k})}{(\omega + i\Gamma)\hat{\mathbb{I}} - \hat{H}^0(\mathbf{k})}. \tag{5.23}$$

Here, the elements of $\hat{Z}(\mathbf{k})$ are defined $\hat{Z}^{ij}(\mathbf{k}) = \sqrt{Z_i(\mathbf{k})}\sqrt{Z_j(\mathbf{k})}$ and the indices describe the d-orbital equivalent to that of the initial Hamiltonian [$1 : d_{xy}, 2 : d_{x^2-y^2}, 3 :$

$d_{xz}, 4 : d_{yz}, 5 : d_{z^2}]$. We introduce a phenomenological momentum dependence to the orbital weights. For each energy, we determine the range of momenta, in k_x and k_y, where the states associated with the bands that are to be suppressed. For momenta within this region, we set $Z_i = [0,1,0,1,1]$, however outside this region $Z_i = [1,1,1,1,1]$. This is a highly phenomenological approach that suppresses a majority of the spectral weight associated with the bands that are not observed in ARPES studies on detwinned crystals. We do not have a microscopic justification for this method of suppression, however, it successfully reproduces the band dispersion observed in ARPES studies on detwinned crystals [163]. For the purpose of this investigation we will therefore use this approach.

It is possible to envisage a reduced 1-Fe unit cell model of FeSe [142], where the two electron pockets are separated in momentum space. However, in the presence of spin orbit coupling, the 1-Fe unit cell is incompatible with k_z states which are not $k_z = 0$ or $k_z = \pi$ [143]. As I will study the effect of k_z on the QPI dispersion, I will retain the physical 2-Fe unit cell of FeSe during this chapter.

The LDOS is calculated on a 512x512 q_x vs q_y grid and the k_x and k_y summation is equivalently performed on a 512x512 grid. For the 3D scenario we assume a model which includes $k_z = 0$ and $k_z = \pi$ states only unless otherwise stated. Finally, the impurity potential V used in the T matrix is set to -100 meV for both models.

5.3 Results

5.3.1 Evidence for $k_z = \pi$ states in the LDOS of FeSe

The effect of k_z on the absolute value of the LDOS, $|N(q_x, q_y, \omega)|$ is presented in Fig. 5.2. In Fig. 5.2(a) we study the 2D scenario for the 2eP model. Here, we only focus on the small scattering vectors which describes intra-pocket scattering. In $\mathbf{q}$-space, scattering associated with the two peanut shaped electron pockets overlap with the elliptical scattering dispersion of the hole pocket. In Fig. 5.2(b), we show the equivalent LDOS for the 2eP model where both $k_z = 0$ and $k_z = \pi$ states contribute. A noticeably different LDOS is calculated, with a marked suppression of the scattering vectors associated with the $k_z = 0$ hole band. This suggests that if k_z does plays a role in the measurements of QPI, it would has a strong influence on the observable scattering dispersion. An equivalent statement can be made about the 1eP model of FeSe. As there is only one electron pocket at the Fermi surface, the overlap of scattering vectors arising from the hole and electron pocket can be clearly observed in the 2D scenario, as shown in Fig. 5.2(c). A large difference between the 2D scenario (Fig. 5.2(c)) and

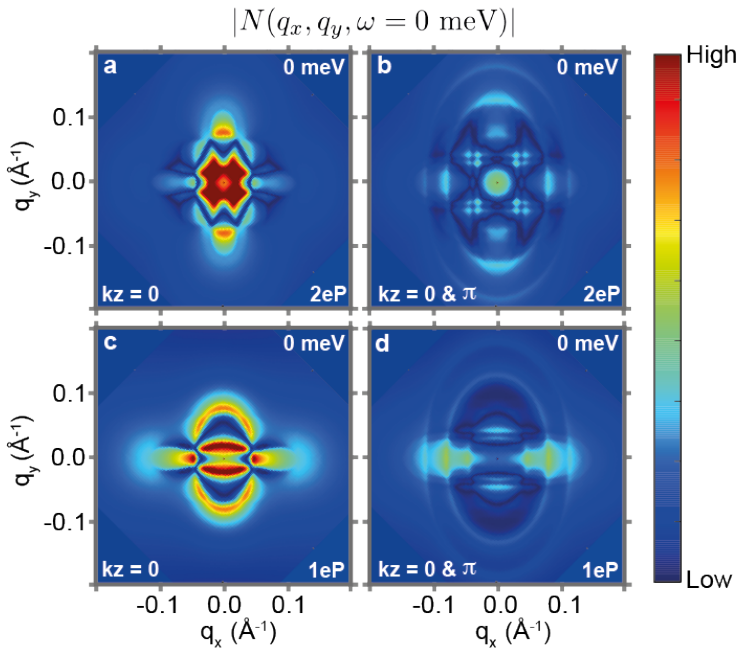

Figure 5.2: Comparison the momentum resolved local density of states $|N(q_x, q_y, \omega = 0 \text{ meV})|$. a) For the 2eP model of FeSe assuming a 2D, $k_z = 0$, electronic structure. b) For the 2eP model of FeSe assuming both $k_z = 0$ and $k_z = \pi$ states contribute to scattering. c,d) Equivalent images for the 1eP model.

the scenario with $k_z = \pi$ states (Fig. 5.2(d)) is also observed. Again, the 3D nature of the hole band weakens the scattering dispersions arising from the $k_z = 0$ hole pocket in Fig. 5.2(c), which is now averaged over both $k_z = 0$ and $k_z = \pi$ states.

To determine whether scattering from $k_z = \pi$ states are present in the experimental QPI data of FeSe, we focus on modelling the Feenstra function of FeSe at $\omega = +25$ meV. At this energy, scattering from the $k_z = 0$ hole state will not be present, as this band has a maxima of only +7 meV [165]. However, the hole band at $k_z = \pi$ extends up to +30 meV, and thus may contribute. In Fig. 5.3, we compare the absolute value of the Feenstra function at $\omega = +25$ meV assuming either a 2D, $k_z = 0$, approximation for the electronic structure, or a scenario with both $k_z = 0$ and $k_z = \pi$ states. In 5.3(a) and (b) we study the 2eP model. For the 2D scenario, only the two C_4 symmetric, electron bands contribute to the scattering dispersion, thus a C_4 symmetric image is calculated. For a scenario including both $k_z = 0$ and $k_z = \pi$ states, the 2eP model consists of the same scattering vectors associated with these two electron states, however, the scattering vectors associated with $k_z = \pi$ hole states are now also predicted to be present. This can be seen as a bright feature highlighted by the yellow arrow in Fig. 5.3(b).

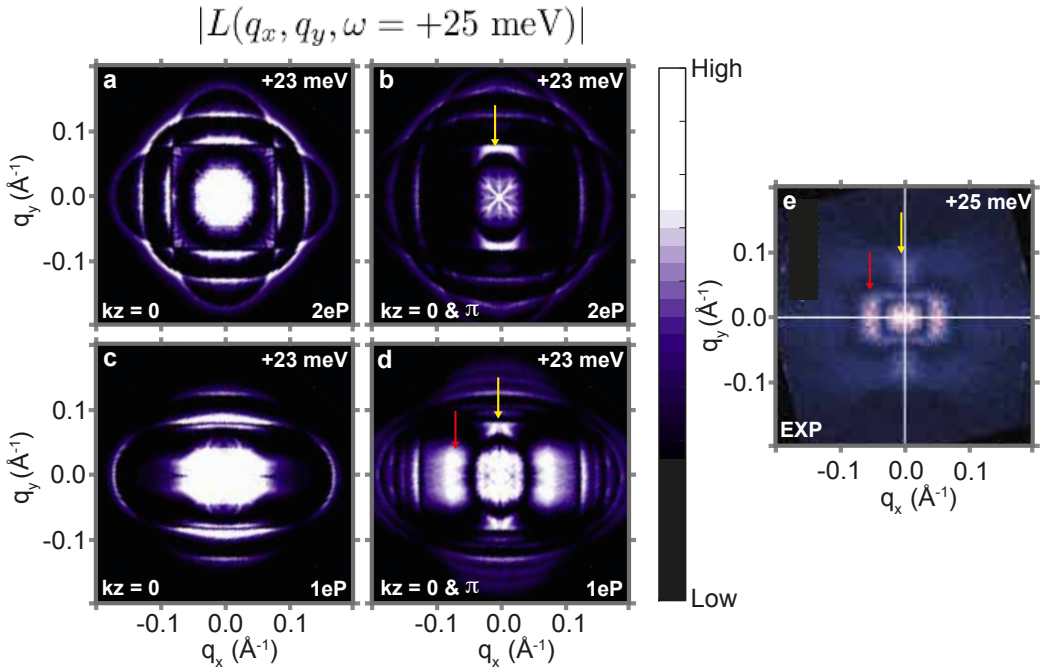

Figure 5.3: Calculated Feenstra function, $|L(q_x, q_y, \omega = +25\ \text{meV})|$. a) For the 2eP model of FeSe assuming a 2D, $k_z = 0$, electronic structure. b) For the 2eP model of FeSe assuming both $k_z = 0$ and $k_z = \pi$ states contribute to scattering. c,d) Equivalent images for the 1eP model. The experimental work of Hanaguri *et. al.* [158] is presented for comparison. The red and yellow arrows highlight agreement between theory and experiment.

For the 1eP model, presented in 5.3(c) and (d), a similar change between the 2D scenario and a scenario which contains both $k_z = 0$ and $k_z = \pi$ states is observed. However, in the 2D scenario, the scattering vectors only occur from a single electron band. For the $k_z = 0$ and $k_z = \pi$ scenario, the 1eP model again shows the appearance of the bright additional feature which is highlighted by the yellow arrow in Fig. 5.3(d) and is associated with the $k_z = \pi$ hole band. At the same time, a more diffuse region of scattering vectors highlighted by the red arrow in Fig. 5.3(d) is also predicted, which is not present in the 2eP model.

In Fig. 5.3(e), we show, for comparison, the experimental Feenstra function measured at $\omega = +25$ meV from the work of Hanaguri *et. al.* [158]. The bright feature (yellow arrow) that is present in both the 2eP model and 1eP model is also observed in the experimental dispersion, albeit weakly. As this feature is present in both the 2eP and 1eP model, we attribute these states to scattering from the hole pocket at $k_z = \pi$. Moreover, the 1eP model also captures the brighter features highlighted by the red arrow in Fig. 5.3(d,e), which is not present in the 2D calculation of Fig. 5.3(c). Thus, the

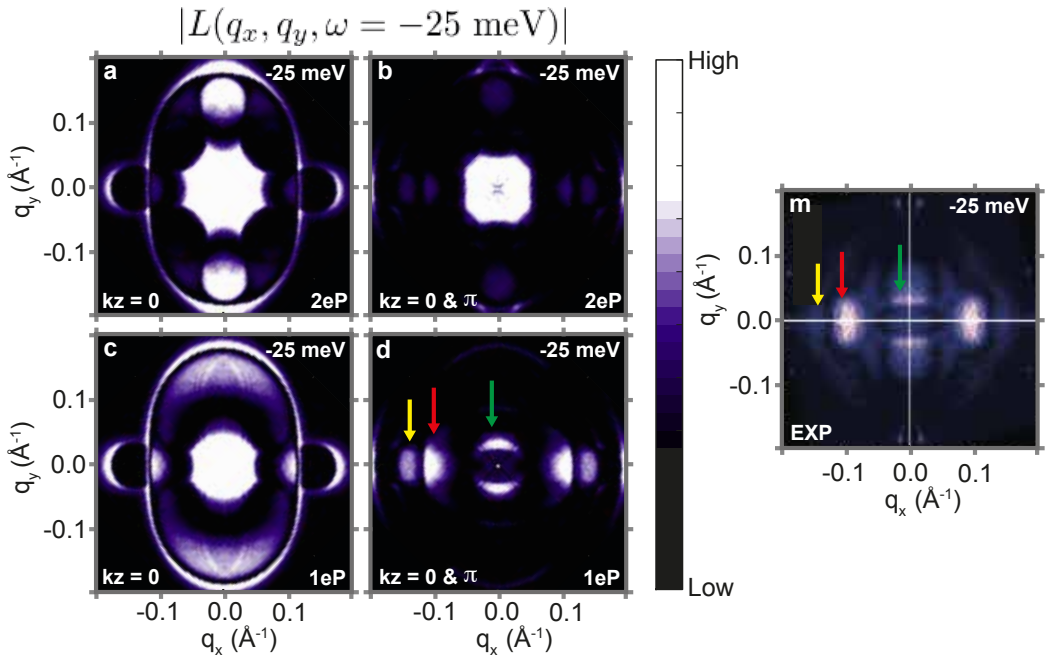

Figure 5.4: Calculated Feenstra function, $|L(q_x, q_y, \omega = -25\ \text{meV})|$. a) For the 2eP model of FeSe assuming a 2D, $k_z = 0$, electronic structure. b) For the 2eP model of FeSe assuming both $k_z = 0$ and $k_z = \pi$ states contribute to scattering. c,d) Equivalent images for the 1eP model. The experimental work of Hanaguri *et. al.* [158] is presented for comparison. The red, yellow and green arrows highlight agreement between theory and experiment.

calculation at $\omega = +25$ meV suggests that $k_z = \pi$ states contribute to the experimental scattering dispersions.

To further support this argument, we next focus on the Feenstra function at $\omega = -25$ meV. Starting again with the 2eP model, in Fig. 5.4(a), the 2D scenario describes scattering from a single elliptical hole pocket, as well as scattering between the small circular like pockets arising from a crossing between a hole band and an electron band around the M point. If we include $k_z = \pi$ states however, as shown in Fig. 5.3(b), the additional 3D hole bands produce a significantly different scattering dispersion where the intensity associated with the $k_z = 0$ hole band and the states around M are much weaker than the small $\mathbf{q}$ scattering vectors.

For the 1eP model, presented in Fig. Fig. 5.4(c,d), The inclusion of $k_z = \pi$ states produces a much more anisotropic set of scattering vectors. However, compared to the equivalent 2eP model, the scattering vectors are observed to be much more anisotropic. This is in quantitative agreement with experiment. This agreement is highlighted by the yellow, red and green arrows in Fig. 5.4(d,e). Thus, on the assumption that the

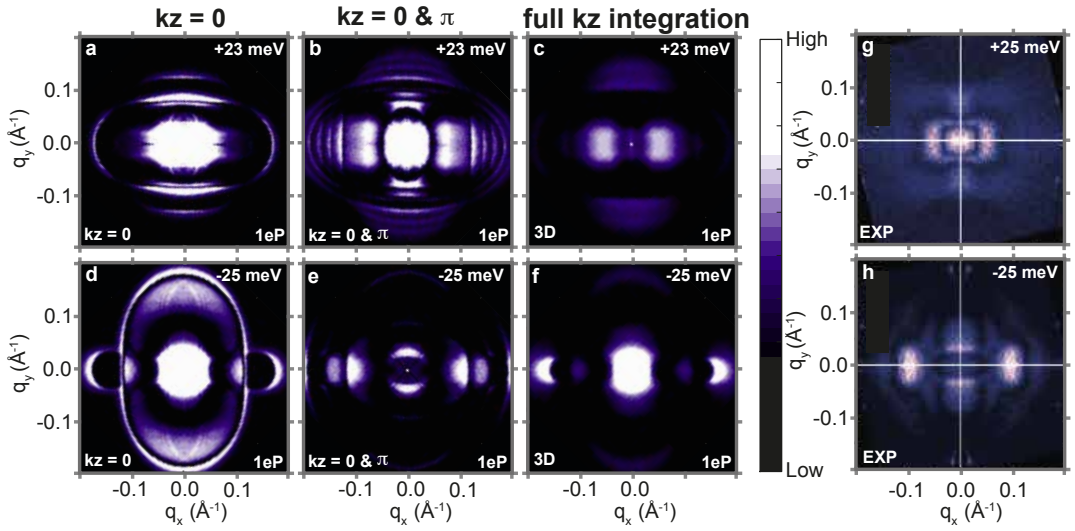

Figure 5.5: Comparison of the calculated Feenstra function of the 1eP model, for a 2D, $k_z = 0$, approximation of the electronic structure, an electronic structure where $k_z = 0$ and $k_z = \pi$ states contribute, and an electronic structure where all k_z states contribute. a-c) Calculated scattering vectors for $|L(q_x, q_y, \omega = +25 \text{ meV})|$. d-f) Calculated scattering vectors for $|L(q_x, q_y, \omega = -25 \text{ meV})|$. g,h) Experimental Feenstra function corresponding to +25 meV and -25 meV respectively, taken from Ref. [158].

1eP model is the correct description of the electronic structure, we can conclude that $k_z = \pi$ states also influence the scattering vectors at $\omega = -25\ meV$.

From these two energies, we conclude that $k_z = \pi$ states are detected in the experimental scattering dispersions measured in QPI. We find however that when we perform a full k_z integration, the calculated result does not reproduce the experimental data. In Fig. 5.5, we present the Feenstra function of the 1eP model again at $\omega = +25$ meV (Fig. 5.5(a-c)) and -25 meV (Fig. 5.5(d-f)). Fig. 5.5(a,b) and (d,e) are the same calculations as shown in Fig. 5.3 and 5.4 respectively. However, Fig. 5.5(c) and (e) represents the calculated Feenstra function where we included full k_z integration in the LDOS. This produces a more smeared out distribution of scattering vectors, which does not agree with the experimental results, again shown in Fig. 5.5(g,h). We find that including $k_z = 0$ and $k_z = \pi$ states is, however, sufficient to reproduce the experimental dispersion.

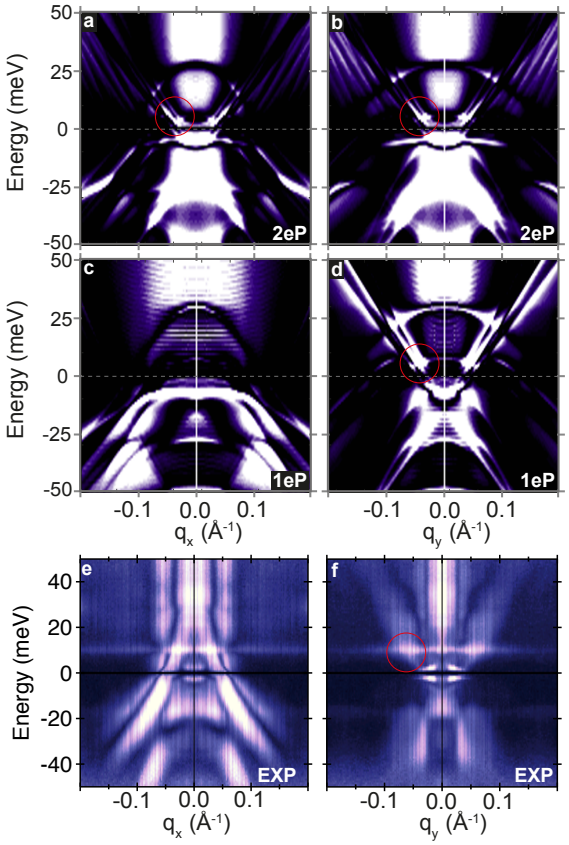

Figure 5.6: Comparison of the energy dependent scattering dispersions predicted from a 2eP tight binding model and a 1eP tight binding model. In both cases it is assumed that $k_z = 0$ and $k_z = \pi$ contribute to scattering. a) $|L(q_x, 0, \omega)|$ dispersion for the 2eP model. b) $|L(0, q_y, \omega)|$ for the 2eP model. c,d) Equivalent images for the 1eP model. e,f) The experimental data from Ref. [158]. The red circles highlight the presence of electron bands.

5.3.2 *Comparison of a "one electron pocket" model with a "two electron pocket" model*

Having justified the importance of $k_z = \pi$ states in the LDOS of FeSe, we now focus on identifying which model of FeSe best describes experimental reality. We have partially discussed this in the previous section by studying the Feenstra function at the specific energies of +25 meV and -25 meV. Now we will focus on the energy dependent dispersion of the scattering vectors.

In Fig. 5.6, we plot the QPI scattering dispersions between ± 50 meV along the q_x axis at $q_y = 0$ (left side of Fig. 5.6) and the q_y axis at $q_x = 0$ (right side of Fig. 5.6). In Fig. 5.6(a) and (b) we present the dispersions for the 2eP model. Both images look

qualitatively similar. This is not unexpected, the 2eP model describes an electronic structure which has the same number of hole and electron bands in both the k_x and k_y directions. The only presence of anisotropy, therefore, is in the elliptical scattering vectors associated with the hole pocket. This would change the position of certain scattering vectors in the q_x and q_y directions, but would not alter the number of scattering bands that would be present in both q_x and q_y cuts.

In the 1eP model, however, shown in Fig. 5.6(c) and (d), the electron band associated with d_{xz} orbital weight is no longer present in the q_x direction. Equivalently the d_{xy} electron band and the hole-like d_{xz} band that is present below the Fermi level around the M/A point are also not present in the q_y direction. This will then lead to a different number of hole and electron scattering bands in the q_x and q_y directions which will produce a highly anisotropic scattering dispersion.

In Fig. 5.6(e,f) we show the experimental QPI dispersions of Ref. [158] for comparison. The highly anisotropic dispersion between the q_x and q_y images are in much better agreement with our calculation for a 1eP model than with the 2eP model. In particular, the 2eP model suggests that scattering dispersions from electron bands should be present in both the q_x and q_y direction, as highlighted by the red circles in Fig. 5.6(a,b). However, in the experimental images, scattering vectors associated with electron bands are only observed in the q_y direction, again highlighted by a red circle in Fig. 5.6(e). This is in direct agreement with the 1eP model and is strong evidence to suggest that only one electron pocket is present at the Fermi surface of FeSe within the nematic state.

Finally, we compare the Feenstra function calculated using the 2eP model and the 1eP model at a range of energies. In Fig. 5.7(a-f) we present the calculated Feenstra function at +25 meV, +15 meV, +6 meV, -7 meV, -15 meV and -25 meV. The corresponding 1eP calculations are presented in 5.7(g-l). For each energy, we find that the 1eP model is in better qualitative agreement with the experimental dispersions shown at +25 meV, +15 meV, +5 meV, -5 meV, -15 meV and -25 meV respectively in Fig. 5.7(m-r). Here, as the model is optimised to experimental ARPES data, with a typical energy resolution of $\sim$5 meV [102], we choose the energies that best match the experimental dispersions within a $\pm$5 meV energy range. At +25 meV, the 1eP model captures the diffuse scattering vectors highlighted by the yellow arrow, which is not observed in the 2eP calculation. At +15 meV, the 2eP model suggests a qualitatively different set of scattering vectors should be present, compared to what is observed in the experimental measurement of Fig. 5.7(l). The 1eP calculation, however, does cor-

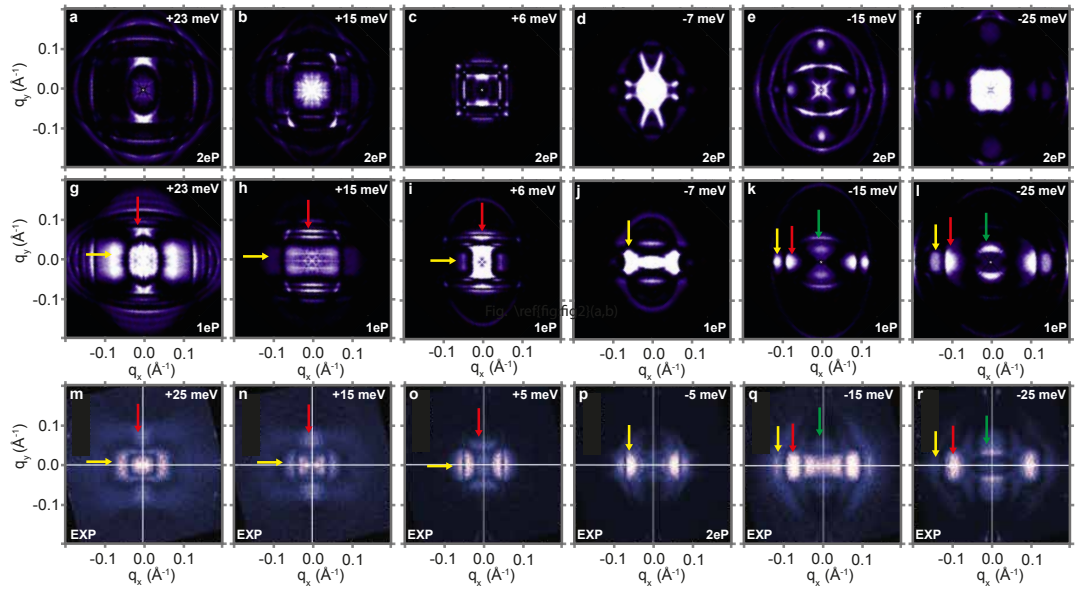

Figure 5.7: Comparison of the Feenstra function, $|L(q_x, qy, \omega)|$, for the 2eP and 1eP models of FeSe at various energies. a-e) Feenstra function of the 2eP model for ω = a) +25 meV b) +15 meV, c) +6 meV, d) -7 meV, e) -15 meV, f) -25 meV. g-l) Equivalent images for the 1eP model of FeSe. The experimental data of Ref. [158] is presented for comparison in (m-r). The arrows are used to highlight agreement between theory and experiment.

rectly capture the main features shown in the experiment. At +6 meV, the 2eP model produces a nearly four-fold symmetric, square-like dispersion, whereas the 1eP model suggests a much greater anisotropy between the bright regions, highlighted with a red arrow in Fig. 5.7(h), and the weaker regions, highlighted with a yellow arrow. Whilst the intensity with the experimental data of 5.7(m) is opposite to that predicted for the 1eP model, the scattering vectors that are calculated are in quantitative agreement with the experimental result whereas the 2eP calculation predicts additional scattering vectors not observed in the experimental data. At -7 meV, the 2eP model suggests two perpendicular sets of scattering vectors, arising from the two electron pockets, should be present. However, the experimental data, of Fig. 5.7(n), shows only two bright features. These two features are correctly described within the 1eP model presented in Fig. 5.7(j). At -15 meV, the 2eP calculation (Fig.5.7(e)) and 1eP calculation (Fig.5.7(k)) suggest a very different set of scattering vectors. The 1eP model presents a much more anisotropic dispersion, which is in better agreement with experiment. Three of the four main features are quantitatively accounted for within the 1eP scenario, whereas the 2eP model does not agree at all with experiment. It is noted that

the central scattering vector observed in the experimental data of Fig. 5.7(q) is not captured within the 1eP model. The origin of this discrepancy is unknown. Finally, at -25 meV the 2eP model, of Fig. 5.7(f), suggests that the most intense scattering vectors will be located around $\mathbf{q} = (0,0)$, whereas the 1eP model of Fig. 5.7(l) describes a highly anisotropic set of scattering vectors, which is in direct agreement with experiment. The quantitative agreement is highlighted by the yellow, red and green arrows.

We thus conclude that the QPI scattering dispersions measured by Hanaguri *et. al.* [158] support the conclusions obtained from detwinned ARPES experiments, that is that the electronic structure of FeSe is best described by the "one electron pocket" model.

5.4 Discussion

In this chapter we have determined two key pieces of information regarding QPI experiments of FeSe and the electronic structure of the nematic state.

Firstly, we have provided evidence that finite k_z states play a role in the scattering dispersion detected by QPI experiments. This was initially suggested by Hanaguri *et. al.* from analysis of the experimental data, and we have been able to confirm this with theoretical calculations. Specifically, we find that including $k_z = 0$ and $k_z = \pi$ states is sufficient to reproduce the observed scattering dispersions. The current microscopic reason for this is unknown, however, as suggested by Hanaguri, *et. al.* [158], it may relate to the fact that scattering probabilities will be dominated by the extremal areas of the Fermi surface. Another possibility is that defects not located at the surface of the material may contribute, which would produce a finite q_z dependence in the LDOS. Additional work studying the assumptions of Bardeens theory of tunnelling [184] and the surface electronic structure of FeSe are required to shed light on this observation.

By including the three-dimensionality of the electronic states, albeit in a simplified manner, we attain significantly better agreement overall than was reported by Kostin *et. al.* [159], who only used a $k_z = 0$ model of FeSe. In both that study and this, we find agreement that a conventional 2D 2eP model can not reproduce the experimental data and that a significant anisotropy had to be included into the simulations in order to reproduce the strongly twofold-symmetric QPI patterns. Whilst Kostin *et. al.* assumed highly anisotropic, orbitally selective, quasiparticle weights, which suppresses the spectral weight of the d_{xz} and d_{xy} states, we use a 1eP model of the electronic struc-

ture. This has the advantage of correctly reproducing the experimental dispersions observed by photoemission experiments on detwinned crystals of FeSe, as well as preserving the scattering vectors associated with the outer hole band, which is composed of predominantly d_{xz} weight, and is detected in ARPES experiments [95].

Finally, we have provided additional evidence that the physical electronic structure of FeSe in the nematic state is incompatible with a model that describes a Fermi surface with two electron pockets. This result is in direct agreement with detwinned ARPES measurements of FeSe, and was obtained by an experiment which was not subject to external strain. As discussed in Chapter 4, the origin of this unusual electronic structure is unknown, however, the additional evidence from the independent technique of QPI suggests that the “one electron pocket" model of FeSe is the true description of the nematic phase.

It would be informative to repeat the calculations presented in this chapter for the isovalent sulphur doped $FeSe_{1-x}S_x$ series, for which experimental data has been obtained by Hanaguri *et. al.* [158]. This doping suppresses the nematic state, up to a critical doping of $x = 0.18$. Beyond this value, the tetragonal electronic structure of FeSe is recovered [176, 186], and a Fermi surface consisting of two electron pockets is observed in ARPES measurements [144, 176, 186]. Thus, at some point in this doping series a transition between a “one electron pocket" Fermi surface and a “two electron pocket" Fermi surface must occur. It would be useful to determine where this transition lies, in order to gain additional information about the response of the nematic state to the electronic structure of FeSe.

5.5 Conclusion

We have studied the complimentary experimental technique of QPI in order to gain additional insight into the electronic structure of the nematic state of FeSe. We find that the QPI data is in direct agreement with the results obtained from ARPES measurements on detwinned crystals, specifically, that two bands, which are predicted to appear around the M point, are not present. Thus we can conclude that the Fermi surface of FeSe consists of only one hole pocket and one electron pocket.

We have also studied the k_z dependence of the QPI spectra. We find evidence that scattering vectors associated with $k_z = \pi$ states are also present in the experimental dispersion of FeSe. This result raises questions about how 3D materials should be accounted for within experimental and theoretical treatments of QPI.

The results presented in this chapter unifies both tunnelling and photoemission based experiments on FeSe and provides important insight into the consequence of nematicity on the electronic structure of FeSe in a single domain. This conclusion will directly influence our study of the superconducting state in the next chapter.

6 | The superconducting gap structure of FeSe

6.1 Introduction

Over the course of this thesis, we have uncovered the foundations of the electronic structure of FeSe. We began by studying the electronic structure of the tetragonal phase above 100 K, and observed how the electronic structure spontaneously evolved upon entering the nematic phase as the temperature was cooled below 90 K. Here, we made the surprising observation that the Fermi surface of FeSe in the nematic state consisted of only one hole pocket and one electron pocket. This was in contradiction to ab-initio calculations and previous assumptions of the electronic structure, which suggested that a Fermi surface consisting of one hole pocket and two electron pockets should be present. The origin of this disagreement between theory and experiment remains unclear, however, now that we have determined the experimental low temperature electronic structure of FeSe, we are finally in a position to study what is arguably the most important phase of this material, the superconducting state.

Superconductivity in the iron-based superconductors generally occurs in close proximity to an antiferromagnetic phase [187]. This observation has led to the suggestion that superconductivity may be mediated by local, instantaneous and repulsive Coulomb interactions [80], generally referred to as spin-fluctuation mediated superconductivity [89]. Evidence for this mechanism has been inferred by the observation of a spin-resonance peak in the superconducting state [188, 189], and the detection of a sign change in the superconducting gap of some systems [13, 190]. However, more evidence is required to confirm the validity of spin fluctuation mediated superconductivity in the iron-based superconductors.

As the Coulomb potential is inversely proportional to the distance between two fermions, the spin-fluctuation mediated pairing interaction will be largest between

fermions in the same orbital. As a consequence of this, pairing between two fermions in momentum space will be largest if those states have the same underlying orbital character. An identifier of spin-fluctuation mediated superconductivity, therefore, would be the observation of a superconducting gap which is sensitive to the orbital content at the Fermi surface. In most iron-based superconductors, the complexities of the multi-band, nematic and antiferromagnetic electronic structure make the verification of this link challenging. However, we have gained sufficient knowledge of both the experimental and theoretical electronic structure of FeSe to be able to determine whether this hypothesis holds.

In this chapter, I will use ARPES to simultaneously measure the momentum dependence of the superconducting gap of FeSe and the orbital content of the bands for the full, three-dimensional, electronic structure. From this, it will become apparent that the superconducting gap of FeSe directly scales with the d_{yz} orbital weight at the Fermi level, which supports the spin-fluctuation pairing hypothesis. I will then perform theoretical calculations modelling the momentum dependence of the superconducting gap of FeSe, assuming that superconductivity is mediated by spin fluctuations. I will show that the calculated gap structure is in direct agreement with the experimental results if the model takes into account all the features of the electronic structure that have been determined during the course of this thesis. This includes the momentum dependent nematic band shifts determined in Chapter 4 and, most importantly, the correct “one electron pocket" description of the electronic structure, which has been discussed in Chapter 4 and Chapter 5. I will conclude with a discussion of the consequences of nematicity and superconductivity, and compare these results with other theoretical interpretations.

6.2 Experimental methodology

6.2.1 Determination of orbital content at the Fermi level

As discussed in Section 2.4.2, photoemission experiments are sensitive to the symmetry of the underlying orbital character of the band. By using different polarisations of light, it is possible to excite electrons only from the orbitals that are either symmetric or antisymmetric with respect to the propagation of light.

Numerical simulations for the matrix elements of the d-orbitals suggest that bands with d_{xz} and d_{yz} orbital character will couple strongly to opposite polarisations of light [191]. The d_{xz} orbital character will be excited under Linear Horizontal (LH) polarised

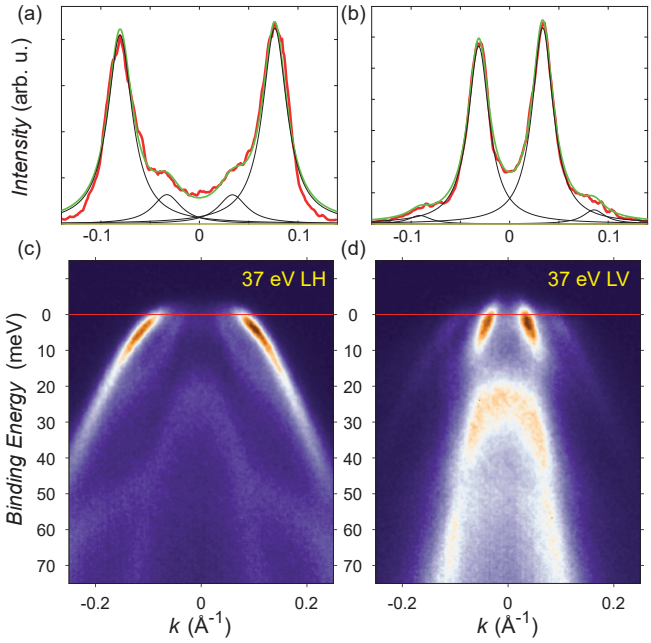

Figure 6.1: Band dispersion and MDC of the Γ point of FeSe measured at 10 K using a photon energy of 37 eV. a) MDC of (c), taken at the Fermi level, measured under LH polarised light. b) MDC of (d), taken at the Fermi level, measured under LV polarised light. c) Band dispersion of the Γ point under LH polarised light. d) Equivalent band dispersion measured under LV polarised light.

light, whereas d_{yz} orbital character will be visible under Linear Vertical (LV) polarised light. The d_{xy} orbital character will only be very weakly observed in both polarisations within the first Brillouin zone, however residual weight may still be observed when the sample is rotated off the high symmetry axis [102]. Therefore, to a first approximation, the intensity of the single particle spectral function under LV polarised light can be assumed to be directly proportional to the d_{yz} weight at the Fermi surface and LH polarised light may be assumed to be directly proportional to the d_{xz} orbital weight.

In most scenarios, only qualitative information about the orbital content can be obtained. However, the Γ point of a twinned sample of FeSe is a special case, where it is possible to extract numerical estimates for the ratio of d_{xz} weight to d_{yz} weight. This is possible for three reasons, firstly, the single band crossing the Fermi level is clearly separated from other spectral weight, secondly, the band can approximately be described as a combination of only two orbital characters, and thirdly, due to the rotational symmetry of the d_{xz} and d_{yz} orbitals, the twinning effect of an orthorhombic crystal allows us to probe both orbital characters within the same experimental measurement. By fitting the Momentum Distribution Curves (MDCs) around the Fermi

level of Fig. 6.1 with four Lorentzian functions, we can extract the amplitude of the outer band (O) and the inner band (I). This corresponds to the intensity of the d_{xz} or d_{yz} weight from both the main elliptical hole pocket (outer branch) and the 90° rotated hole pocket (inner branch)[1].

From this, we can obtain ratios of the intensity of the d_{xz} and d_{yz} states from a single MDC. The data measured under LH polarised light (Fig. 6.1(a) and (c)) gives $\frac{O_{d_{xz}}}{I_{d_{yz}}} = 16$ and the data measured under LV polarised light (6.1(b) and (d)) gives $\frac{O_{d_{yz}}}{I_{d_{xz}}} = 0.19$. Here, we are assuming that the orbital characters couple perfectly to one polarisation and that only the d_{xz} and d_{yz} orbital characters contribute at the Fermi level. From this assumption, we can also write $W_{d_{xz}} + W_{d_{yz}} = 1$. Here W is the intensity of either the inner or outer band. By solving this set of linear equations, we obtain d_{yz} = 0.18 on the minor axis of the ellipse, and 0.05 on the major axis. This indicates that the d_{yz} weight is greatest along the sides of the elliptical hole pocket. However, the dominant orbital character at the Γ point is the d_{xz} weight, which is always greater than 80%.

We use this method to provide a quantitative estimate for the ratio of the orbital characters at the Γ point. However, at other momenta, such as the Z point, this is not possible. The d_{yz} band observed at -20 meV in Fig. 6.1(d) is now much closer to the Fermi level, which as a consequence overlaps with the spectral weight of the hole band crossing the Fermi level. This makes it impossible to clearly resolve the two bands. Despite this, the numerical estimate will prove useful in the following discussion and a visualisation of these results is shown in Fig. 6.3(e).

6.2.2 Determination of the superconducting gap from ARPES data

In the ARPES data, presented in this chapter, we report the leading edge gap (LEG) as the quantity that defines the magnitude of the superconducting gap. The LEG measures the shift to the position of the Energy Distribution Curve (EDC) where the Fermi function is equal to 0.5. Above T_c this is equivalent to the chemical potential, however below T_c the LEG will shift to a negative value, due to the formation of gapped states around the Fermi level. Whilst this value is not equivalent to the true gap, the LEG is much less sensitive to the overall resolution of the experiment, as well as the exact location of the Fermi level [192].

To estimate the size of the true superconducting gap, we compare the experimental EDC, both above and below T_c, to the Fermi-Dynes function,

[1]The Fermi surface of a twinned hole pocket of FeSe is discussed in Section 4.4.

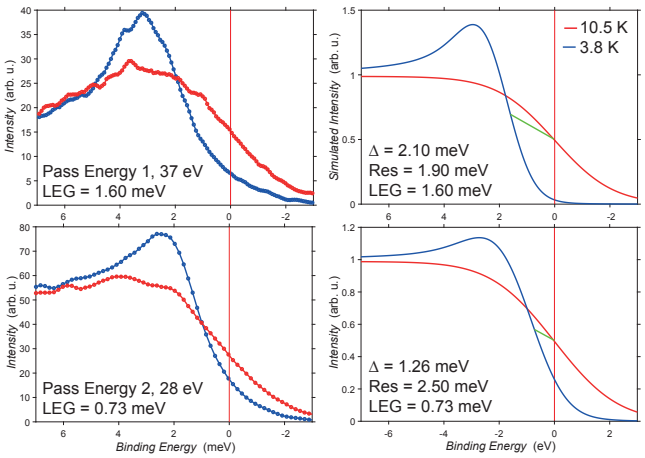

Figure 6.2: Comparison of the experimental EDCs (left) with simulations of the Fermi-Dynes function (right). Red curves describe ARPES data at 10.5 K, above T_c, blue curves describe data collected at 3.8 K, below T_c. The parameters used in Eq. (6.1) are presented within the figures on the right hand side, where Res = Γ.

$$N(\omega) = N_0 Re\left[\frac{\omega + i\Gamma}{\sqrt{(\omega + i\Gamma)^2 - \Delta^2}}\right] f(\omega, T). \tag{6.1}$$

Here, $N(\omega)$ is the density of states at energy ω, N_0 is the density of states above T_c, Γ is the experimental resolution, Δ is the magnitude of the superconducting gap and $f(\omega, T)$ is the Fermi function which accounts for the finite temperature. In Fig. 6.2 we show both the raw data (left), and Fermi-Dynes simulation (right), for two different momenta both above T_c (red curve) and below T_c (blue curve). By comparing the simulation and experimental data of the normal state (red curve), where $\Delta = 0$, we can obtain an estimation for the resolution of the experiment. By using the same resolution, we can then compare the simulation of the superconducting state (blue curve) to the 3.8 K data, using Δ as a tuning parameter, and obtain an estimate for the true superconducting gap at a given momenta.

6.3 Experimental Results

6.3.1 Hole pocket

We begin by discussing the Fermi surface and orbital content of the $k_z = 0$, Γ point of FeSe. In Fig. 6.3(a,b) we present Fermi surface maps at 10 K, in both LH and LV polarisation, using 37 eV photons. As discussed in Sec. 6.2.1, the hole pocket at Γ is dominated by d_{xz} weight, which is observed under LH polarised light. By switching to

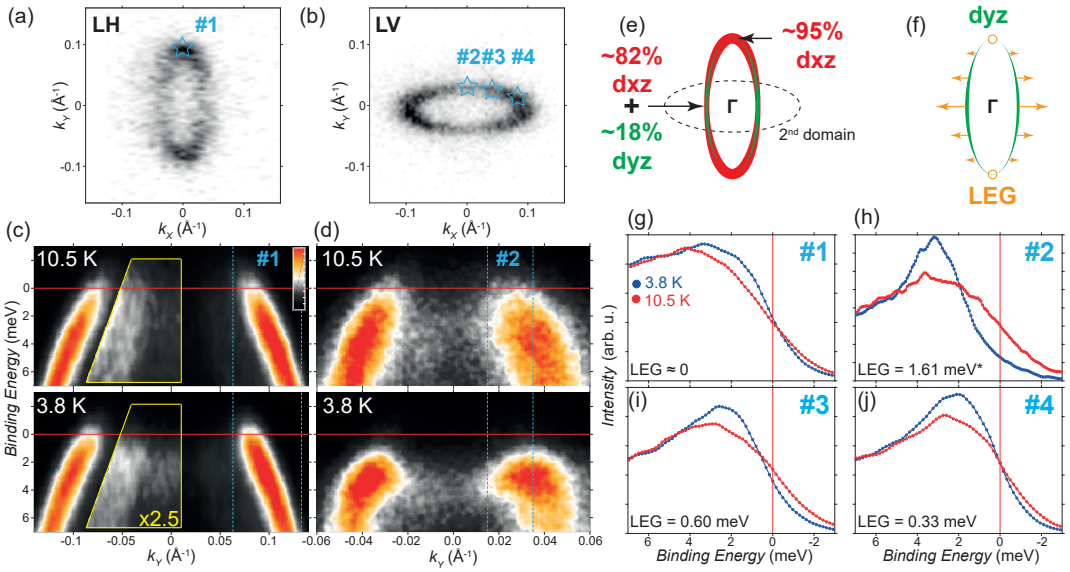

Figure 6.3: a,b) Fermi surface maps of twinned FeSe samples around the Γ point (37 eV), in both linear polarizations. c) High-symmetry dispersions in LH polarisation above and below T_c. d) High symmetry dispersion in LV polarisation, highlighting the shorter axis of the ellipse. e) Schematic of the distribution of orbital weights. f) Schematic correlation between the LEG and the d_{yz} orbital character. g,h) EDCs integrated in small regions (cyan dashed lines in (c,d)) around k_F . i,j) EDCs at positions shown in (b), off the high-symmetry axes. *Note that (d) and (h) are obtained with a higher resolution than other plots.

LV light, we observe states from the hole pocket originating from the second domain, which is rotated 90° degrees and therefore detected using the opposite polarisation of light. From the quantitative analysis, discussed in Sec. 6.2.1, we have determined that the hole pocket at Γ is composed of 82 % d_{xz} weight along the minor axis of the ellipse, which increases to 95 % along the major axis of the ellipse. The remaining spectral weight is attributed to the d_{yz} orbital character as sketched in Fig. 6.3(e).

We now study the superconducting gap as a function of angle around the elliptical Fermi surface. In Fig. 6.3(c), we present band dispersions above and below T_c corresponding to a cut along k_y for $k_x = 0$. There is no evidence of Bogoliubov backbending at this momenta, with the bands both above and below T_c appearing to cross the Fermi level. This does not necessarily imply that a gap does not exist, only that the gap is smaller than our experimental resolution of ~ 2 meV [95]. In Fig. 6.3(d), we use the hole pocket originating from the twinned domain and present a band dispersion along the minor axis of the ellipse. Below T_c, a clear Bogoliubov backbending of the band is observed, indicating a superconducting gap. In Fig. 6.3(g) and (h), we present EDCs integrated around k_F, corresponding to the band dispersions of Fig. 6.3(c) and (d).

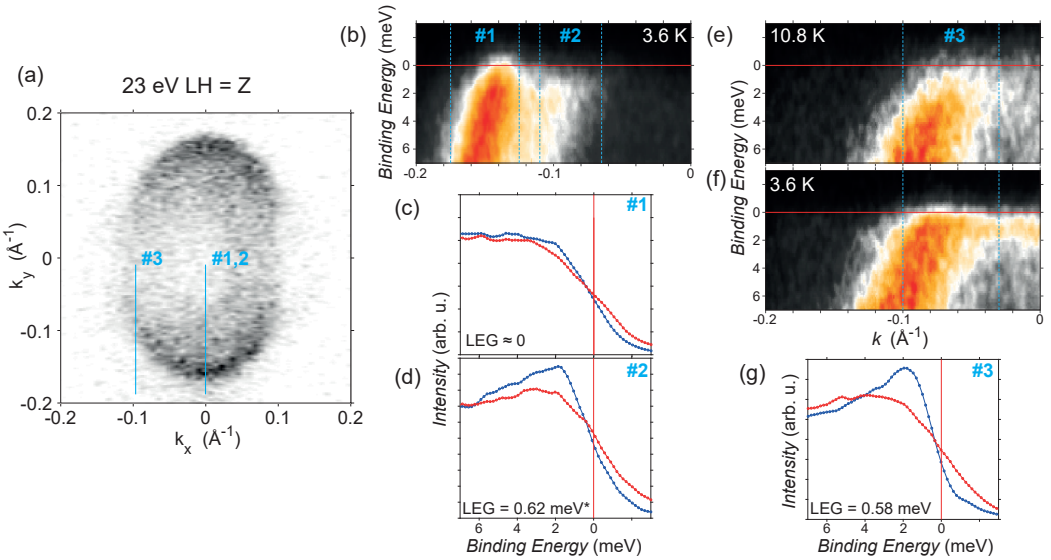

Figure 6.4: a) Fermi surface of the hole pocket of FeSe at the Z point. b) High symmetry cut, focusing on the hole band dispersions along k_y for $k_x = 0$. c) EDC above (red line) and below (blue line) T_c corresponding to #1 in (b). d) equivalent EDC for region #2 of (b). e,f) Band dispersion off the high symmetry axis above and below T_c corresponding to #3 in (b) . The Bogoliubov backfolding can be seen in the raw data. (g) EDC above and below T_c for region #3.

We find a maximum LEG of 1.6 meV in Fig. 6.3(h), which corresponds to a true gap of 2.1 meV at 3.8 K[2]. In Fig. 6.3(i) and (j), we show EDCs off the high symmetry axis, the exact positions are marked as #3 and #4 in Fig. 6.3(b). We find that the gap continuously decreases as we move from the minor axis of the ellipse, where the d_{yz} weight is largest, to the major axis of the ellipse, where the gap is not resolved, and the d_{yz} weight is less than 5% of the orbital content. This is presented pictorially in Fig. 6.3(f).

We now focus on the Z point of FeSe, the hole pocket at $k_z = \pi$. Here, at 23 eV, it is not possible to perform the same numerical analysis of the orbital content as performed at the Γ point, as discussed in the section 6.2.1. However, it can be qualitatively observed, from the Fermi surface map of the Z point under LH polarised light (Fig. 6.4(a)), that there is a greater variation of intensity between the minor axis and the major axis of the ellipse. This indicates that there is also a greater variation of d_{xz} weight to d_{yz} weight.

By studying the band dispersions in Fig. 6.4(b), we are still able to detect both an outer (#1) and inner (#2) band, corresponding to the hole pocket from two rotated

[2]Determined using the methodology described in section 6.2.2.

domains. The integrated EDC around each of these k_F values in Fig. 6.4(c) and (d) reveal that no gap is detected along the major axis of the ellipse, however a gap is still detected along the minor axis. In Fig. 6.4(e) and (f) we present band dispersions at a momenta off the high symmetry axis. Here, the Bogoliubov backbending is identifiable in the raw data of Fig. 6.4(f) and seen as a peak in the EDC of Fig. 6.4(g).

We therefore find that the momentum dependence of the gap at the Z point is equivalent to that at Γ. We qualitatively infer that the gap at the hole pocket follows the symmetry of the d_{yz} weight. We also find that the absolute magnitude of the superconducting gap appears smaller at the Z point, at roughly half the size of the gap at the Γ point.

Comparison with Literature

Xu *et. al.* [193] had previously studied the Z point of 7% sulphur doped FeSe using ARPES via synchrotron radiation. The highly anisotropic two-fold momentum dependence of the gap is in agreement with our results here for pure FeSe. However, they were not able to resolve the gap at the Γ point. Liu *et. al.* [194] have reported a laser ARPES study on the hole pocket of FeSe using 6.994 eV photons. Due to the low photon energy k_z is not well defined, so a precise definition of Γ and Z is not possible. In this report they claim a highly two-fold momentum dependence of the gap, in agreement with the conclusions drawn here. Hashimoto *et. al.* [195] performed a similar laser ARPES study using 6.994 eV photons. They present a gap structure from a twinned sample which follows a more exotic angular dependence, with a $\cos(8\theta)$ component. This is in disagreement with our experiment, the experimental of *Xu et. al.* [193] and the equivalent laser ARPES study by Liu *et. al.* [194] which all suggest that the gap at the hole pocket can be described by $\cos(2\theta)$.

Kushnirenko *et. al.* used synchrotron radiation on pure FeSe and studied the gap at both Γ ($h\nu = 37$ eV) and Z ($h\nu = 21$ eV) [196]. In both cases, we find that our results are in agreement with the momentum dependence of the superconducting gap determined in their study. We also find agreement with the magnitude of the gap that they determined at the Z point. However, we find that the maximum gap at the Γ point is twice the size of the Z point, whereas Kushnirenko *et. al.* report a smaller gap at Γ. This discrepancy highlights the challenge of measuring a superconducting gap on the order of 1 meV, using photons energies of 37 eV.

Finally, Bugoliubov Quasiparticle Interference experiments on FeSe have also been reported by Sprau *et. al.* [157]. Whilst the three-dimensional nature of this technique

is unclear, the in plane momentum dependence of the superconducting gap at the hole pocket is in agreement with our observations, as is the magnitude of the superconducting gap at the Γ point.

6.3.2 Electron pocket

We now focus our attention on the electron pocket of FeSe. In Fig. 6.5(a) we present the Fermi surface map of the A point, using 28 eV photons and LV polarised light. The interpretation of the orbital content at the electron pocket is more complicated than at the hole pocket. Here, the centre of the electron pocket is also the corner of four different Brillouin zones in the 2-Fe unit cell. The transition between the first and second Brillouin zone in FeSe reverses the parity of the d_{xz} and d_{yz} orbitals due to the glide symmetry of the lattice. Thus, whilst the peanut oriented along the k_y axis (from the second orthorhombic domain) should have d_{xz} orbital character, it is still observed under LV polarised light. Under LH polarised light in Fig. 6.5(b), the tips of the electron pocket in the 1st and 3rd Brillouin zones are also detected. From first principle calculations, these should be of d_{xy} weight [102]. The parity switching effect does not apply to the d_{xy} orbital, and thus only the tips parallel to the k_x axis are observed. This would imply that the d_{xy} tips of the electron pockets should also be observed in LV polarisation, however from the numerical analysis of the matrix elements [191], the d_{xy} weight in LV polarisation at this momenta should be negligible and thus will not be observed. The orbital character of the electron pocket from a single domain is drawn schematically in Fig. 6.5(c). The length of the peanut shaped feature is predominantly d_{yz} orbital character, with d_{xy} weight at the tips.

In Fig. 6.5(d-g), we show the evolution of the band dispersion both above and below T_c for the electron pocket, at the specified k_x momenta, labelled as #1 to #4 in Fig. 6.5(a). At 3.7 K, backbending of the bands can be observed along the length of the peanut. This is shown by the detection of a coherence peak and LEG in the EDCs (Fig. 6.5(h-k)). Here the EDCs have been integrated around k_F, as shown by the dashed blue lines in Fig. 6.5(d-g). The coherence peak and LEG remain roughly equivalent along the length of the peanut, where the orbital character is dominated by d_{yz} weight. However, the LEG decreases close to the tips of the electron pocket (Fig .6.5(g) and (k)).

Using 42 eV photons, we study the M point of FeSe. In Fig. 6.6(a), we present a Fermi surface map, which has a smaller k_F than the A point. Despite this, the orbital analysis remains equivalent. The one exception is the slight observation of the tip of

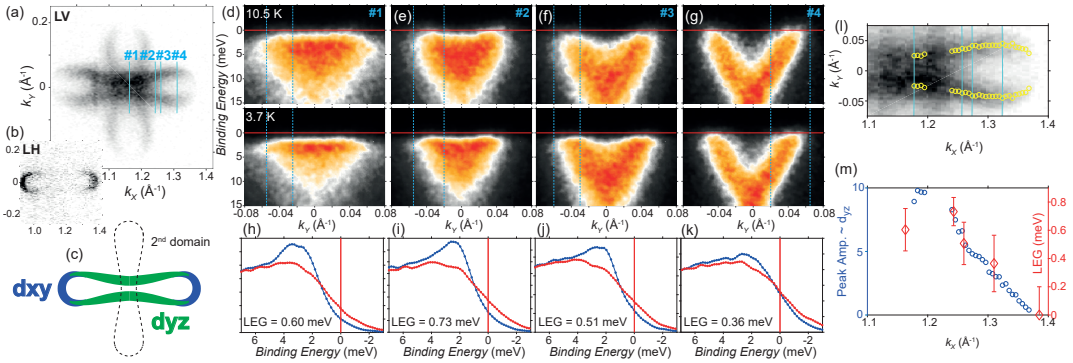

Figure 6.5: a,b) Fermi surface maps of twinned FeSe at the A point (28 eV) in LV (a) and LH (b) polarisation. c) Schematically representation of the orbital character of the electron pocket. d-g) Cuts along k_y , above and below T_c. h-k) EDC's above T_c (red) and below T_c (blue) Integrated around k_F in (d-g). l) Section of the Fermi surface used for peak-fitting analysis. The yellow circles indicate the peak positions. m) Peak amplitude from fitting the Fermi surface, which is proportional to the d_{yz} orbital character. The decrease in the LEG (red) with k_X correlates with the decrease in d_{yz} orbital character (blue).

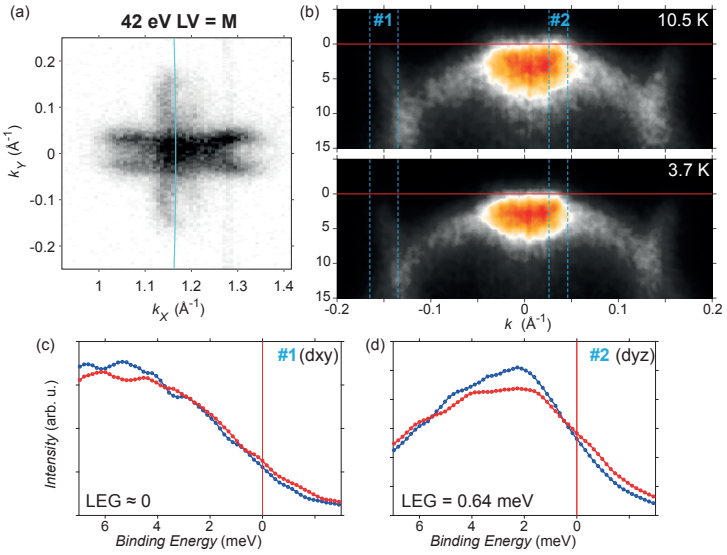

Figure 6.6: a) Fermi surface of FeSe at the M point (42 eV, LV). b) Band dispersions above and below Tc; note that the cut is very slightly off the high symmetry axis in order to obtain higher intensity on the outer band with d_{xy} character. c) EDCs for the outer band with d_{xy} character both above T_c (red) and below T_c (blue). d) EDC's for the inner band with d_{yz} character.

the electron pocket parallel to the k_y axis. The band dispersion for the cut, indicated by the blue line in Fig. 6.6(a), is shown in Fig. 6.6(b). No gap was detected at the tip of the electron pocket, indicating that the gap is below the experimental resolution (Fig.

6.6(c)). However, a LEG of 0.64 meV was detected for the band near the centre of the electron pocket (Fig. 6.6(d)). Whilst detecting a gap of < 1 meV using 42 eV photons is challenging, the detection of the LEG suggests that the momentum dependence at the M point is equivalent to that of the A point.

Comparison with Literature

Measurements of the electron pocket of FeSe have been much harder to obtain due to the higher photon energies required to reach the corner of the Brillouin zone. Consequentially, a higher energy resolution is required to resolve the gap. However, Kushnirenko *et. al.* [196] have recently reported the momentum dependence of the superconducting gap at both the M ($h\nu = 42$ eV) and A ($h\nu = 28$ eV) point. We find agreement with their measured momentum dependence and magnitude of the superconducting gap at both the M and A point.

The momentum dependence of the superconducting gap at the electron pocket has also been determined by BQPI [157]. Again, the k_z nature of this technique is not apparent, however our results are in agreement with the in plane momentum dependence of the gap determined via this method.

6.3.3 Scaling of superconducting gap with orbital character

Having observed that the magnitude of the superconducting gap is always largest where the d_{yz} weight of the band is maximum, we can make the qualitative statement that the magnitude of the superconducting gap appears to follow the d_{yz} orbital character. At the electron pocket, we can go one step further and provide evidence for a quantitative scaling between d_{yz} weight and gap magnitude. In Fig. 6.5(f) we present a close up of one lobe of the electron pocket. Here we extract out the amplitude of the peak under LV polarisation, which we assume is directly equivalent to the d_{yz} weight. In Fig 6.5(m) we plot this peak amplitude as a function of momentum on top of a plot of the LEG as a function momentum. We find a direct scaling between the magnitude of the LEG and the magnitude of d_{yz} orbital character of the band. Thus, we find evidence for a direct linear relationship between orbital character and gap magnitude. We conclude from this that the superconducting gap scales with orbital character.

6.4 Theoretical modelling of the superconducting gap

We have found experimental evidence to suggest that the gap magnitude follows the d_{yz} weight of a band. This suggests that superconducting pairing in FeSe is sensitive to orbital content, as would be expected from a pairing mechanism involving spin fluctuations.

Unlike phonon-mediated superconductors, there is no analytical theory for spin-fluctuation mediated superconductivity. However, it is still possible to extract numerical information out of a specific system, provided the electronic structure is known. Throughout this thesis we have developed a model of FeSe which can quantitatively describe the electronic structure observed in ARPES experiments. Thus, we are in a position to attempt to model the superconducting gap of FeSe. In this section we will solve the linearised gap equation for FeSe under the assumption of spin-fluctuation mediated superconductivity, and compare with our experimental results.

6.4.1 Pairing vertex

The formation of a Cooper pair may be described by the following Hamiltonian [15].

$$\hat{H} = \hat{H}^0 + \sum_{\mathbf{k}\mathbf{k}'} \Gamma(\mathbf{k},\mathbf{k}') c^\dagger_{\mathbf{k}\uparrow} c_{-\mathbf{k}\downarrow} c^\dagger_{\mathbf{k}'\downarrow} c_{-\mathbf{k}'\uparrow} \tag{6.2}$$

Here $\hat{H}^0$ is the non-interacting Hamiltonian. $c^\dagger_{\mathbf{k}\sigma}$ and $c_{\mathbf{k}\sigma}$ defines the creation or annihilation operators for a fermion with momentum, $\mathbf{k}$ and spin σ and $\Gamma(\mathbf{k},\mathbf{k}')$ describes the pairing vertex, which couples two fermions at different momenta.

In the case of phonon-mediated BCS superconductivity, $\Gamma(\mathbf{k},\mathbf{k}')$ is assumed to be a constant. Thus, it becomes possible to derive an analytical model for the ground state wavefunction of phonon-mediated superconductors assuming a mean field approximation [15]. However, as spin-fluctuations are strongly momentum dependent [89, 161], this assumption no longer applies. We must therefore define a pairing vertex which can couple two fermions via spin-fluctuations.

Such a pairing vertex can be derived using the fluctuation-exchange approximation (FLEX), originally developed by Bickers and Scalapino [197],

$$\Gamma(\mathbf{k},\mathbf{k}') = \frac{3}{2}U^2\chi^S(\mathbf{q}) - \frac{1}{2}U^2\chi^C(\mathbf{q}) + U, \tag{6.3}$$

This equation was then generalised for use in multiorbital systems by Graser *et. al.*

[89],

$$\Gamma^{pq}_{st}(\mathbf{k},\mathbf{k}',\omega) = \left[\frac{3}{2}U^S\chi^S(\mathbf{q},\omega)U^S - \frac{1}{2}U^C\chi^C(\mathbf{q},\omega)U^C + \frac{1}{2}U^S + \frac{1}{2}U^C\right]^{tq}_{ps} \tag{6.4}$$

Here p,q,s,t are orbital indices. $U^{S/C}$ is a matrix which includes local Coulomb repulsion and Hunds coupling in the spin or charge channel,

$$U^S = \begin{cases} U, & p=q=s=t \\ U', & p=s\neq q=t \\ J, & p=q\neq s=t \\ J', & p=t\neq q=s \\ 0, & otherwise \end{cases} \qquad U^C = \begin{cases} U, & p=q=s=t \\ -U'+2J, & p=s\neq q=t \\ 2U'-J, & p=q\neq s=t \\ J', & p=t\neq q=s \\ 0, & otherwise. \end{cases} \tag{6.5}$$

In these calculations we assume spin rotational invariance such that $U' = U - 2J$, and set $J = \frac{U}{6}$ with $J' = J$. U is set to 0.3 eV throughout. These parameters are equivalent to those used by Graser *et. al.* [89], however as long as the condition $U > U' > J$ is imposed, the qualitative features will remain consistent regardless of the numerical value of U, U' and J.

Finally $\chi^{S/C}(\mathbf{q})$ describes the spin susceptibility under the random phase approximation (RPA),

$$\chi^{C/S}(\mathbf{q}=\mathbf{k}-\mathbf{k}') = \frac{\chi^0(\mathbf{q})}{1\pm U^{C/S}\chi^0(\mathbf{q})}. \tag{6.6}$$

The non-interacting susceptibility matrix, χ^0, is then calculated via a convolution of two Green's functions in Matsubara space [89],

$$\chi^0_{pq;st}(\mathbf{q},i\omega_m) = -\frac{1}{N\beta}\sum_{\mathbf{k},i\omega_n} G_{sp}(\mathbf{k},i\omega_n)G_{qt}(\mathbf{k}+\mathbf{q},i\omega_n+i\omega_m). \tag{6.7}$$

Here, $\beta = \frac{1}{k_bT}$, where T is the temperature of the system, N is the number of Fe atoms, and $\omega_n = (2n+1)\pi T$, is the Matsubara frequency. We have used a 32x32x16 $\mathbf{k}$-grid to determine equation (6.7), and set the Matsubara cutoff to $n_{cutoff} = 128$ for a temperature of 10 K. Finally, the Green's function in Matsubara space is defined

$$G_{sp}(\mathbf{k}, i\omega_n) = \sum_{\mu} \frac{a^s_\mu(\mathbf{k}) a^{p*}_\mu(\mathbf{k})}{i\omega_n - E_\mu(\mathbf{k})}. \tag{6.8}$$

Here $a^s_\mu(\mathbf{k})$ projects the orbital space, s, p, into a band space, μ, as defined by the eigenvector of the Hamiltonian of our system, and $E_\mu(\mathbf{k})$ is the eigenvalue of the original Hamiltonian.

A full derivation and discussion of the FLEX approximation, the random phase approximation, and the non-interacting spin susceptibility, $\chi^0(\mathbf{q})$, is presented in Appendix B.

6.4.2 Linearised gap equation

To extract information about the momentum dependence of the superconducting gap we first make the assumption that the superconducting order parameter, $\Delta(\mathbf{k})$, can be decomposed into a magnitude, Δ, and a normalised symmetry function, $g(\mathbf{k})$,

$$\Delta(\mathbf{k}) = \Delta \cdot g(\mathbf{k}). \tag{6.9}$$

Under this assumption, we lose information regarding to the magnitude of the superconducting gap, but retain the momentum dependence. At values close to T_c, where only the leading instability is present, this is generally a valid approximation.
We are only interested in fixed energies contours in the study of superconductivity, thus the co-ordinate transformation,

$$\mathbf{k}_\parallel = v_F(\mathbf{k})(\mathbf{k} - \mathbf{k_F}), \tag{6.10}$$

is applied. This converts $\mathbf{k}$ into a contour of momenta specifically defined on the Fermi surface, where $\mathbf{k_F}$ is the momenta at the Fermi level and $v_F(\mathbf{k})$ is the Fermi velocity. To obtain the linearised gap equation, which can be solved to determine information about the pairing instability of a system, we define the expectation value for the pairing vertex as,

$$-\frac{\sum_\mu \oint_{C_\mu} \frac{d\mathbf{k}_\parallel}{v_F(\mathbf{k})} \sum_\nu \oint_{C_\nu} \frac{d\mathbf{k}'_\parallel}{v_F(\mathbf{k}')} g(\mathbf{k}) \Gamma_{\mu\nu}(\mathbf{k}, \mathbf{k}') g(\mathbf{k}')}{\sum_i \oint_{C_\mu} \frac{d\mathbf{k}_\parallel}{v_F(\mathbf{k})} g(\mathbf{k})^2} = \lambda. \tag{6.11}$$

Here, λ defines the leading pairing instability in the system. The minus sign is included as a convention such that the lowest (most negative) eigenvalue is the dominant

instability in the system and the summation of μ and ν define the sum over bands.

The pairing vertex, $\Gamma_{\mu\nu}(\mathbf{k},\mathbf{k}')$, is equivalent to the pairing vertex defined in Sec. 6.4.1, expected converted into band space,

$$\Gamma_{\mu\nu}(\mathbf{k},\mathbf{k}') = \sum_{stpq} a_{\mu}^{t*}(-\mathbf{k})a_{\mu}^{s*}(\mathbf{k})\mathrm{Re}[\Gamma_{st}^{pq}(\mathbf{k},\mathbf{k}',\omega=0)]a_{\nu}^{p}(\mathbf{k}')a_{\nu}^{q}(-\mathbf{k}'). \tag{6.12}$$

The expectation value of Eq. (6.11) is technically dependent on the summation over the imaginary part of the pairing vertex, $\Gamma_{st}^{pq}(\mathbf{k},\mathbf{k}',\omega)$, as a function of energy. However, as the vertex decays rapidly as we move away from the Fermi energy, we can perform a Krammers-Kronig transformation so that only the $\omega = 0$ real part of the pairing vertex [89] is required.

Finally, it is assumed that $\mathbf{k}$ is stationary and independent of $\mathbf{k}'$. This allows us to write the linearised gap equation as an Eigenequation,

$$-\frac{1}{4\pi^2}\sum_{\nu}\oint_{C_\nu}\frac{d\mathbf{k}'_{\parallel}}{v_F(\mathbf{k}')}\Gamma_{\mu\nu}(\mathbf{k},\mathbf{k}')g_\alpha(\mathbf{k}') = \lambda_\alpha g_\alpha(\mathbf{k}). \tag{6.13}$$

We thus perform an integral of the pairing vertex over all states $\mathbf{k}'$ present at the Fermi surface of each band, ν. The leading eigenvalue λ_0 then defines the dominant instability of the system, and the corresponding eigenvector $g_0(\mathbf{k})$ contains information on the momentum dependence and symmetry of the gap.

To ensure this equation produces real eigenvalues we require that the resulting matrix be Hermitian. To ensure this we multiply Eq. (6.13) by $\frac{\sqrt{d\mathbf{k}'_{\parallel}}}{\sqrt{v_F(\mathbf{k})}}$ and redefine our eigenvectors as

$$\tilde{g_\alpha}(\mathbf{k}) = \frac{\sqrt{d\mathbf{k}'_{\parallel}}}{\sqrt{v_F(\mathbf{k})}}g_\alpha(\mathbf{k}). \tag{6.14}$$

Here, $d\mathbf{k}'_{\parallel}$ has been discretised such that it is not an infinitesimally small quantity. This ensures the resulting matrix is now symmetric with respect to $\mathbf{k}$ and $\mathbf{k}'$,

$$-\frac{1}{4\pi^2}\sum_{\nu}\sum_{\mathbf{k}'_{\parallel}}\frac{\sqrt{d\mathbf{k}'_{\parallel}}\sqrt{d\mathbf{k}_{\parallel}}}{\sqrt{v_F(\mathbf{k}')}\sqrt{v_F(\mathbf{k})}}\Gamma_{\mu\nu}(\mathbf{k},\mathbf{k}')\tilde{g_\alpha}(\mathbf{k}') = \lambda_\alpha\tilde{g_\alpha}(\mathbf{k}). \tag{6.15}$$

To determine the momentum dependence of the superconducting gap we take the eigenvector, $g^0(\mathbf{k})$, corresponding to the leading eigenvalue. Each element of this eigenvector corresponds to the normalised magnitude of the superconducting gap at

a specific momentum on the Fermi surface, and can be directly compared with experiment.

6.4.3 Spin orbit coupling

As the linearised superconducting gap equation is sensitive to the exact topology of the Fermi surface, we must take into account all the features required to provide a quantitatively accurate Fermi surface. Specifically, we must include additional spin-indices introduced by the presence of spin-orbit coupling. For this reason we have to slightly modify the pairing vertex of Eq. (6.4) to also include the pseudospin bands generated by the spin orbit interaction.

The pairing vertex in the band basis for a singlet state takes the form presented in Ref. [91],

$$\Gamma^{SOC}_{\mu\nu}(\mathbf{k},\mathbf{k}') = \left[\Gamma^{\Uparrow\Downarrow\Uparrow\Downarrow}_{\mu\nu}(\mathbf{k},\mathbf{k}') - \Gamma^{\Uparrow\Downarrow\Downarrow\Uparrow}_{\mu\nu}(\mathbf{k},\mathbf{k}')\right]. \tag{6.16}$$

where

$$\Gamma^{\Sigma\bar{\Sigma}\Lambda\bar{\Lambda}}_{\mu\nu}(\mathbf{k},\mathbf{k}') = \sum_{stpq}\sum_{\sigma\bar{\sigma}\lambda\bar{\lambda}} a^{t\sigma *}_{\mu\Sigma}(\mathbf{k}) a^{s\bar{\sigma}*}_{\mu\bar{\Sigma}}(-\mathbf{k}) \mathrm{Re}[\Gamma^{pq;\lambda\bar{\lambda}}_{st;\sigma\bar{\sigma}}(\mathbf{k},\mathbf{k}')] a^{p\bar{\lambda}}_{\nu\bar{\Lambda}}(-\mathbf{k}') a^{q\lambda}_{\nu\Lambda}(\mathbf{k}'). \tag{6.17}$$

Here, $a^{t\sigma}_{\mu\Sigma}(\mathbf{k})$ is the eigenvector of the original Hamiltonian, in the presence of spin orbit coupling, which connects the orbital and spin basis (s,p,q,t and σ,λ) with the band and pseudospin-band basis (μ,ν and Σ,Λ).
The pairing vertex in orbital space is then defined as

$$\Gamma^{pq;\lambda\bar{\lambda}}_{st;\sigma\bar{\sigma}}(\mathbf{k},\mathbf{k}') = V^{c}_{pq;st}\delta_{\sigma\lambda}\delta_{\bar{\sigma}\bar{\lambda}} + V^{s}_{pq;st}\tilde{\sigma}_{\sigma\lambda}\tilde{\sigma}_{\bar{\sigma}\bar{\lambda}}. \tag{6.18}$$

Here, $\tilde{\sigma}_{\sigma\lambda}$ is a vector of Pauli matrices and $\delta_{\sigma\lambda}$ defines the Kronecker delta function. By performing the spin sum over these Pauli matrices, we obtain a pairing vertex of the form

$$\Gamma^{pq;\lambda\bar{\lambda}}_{st;\sigma\bar{\sigma}}(\mathbf{k},\mathbf{k}')] = \begin{cases} V^{c}_{pq;st} + V^{s}_{pq;st}, & \sigma=\lambda=\bar{\sigma}=\bar{\lambda} \\ V^{c}_{pq;st} - V^{s}_{pq;st}, & \sigma=\lambda\neq\bar{\sigma}=\bar{\lambda} \\ 2V^{s}_{pq;st}, & \sigma=\bar{\lambda}\neq\lambda=\bar{\sigma} \\ 0, & otherwise. \end{cases} \tag{6.19}$$

Here, $V^{c/s} = \frac{1}{2}U^{c/s}\chi^{c/s}U^{c/s}$. The Coulomb matrix $U^{c/s}$, and spin susceptibility $\chi^{c/s}$,

are the same as Eq. (6.5) and (6.6). We calculate χ_0 without the inclusion of spin orbit coupling as it has been shown that this quantity will only strongly affect the susceptibility when very close to a magnetic instability [91].

6.4.4 Tight binding model and orbital content

Here we use the unfolded 1-Fe unit cell of FeSe, which, in the $k_z = 0$ plane, is exactly equivalent to the folded 2-Fe unit cell [143]. We use this model, firstly, to simplify the computational cost of the calculation and secondly, to separate the two electron pockets in momentum space. This provides a method to easily generate a “one electron pocket" Fermi surface from the conventional “two electron pocket" tight binding model. To perform the unfolding procedure we write the Hamiltonian as

$$H^{1Fe}(\mathbf{k}) = H^{AA}(\mathbf{k}) + H^{AB}(\mathbf{k}). \tag{6.20}$$

Here, $H^{AA}(\mathbf{k})$ and $H^{AB}(\mathbf{k})$ are 5x5 block matrices, which are defined in Section 3.2.

This 1-Fe Hamiltonian now has a Brillouin zone twice as large as the 2-Fe unit cell Hamiltonian used in the previous chapters. The important high symmetry points for FeSe are, the Γ pocket, the electron pocket along the k_x axis, which we will refer to as the X pocket, and the electron pocket pointing along the k_y axis, which we will refer to as the Y pocket. These are located at $(k_x, k_y) = (0,0)$, $(\pi, 0)$ and $(0, \pi)$ respectively.

When compared to the 2-Fe unit cell models, used in the Chapter 5, the “one electron pocket model" is equivalent to a Fermi surface where the Y pocket is neglected, whereas the “two electron pocket model" is a model with eh Y pocket included.

In Fig. 6.7(a), we present the calculated Fermi surface for the hole states at $k_z = 0$. Here, the colour describes the maximum orbital character of the band. In Fig. 6.7(b) we then present the corresponding orbital character as a function of angle around the centre of the pocket, taken counter clockwise from the horizontal axis. The model describes a hole pocket which is predominantly composed of d_{xz} weight. It also captures a weaker component of d_{yz} weight which reaches a maximum value of 16.5% along the minor axis of the ellipse (0°). This reduces to around 8% along the major axis of the ellipse (90°), in agreement with our numerical analysis in Sec. 6.2.1. The X electron pocket, described in Fig. 6.7(c) and (d) has nearly 100% d_{yz} weight along the sides of the peanut shape, which is quickly suppressed and replaced with d_{xy} weight at the tips. However, a smaller 10% contribution of d_{xz} and d_{yz} weight is also present. Finally, in Fig. 6.7(e) and (f) the Y electron pocket is shown. This pocket is equivalent to a 90°

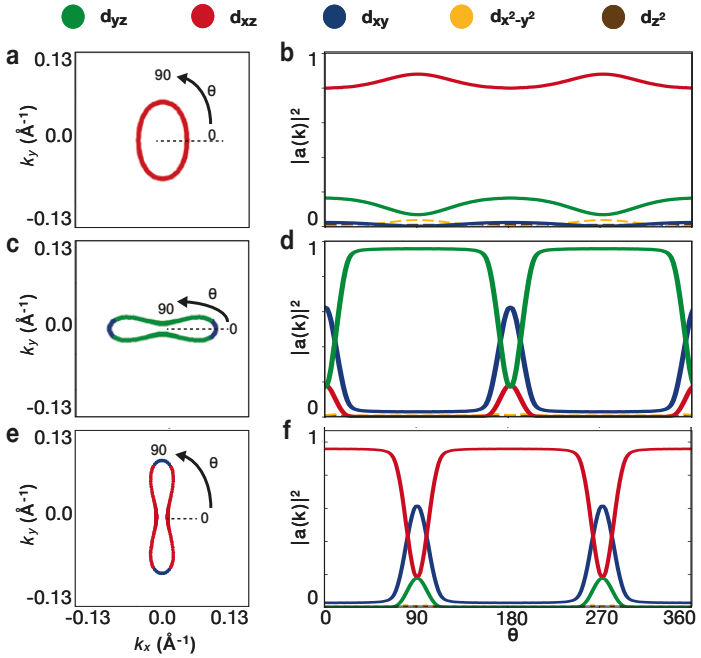

Figure 6.7: Tight binding description of the 1-Fe unit cell of the nematic phase of FeSe at $k_z = 0$. a) Close up of the hole pocket centred at $\mathbf{k} = (0,0)$. b) Orbital content of the pocket as a function of angle. c,d) Equivalent close up of the X electron pocket centred at $\mathbf{k} = (\pi,0)$ and orbital content. e,f) Equivalent close up of the Y electron pocket centred at $\mathbf{k} = (0,\pi)$ and orbital content. The angular dispersion is taken counter clockwise with 0 positioned parallel to the k_x axis, as labelled in the figures. The colour of the band describes the maximum orbital content as labelled at the top of the figure.

rotated X pocket, with the d_{yz} and d_{xz} orbital content swapped.

6.4.5 Results

We now present the results of the solution to the eigenvalue equation from Eq. (6.15) using the pairing vertex described in Eq. (6.16).

In Fig. 6.8 we present the leading eigenvalue obtained from the solution to Eq. (6.15). Although we have determined that the Y electron pocket is not present in the nematic phase of FeSe [163], the Y electron pocket is predicted to exist in ab-initio modelling and tight binding descriptions of the *Cmma* lattice. For this reason, we begin by presenting the solution of Eq. (6.15) assuming a Fermi surface composed of a hole pocket and two electron pockets, as shown in Fig. 6.8(a). The leading eigenvalue of this model is presented in Fig. 6.8(c). Here, the red curve describes the magnitude of the superconducting gap at the hole pocket, which is suggested to be much smaller than

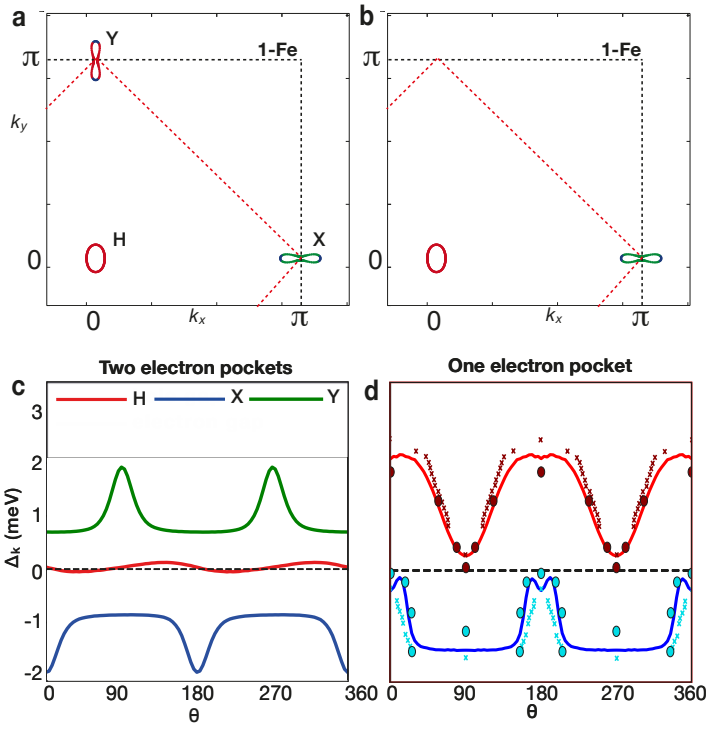

Figure 6.8: a) Fermi surface map of nematic FeSe in the 1-Fe unit cell including a hole pocket (H) and two electron pockets (X and Y). The black dashed line describes the 1-Fe unit cell Brillouin zone boundary, and the red dashed line defines the 2-Fe unit cell equivalent. b) Fermi surface map of nematic FeSe where the Y electron pocket has been removed. c) Momentum dependence of the superconducting gap calculated using the Fermi surface of (a). The convention of the angular dispersion is the same as in Fig. 6.7. Here, the green curve describes the gap at the Y electron pocket, the red curve describes the gap at the hole pocket, and the blue curve describes the gap at the X electron pocket. d) Equivalent calculation using the Fermi surface in (b). Here, the red and blue circles describe the experimental gap magnitude obtained in Section 6.2. The red and blue crosses are the corresponding gap results obtained from BQPI experiments [157].

the magnitude of the gap at either electron pocket, and consist of nodes. The X and Y electron pockets present a similar momentum dependence of the gap with opposite sign and offset by 90°. The maximum gap here is predicted to be observed at the tips of the electron pocket. This calculation does not reproduce the experimental results of Section 6.3.

By taking into account the observations of ARPES studies on detwinned FeSe [163] and removing the contribution of the Y electron pocket from the superconducting pairing, as shown in Fig. 6.8(b), we obtain a completely different momentum dependence of the superconducting gap. In Fig. 6.8(d) we present the calculated momentum

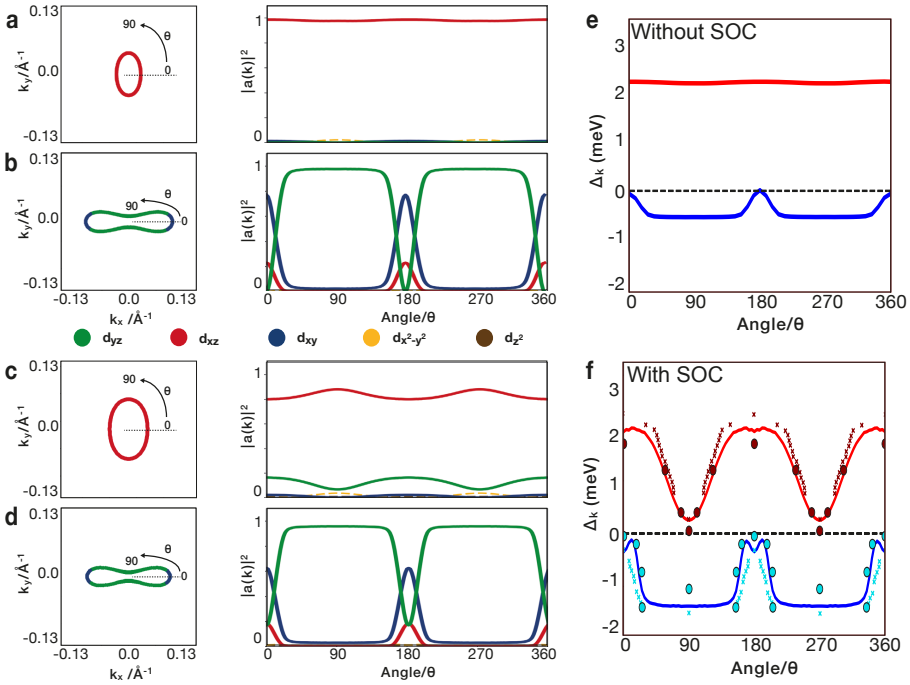

Figure 6.9: a,b) Fermi surface and orbital character of the nematic phase of FeSe without spin orbit coupling. c,d) Fermi surface and orbital character of the nematic phase of FeSe with spin orbit coupling. e) Calculated momentum dependence of the superconducting gap without spin orbit coupling. f) Calculated momentum dependence of the superconducting gap with spin orbit coupling. In (a-d) the colours correspond to the orbital content as labelled in the Figure. In (e-f) red describes the gap at the hole pocket, blue describes the gap at the electron pocket.

dependence. Here, the hole pocket is predicted to be very anisotropic, with the largest gap along the minor axis of the ellipse, and a very small gap along the major axis of the ellipse. The electron pocket, is predicted to have a maximum gap along the length of the peanut shaped pocket, which rapidly tends to zero (but remains nodeless) at the tips. This is in direct agreement with our experimental results, and the results obtained from BQPI experiments by Sprau *et. al.* [157]. These experimental results have been overlaid on top of the calculated result in Fig. 6.8(d). To facilitate comparison with experiment, we have scaled the calculated results by a single constant, such that the maximum normalised gap has the same magnitude as the experimental results. The relative magnitude of the gap at the hole and electron pocket have not been altered by the scaling parameter.

Finally, to illustrate that the momentum dependence of the superconducting gap scales with the d_{yz} orbital weight, we solve Eq. (6.15) using the pairing vertex from

Eq. (6.4), where spin orbit coupling has been set to zero. Again, we assume that the Y pocket is not present. In Fig. 6.9(a) and (b) it can be seen that this only has a minor effect on the shape and symmetry of the Fermi surface, with a slight reduction in the size of the hole pocket. However, without spin orbit coupling, the hole pocket is composed of 100% d_{xz} weight. By solving Eq. (6.15) using this model, we find that the hole pocket gap is expected to be totally isotropic, and much larger than the electron pocket. The equivalent model and gap calculation with spin orbit coupling are presented again for comparison in Fig. 6.9(c-f).

This calculation demonstrates the orbitally-differential nature of spin-fluctuation mediated superconductivity. The inclusion of a minor contribution of d_{yz} states at the hole pocket provides a pathway for $(\pi, 0)$ spin-fluctuations to pair two fermions with the same orbital character. This interaction will be much larger than both the pairing between different orbital characters separated by $(\pi, 0)$, or the same orbital characters separated by a small $\mathbf{q}$ vector. As a result, the d_{yz} states will dominate the momentum dependence of the superconducting gap.

6.4.6 Calculated superconducting gap structure of $FeSe_{1-x}S_x$

The results from section 6.4.5 suggest that the “one electron pocket" Fermi surface directly influences the momentum dependence of the superconducting gap. We now ask the question, how will the gap structure evolve as the strength of nematicity is decreased? Experimentally, It is possible to tune the strength of nematicity in FeSe by substituting Se atoms with sulphur. Sulphur is isoelectronic to selenium, but has a smaller atomic radius. Sulphur substitution therefore does not dope the electronic states of FeSe but instead only applies effective chemical pressure to the lattice, which consequentially suppresses the nematic state [176]. Above a critical doping of $x \approx 0.18$, nematicity is completely suppressed and the tetragonal electronic structure measured in FeSe at 100 K is recovered [186]. This has little impact on the the superconducting transition temperature [198].

We can model the $FeSe_{1-x}S_x$ system using the tight binding model of FeSe. By reducing the strength of our nematic order parameter Δ_{nem}, we have an effective parameter which mimics the suppression of nematic ordering. In Fig. 6.10, the Fermi surface and orbital characters of the tight binding model in the $k_z = 0$ plane are presented for the tetragonal phase ($\Delta_{nem} = 0$). The hole pocket, presented in Fig. 6.10(a) and (b), now describe a C_4 symmetric state with equivalent contribution of d_{xz} and d_{yz} orbital weight. The X and Y electron pockets (Fig. 6.10(c)-(f)) describe bands with

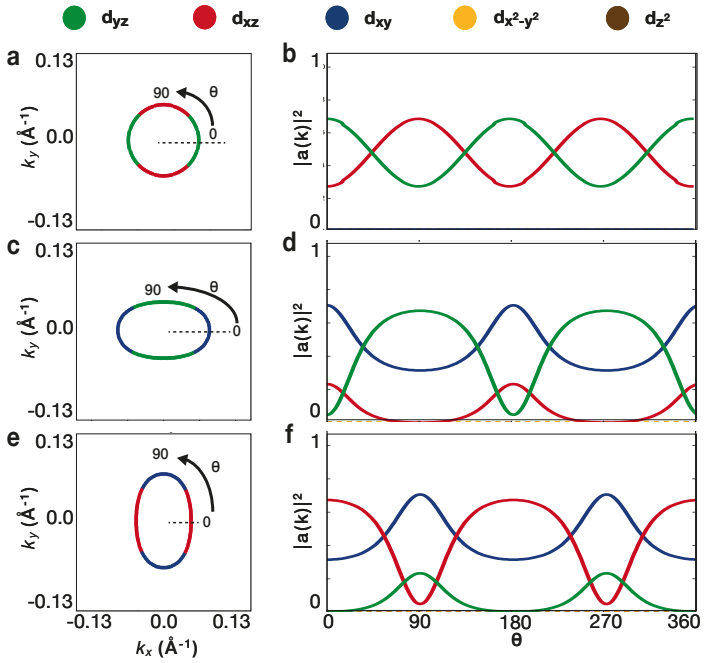

Figure 6.10: Tight binding description of the 1-Fe unit cell of the tetragonal phase of FeSe at $k_z = 0$. a) Close up of the hole pocket centred at $\mathbf{k} = (0,0)$. b) Orbital content of the pocket as a function of angle. c,d) Equivalent close up of the X electron pocket centred at $\mathbf{k} = (\pi,0)$ and orbital content. e,f) Equivalent close up of the Y electron pocket centred at $\mathbf{k} = (0,\pi)$ and orbital content. The angular dispersion is taken counter clockwise with 0 positioned parallel to the k_x axis, as described in the figures. The colour of the state describe the maximum orbital content labelled at the top of the figure.

mixed orbital characters. By increasing Δ_{nem}, we smoothly evolve the orbital content of Fig. 6.10 to the full nematic state of Fig. 6.7.

In Fig 6.11 we present the results of these calculations as a function of Δ_{nem}. We begin by assuming that the Y electron pocket does not contribute in any of the sulphur substituted systems (6.11(a)-(d)). Fig. 6.11(a) reproduces the calculation of undoped FeSe, as presented in Fig. 6.8, which is in agreement with the experimentally observed gap structure [95]. As sulphur substitution increases, nematicity is suppressed. The gap at the X electron pocket becomes larger than the gap at the hole pocket. This prediction does not necessarily imply that the absolute magnitude of the gap will increase, only that the ratio between the two will shift in favour of the electron pocket. These calculations also suggest the presence of an accidental node at the tip of the electron pocket as nematicity is reduced.

This prediction of a decrease to the magnitude of the gap at the hole pocket, com-

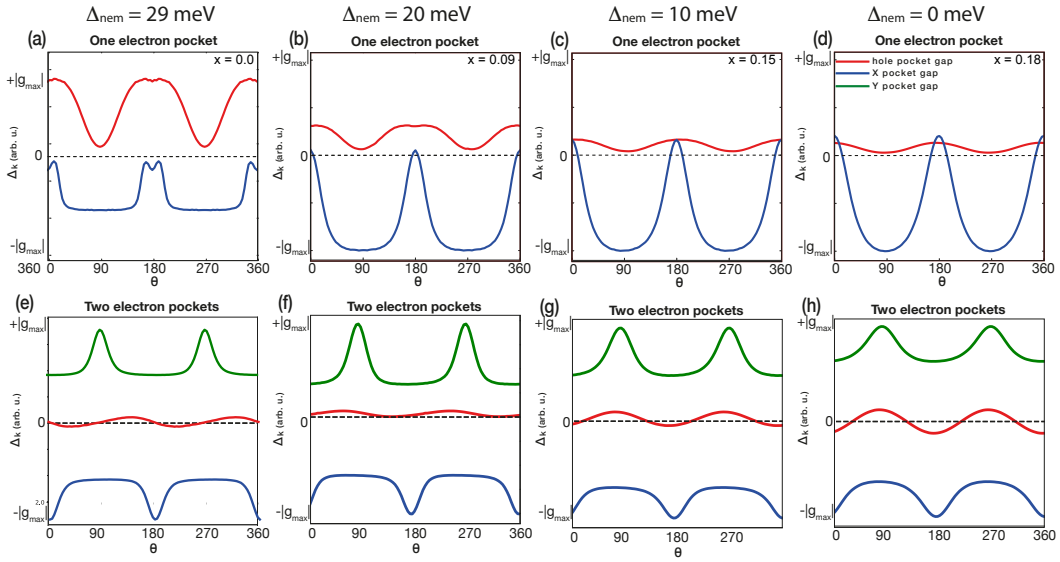

Figure 6.11: Calculated momentum dependence of the superconducting gap for sulphur doped FeSe. a-d) Assuming that the Y pocket is not present, and for nematic strengths of $\Delta_{nem} = 29$ meV, 20 meV, 10 meV and 0 meV. e-h) Equivalent calculations assuming the Y electron pocket is present.

pared to the gap at the electron pocket, is consistent with the general description of multiband pairing. In a multiband system, the ratio of the gap on the two pockets is proportional to the inverse ratio of the density of states [199],

$$\frac{\Delta_h}{\Delta_e} = \frac{\sqrt{N_e}}{\sqrt{N_h}}. \tag{6.21}$$

Here, $\Delta_{e/h}$ describes the gap at the electron and hole pocket respectively, and $N_{e/h}$ describes the density of states. If we assume that these quantities are dominated by the d_{yz} orbital character, as would be the case in the spin-fluctuation scenario, then a smaller density of d_{yz} states on the hole band will lead to a larger magnitude of the superconducting gap at the same state. However, as nematicity is suppressed, the d_{yz} orbital weight at the hole pocket increases, as shown in Fig. 6.10. This increase in N_h then decreases the relative ratio of the gap at the hole pocket, compared to the electron pocket.

If at any point the Y electron pocket is present in the sulphur doped systems, a dramatic change to the momentum dependence of the gap structure is predicted to occur. This is shown in Fig. 6.11(e)-(h). The gap at the electron pocket is predicted to become much larger than the gap at the hole pocket and have a maximum gap at the tips of the electron pocket. Conversely, the gap at the hole pocket is predicted to

become much smaller and exhibit nodes. For a tetragonal sample, where two electron pockets should be observed [186], our calculations suggest a d-wave type gap, with nodes at the hole pocket.

Looking at the momentum dependence of the gaps closely, it appears that the gap at the electron pockets follow the d_{xy} orbital character in a two electron pocket scenario. This implies that (π,π) scattering between the d_{xy} electron states dominate the calculation. We note that the RPA approximation is known to overestimate the spin susceptibility at $\mathbf{q} = (\pi,\pi)$ [146], which is in contrast to inelastic neutron scattering experiments, which observe a peak at $(\pi,0)$ and $(0,\pi)$[3] [115]. Thus, the RPA pairing vertex may be artificially overestimating the interaction between these states. Whilst theoretical efforts to go beyond the RPA approximation have been attempted [182], the calculations are much more computationally expensive and beyond the scope of this thesis.

Currently, the superconducting gap of sulphur doped FeSe has not been measured, thus comparisons with experiment are not possible at this moment in time. The one exception is the momentum dependence of the hole pocket measured by Xu *et. al.* for 7% sulphur doped FeSe [193] which corresponds to $\Delta_{nem} = 23$ meV. Here, the symmetry of the gap at the hole pocket is in agreement with the theoretical calculations of Fig. 6.11(b), assuming that the Y electron pocket is not present, however the electron pocket gap was not resolved.

6.5 Discussion

There has been a general consensus, within the theoretical literature, that spin fluctuations must be an important ingredient when it comes to superconductivity in the iron-based superconductors [13, 80, 89, 94, 200, 201]. However, direct experimental evidence is still challenging to obtain. In this chapter, we have presented two pieces of evidence supporting the spin-fluctuation pairing scenario in FeSe. Firstly, we have experimentally determined that the magnitude of the superconducting gap directly scales with the orbital content of the band. Secondly, we have shown that once we take into account all of the fine details of the electron structure of FeSe, such as spin orbit coupling and band shifts associated with nematic ordering, the highly anisotropic momentum dependence of the superconducting gap, measured in our ARPES experiment,

[3] So far, neutron scattering has only been performed on twinned crystals of FeSe, so the difference between $(\pi,0)$ and $(0,\pi)$ has not yet been established.

is directly reproduced on the assumption of a spin fluctuation pairing scenario.

Importantly, this theoretical result would not have been obtained without previous experimental evidence to suggest that the Fermi surface of FeSe only consists of one hole pocket and one electron pocket [163]. Conventional theories of the electronic structure of FeSe suggest that the Fermi surface should be composed of one hole pocket and two electron pockets. However, as discussed in Chapter 4, detwinned ARPES studies do not observe this. We have also found that the experimental QPI data does not show any evidence for a Fermi surface composed of one hole pocket and two electron pockets. Whilst the origin of this partial reconstruction of the electronic structure is still not known, by taking this experimental phenomenology seriously of ARPES and QPI seriously, we can naturally account for the unusual anisotropic response in the superconducting state. This provides further evidence supporting the “one electron pocket" description of FeSe.

Several other theories have been put forward to describe the anisotropic gap distribution measured in FeSe. Sprau *et. al.* [157] and Kreisel *et. al.* [78] have suggested a theory that the electronic structure of FeSe is sufficiently renormalised by orbitally selective quasiparticle weights. Specifically, they introduce a tight binding model of FeSe which is modified by quasiparticle weights to satisfy the criteria $Z_{xy} < Z_{xz} << Z_{yz}$. This assumption dramatically reduces the coherence of the d_{xz} ($Z_{xz} = 0.16$) and d_{xy} ($Z_{xy} = 0.073$) states, such that the gap only follows the remaining d_{yz} ($Z_{yz} = 0.85$) states. However, whilst this theory correctly reproduces the measured gap structure, the assumptions required to obtain this agreement would also have a direct impact on the single particle spectral function measured by ARPES. In this chapter we have presented a detailed study on the orbital content of the bands of FeSe, and observe all three d_{xz}, d_{yz} and d_{xy} orbital characters, with roughly equal intensity and sharpness. therefore, this assumption, of a large difference in quasiparticle weights between different orbitals, does not agree with experimental ARPES measurements. We note however, that the Y electron pocket, which we explicitly remove in our calculations, is composed entirely of d_{xz} and d_{xy} weight at the Fermi level (Fig. 6.7(e)). The chosen quasiparticle values used in Ref. [157] and [78] have the additional consequence of suppressing the contribution of the Y electron pocket to the superconducting pairing. This is consistent with the conclusion drawn here.

Benfatto *et. al.* [181] have proposed a scenario where the spin fluctuations themselves generate an anisotropic preference in the X or Y direction, which they claim could originate from the induction of nematicity [180]. Benfatto *et. al.* found that

the required anisotropy in the spin fluctuations along the X or Y direction had to be at least $\frac{g_X}{g_Y} = 21$, where g is the directional coupling parameter, to match the experimental results. This suggests that coupling between the hole pocket and Y electron pocket is effectively negligible compared to coupling between the hole and X electron pocket. Again, this theoretical assumption has the consequence of removing the contribution of the Y electron pocket from superconducting pairing, which is in agreement with our conclusions.

Kang *et. al.* [170], using a simplified tight binding model, proposed that nematicity alone may account for the observed anisotropy at the hole pocket. However, in this approach, the orbital character at the hole pocket does not match the experimental observations determined in this chapter. The hole pocket used consists of 100% d_{yz} weight along the minor axis of the ellipse, compared to the 18.5% determined experimentally. This theoretical approach also suggests a unique momentum dependence of the superconducting gap at the Y pocket, such that experimental measurements should observe three separate superconducting gaps. So far this has not been observed within ARPES [95, 196] or BQPI [157].

Finally, Hu *et. al.* [183] used a self consistent slave-spin model to determine the quasiparticle weights of the d_{xz}, d_{yz} and d_{xy} orbitals as suggested from a DFT-based tight binding model. Here, they obtain similar values for the quasiparticle weights to those suggested by the experiment of Sprau *et. al.* [157] and Kreisel *et. al.* [78], and equivalently, the calculation of the momentum dependence of the superconducting gap reproduces the experimental result. However, the DFT-based tight binding model, used as a starting point for their calculations, describes a system with an additional d_{xy} hole pocket at the Fermi surface, which may have influenced the slave-spin calculation. The values of the quasiparticle weights chosen would one more produce a noticeable difference in the ARPES data of FeSe, which we have not observed. Again, the quasiparticle weight values determined in this work would have the consequence of suppressing the Y electron pocket from contributing to the superconducting pairing.

In each of these theoretical attempts to model the superconducting gap of FeSe, spin fluctuation mediated superconductivity has been assumed. Each approach has found that the gap structure in a multi-orbital system will follow the orbital content that dominates the superconducting pairing. Thus, the conclusion that superconductivity in FeSe is mediated by spin fluctuations appears to be unanimously accepted. The discrepancies lie in determining the origin of the dramatic anisotropy of the gap. Refs [78, 157, 181, 183] have all proposed modifications to either the electronic structure

or pairing vertex which greatly reduces the contribution of the Y electron pocket to superconducting scattering. We propose that the simplest explanation, which does not require phenomenological quasiparticle weights or coupling parameters, is simply that the Y electron pocket is not present in the nematic phase. And that the Fermi surface consists of only one hole pocket and one electron pocket. This “one electron pocket" description of FeSe is in agreement with ARPES data on detwinned crystals [163], QPI experiments [158, 159] and can reproduce the momentum dependence of the superconducting gap. We stress that the origin of this reconstruction of the electronic structure within the nematic state is still unknown. However, this may be a key feature of nematicity, which could allow us to understand both superconductivity and the microscopic mechanism of nematicity in FeSe.

6.6 Conclusion

One of the major challenges in our attempts to understand unconventional superconductivity is uncovering the underlying mechanism which controls T_c. In this chapter, we have studied the momentum dependence of the superconducting gap of FeSe. We have observed a large anisotropy of the gap at both the hole and electron pockets, which follows the d_{yz} orbital character of the band, as suggested by a spin-fluctuation pairing mechanism of superconductivity.

We have further supported this observation, by performing theoretical calculations, using the understanding of the electronic structure of FeSe, developed throughout the course of this thesis. We find that the experimental gap structure and the theoretical gap structure are in direct agreement, when a “one electron pocket" model description of the electronic structure of FeSe is used. This result shows a direct consequence of nematicity on the superconducting gap structure, and provides strong evidence in favour of spin-fluctuation mediated superconductivity in FeSe.

7 | Conclusion

In this thesis I have attempted to understand the superconducting mechanism of FeSe.

In Chapter 3, a set of ARPES-based hopping parameters for a tight binding model of FeSe was developed. These parameters were able to quantitatively describe the electronic structure of the tetragonal phase of FeSe at 100 K. Using this model, a strong temperature dependence of the chemical potential was predicted to occur. This was then confirmed via a temperature dependent ARPES study [144]. This result highlighted the importance of capturing the low temperature electronic structure from a quantitatively accurate model of FeSe.

In Chapter 4, this tight binding model was updated to account for the C_4 symmetry breaking effects of the nematic state of FeSe. A phenomenological nematic order parameter was developed which could quantitatively reproduce the band shifts observed in ARPES studies of twinned sample of FeSe. By studying detwinned crystals of FeSe, an entirely expected result was uncovered. Whilst theoretical models suggest that the Fermi surface of FeSe should consist of one hole pocket and two electron pockets, only of the two electron pockets were detected within the nematic state [163]. This disappearance could not be explained by band shifts of splittings alone and is potentially a more fundamental feature of nematicity. We also observed a similar phenomenon in detwinned studies of NaFeAs [173].

In Chapter 5, additional evidence was found for a Fermi surface of the nematic state which only consisted of one hole pocket and one electron pocket within the QPI experiments of FeSe. By comparing the experimental data of Hanaguri *et. al.* [158] with theoretical calculations, assuming either a “two electron pocket" or “one electron pocket" tight binding model, it was found that the “one electron pocket" tight binding model was in much better agreement with the experimental data of FeSe. The importance of finitie k_z states within QPI measurements were also highlighted.

Whilst the discovery of a Fermi surface consisting of one hole pocket and only one electron pocket was unexpected, this observation provides a possible justification for

the large anisotropic responses observed in the nematic phase of iron-based superconductors [72]. However, it's microscopic origin remains unclear and requires further study.

Finally, In Chapter 6, the superconducting state of FeSe was studied [95]. A two-fold highly anisotropic momentum dependence of the superconducting gap was observed at both the hole and electron pockets and in three dimensions. It was observed that the magnitude of the superconducting gap appeared to scale with the d_{yz} orbital character of the band. This suggested that the pairing mechanism for superconductivity in FeSe was sensitive to the orbital content of the underlying band structure.

Using the tight binding model developed in the previous chapters, the momentum dependence of the superconducting gap was calculated assuming superconductivity was mediated by spin fluctuations. It was found that when the correct "one-electron pocket" Fermi surface of FeSe was used, the theoretical calculation directly reproduced the experimental results.

This thesis provides a detailed study of the electronic structure of bulk FeSe. It presents an argument to suggest that whilst the Fermi surface of the nematic phase is predicted to consist of one hole pocket and two electron pockets, experimentally only one hole pocket and one electron pocket are observed. This thesis also presents strong experimental and theoretical evidence in favour of a spin fluctuation mediated pairing mechanism for superconductivity in FeSe.

7.1 Future work

One of the key conclusions from this thesis is that the Fermi surface of FeSe consists of only one hole pocket and one electron pocket. Whereas theoretical calculations suggested that two electron pockets should be present. The tetragonal state of FeSe at 100 K does exhibit a Fermi surface with two electron pockets, thus it would be informative to perform a temperature dependent study of this pocket as the system evolves through the nematic transition.

Detwinned ARPES studies on other nematic iron-based superconductors such as $BaFe_2As_2$, will also need to be performed to determine if the "one electron pocket" Fermi surface is a generic feature of the nematic phase or a phenomenon specific to FeSe and NaFeAs.

Regarding superconductivity, it would be interesting to study the sulphur doped phase diagram of FeSe. Sulphur doping has the effect of suppressing the nematic state,

whilst only weakly affecting the superconducting transition temperature. Beyond the nematic critical point of 18% sulphur doping, the low temperature electronic structure appears almost equivalent to the tetragonal electronic structure of FeSe at 100 K, and two electron pockets are measured in ARPES [186]. The model devised in Chapter 3, along with the nematic order parameter devised in Chapter 4, is able to describe the experimental band dispersions of the sulphur doped system of FeSe. It would also be interesting to experimentally measure the superconducting gap of the sulphur doped systems, to compare with the theoretical calculations we have made in section 6.4.6.

It would also be informative to calculate the QPI images of the Sulphur doped FeSe systems and compare with experimental literature. Beyond 18% sulphur doping, scattering vectors from the second electron pocket should be present. It would be informative to determine which value of sulphur doping shows evidence for the second electron pocket.

A | Tight binding model

In this section we describe the tight binding model, first introduced by Eschrig and Koepernik [142], and used throughout this thesis. Following the notion of Ref. [142], we label the hopping parameters as $t^{xyz}_{\alpha\beta}$ where x, y and z describe the number of Fe-atoms a fermion has hopped in the x, y or z direction and α,β describe the initial and final orbital character for the overlap integral. For 2D hoppings the z label is neglected for simplicity. Finally, the orbitals are labelled as $[1: d^A_{xy}, 2: d^A_{x^2-y^2}, 3: id^A_{xz}, 4: id^A_{yz}, 5: d^A_{z^2}, 6: d^B_{xy}, 7: d^B_{x^2-y^2}, 8: -id^B_{xz}, 9: -id^B_{yz}, 10: d^B_{z^2}]$ where the A and B notation relates to the first or second Fe atom, this is labelled as $+$ and $-$ in the notation of Ref. [142]. The sign change for the imaginary d_{xz} and d_{yz} orbitals is a matter of convention to take into account the glide symmetry of the $P4/nmm$ lattice [142, 143].

The full 10x10 matrix can be written as 5x5 block matrices,

$$H(\mathbf{k}) = \begin{pmatrix} H^{AA}(\mathbf{k}) & H^{AB}(\mathbf{k}) \\ H^{AB}(\mathbf{k})^* & H^{AA}(\mathbf{k})^* \end{pmatrix}, \tag{A.1}$$

And the two Bloch matrices, H^{AA} and H^{AB} take the form: [142, 146]

$$\begin{aligned} H^{AA}_{11} = \;& \varepsilon_1 + 2t^{11}_{11}\Big[cos(k_1)+\cos(k_2)\Big] + 2t^{20}_{11}\Big[\cos(2k_1)+\cos(2k_2)\Big] \\ & + \Big\{2t^{001}_{11} + 4t^{111}_{11}\Big[\cos(k_1)+\cos(k_2)\Big] + 4t^{201}_{11}\Big[\cos(2k_x)+\cos(2k_y)\Big]\Big\}\cos(k_z) \end{aligned}$$

$$H^{AA}_{12} = 0$$

$$H^{AA}_{13} = \; 2it^{11}_{13}\Big[\sin(k_1)-\sin(k_2)\Big] - 4t^{201}_{14}\sin(2k_y)\sin(k_z)$$

$$H^{AA}_{14} = \; 2it^{11}_{13}\Big[\sin(k_1)+\sin(k_2)\Big] - 4t^{201}_{14}\sin(2k_x)\sin(k_z)$$

$$H^{AA}_{15} = \; 2t^{11}_{15}\Big[\cos(k_1)-\cos(k_2)\Big]$$

$$H_{22}^{AA} = \varepsilon_2 + 2t_{22}^{11}\Big[\cos(k_1)+\cos(k_2)\Big]$$

$$H_{23}^{AA} = 2it_{23}^{11}\Big[\sin(k_1)+\sin(k_2)\Big]$$

$$H_{24}^{AA} = 2it_{23}^{11}\Big[-\sin(k_1)+\sin(k_2)\Big]$$

$$H_{25}^{AA} = 0$$

$$\begin{aligned} H_{33}^{AA} = {} & \varepsilon_3 + 2t_{33}^{11}\Big[\cos(k_1)+\cos(k_2)\Big] + 2t_{33}^{20}\cos(2k_x) \\ & + 2t_{33}^{02}\cos(2k_y) + 4t_{33}^{22}\cos(2k_x)\cos(2k_y) \\ & + \Big\{2t_{33}^{001} + 4t_{33}^{201}\cos(2k_x) + 4t_{33}^{021}\cos(2k_y)\Big\}\cos(k_z) \end{aligned}$$

$$H_{34}^{AA} = 2t_{34}^{11}\Big[\cos(k_1)-\cos(k_2)\Big]$$

$$H_{35}^{AA} = 2it_{35}^{11}\Big[\sin(k_1)+\sin(k_2)\Big]$$

$$\begin{aligned} H_{44}^{AA} = {} & \varepsilon_3 + 2t_{33}^{11}\Big[\cos(k_1)+\cos(k_2)\Big] + 2t_{33}^{02}\cos(2k_x) \\ & + 2t_{33}^{20}\cos(2k_y) + 4t_{33}^{22}\cos(2k_x)\cos(2k_y) \\ & + \Big\{2t_{33}^{001} + 4t_{33}^{021}\cos(2k_x) + 4t_{33}^{201}\cos(2k_y)\Big\}\cos(k_z) \end{aligned}$$

$$H_{45}^{AA} = 2it_{35}^{11}\Big[\sin(k_1)-\sin(k_2)\Big]$$

$$H_{55}^{AA} = \varepsilon_5$$

$$
\begin{aligned}
H_{16}^{AB} = \;& 2t_{16}^{10}\Big[\cos(k_x)+\cos(k_y)\Big] + 2t_{16}^{21}\Big\{\Big[\cos(k_1)+\cos(k_2)\Big]\Big[\cos(k_x)+\cos(k_y)\Big] \\
& -\sin(k_1)\Big[\sin(k_x)+\sin(k_y)\Big]+\sin(k_2)\Big[\sin(k_x)-sin(k_y)\Big]\Big\} \\
& +4t_{16}^{101}\Big[\cos(k_x)+\cos(k_y)\Big]\cos(k_z) \\
& +2t_{16}^{121}\Big\{\Big[\cos(k_1+k_y)+\cos(k_1+k_x)\Big]e^{ik_z}+\Big[\cos(k_2+k_y)+\cos(k_2-k_x)\Big]e^{-ik_z}\Big\}
\end{aligned}
$$

$$
H_{17}^{AB} = 0
$$

$$
\begin{aligned}
H_{18}^{AB} = \;& 2it_{18}^{10}\sin(k_x) - 4\Big\{t_{18}^{101}\sin(k_x)+t_{19}^{101}\sin(k_y)\Big\}\sin(k_z) \\
& +2it_{19}^{121}\Big\{\sin(k_1+k_y)e^{ik_z}-\sin(k_2+k_y)e^{-ik_z}\Big\}
\end{aligned}
$$

$$
\begin{aligned}
H_{19}^{AB} = \;& 2it_{18}^{10}\sin(k_y) - 4\Big\{t_{19}^{101}\sin(k_x)+t_{18}^{101}\sin(k_y)\Big\}\sin(k_z) \\
& +2it_{19}^{121}\Big\{\sin(k_1+k_x)e^{ik_z}+\sin(k_2-k_x)e^{-ik_z}\Big\}
\end{aligned}
$$

$$
H_{1,10}^{AB} = 0
$$

$$
H_{27}^{AB} = \;\; 2t_{27}^{10}\Big[\cos(k_x)+\cos(k_y)\Big]
$$

$$
H_{28}^{AB} = \;\; -2it_{29}^{10}\sin(k_y)
$$

$$
H_{29}^{AB} = \;\; 2it_{29}^{10}\sin(k_x)
$$

$$
H_{2,10}^{AB} = \;\; 2t_{2,10}^{10}\Big[\cos(k_x)-\cos(k_y)\Big]
$$

$$
\begin{aligned}
H_{38}^{AB} = \;& 2t_{38}^{10}\cos(k_x)+2t_{49}^{10}\cos(k_y) \\
& +2t_{38}^{21}\Big\{\Big[\cos(k_1)+\cos(k_2)\Big]\cos(k_x)-\Big[\sin(k_1)-\sin(k_2)\Big]\sin(k_x)\Big\} \\
& +2t_{49}^{21}\Big\{\Big[\cos(k_1)+\cos(k_2)\Big]\cos(k_y)-\Big[\sin(k_1)+\sin(k_2)\Big]\sin(k_y)\Big\} \\
& +4\Big\{t_{38}^{101}\cos(k_x)+t_{49}^{101}\cos(k_y)\Big\}\cos(k_z) \\
& +2t_{38}^{121}\Big\{\cos(k_1+k_x)e^{ik_z}+\cos(k_2-k_x)e^{-ik_z}\Big\} \\
& +2t_{49}^{121}\Big\{\cos(k_1+k_y)e^{ik_z}+\cos(k_2+k_y)e^{-ik_z}\Big\}
\end{aligned}
$$

$$H_{39}^{AB} = \quad 4it_{39}^{101}\Big[\cos(k_x)+\cos(k_y)\Big]\sin(k_z)$$

$$H_{3,10}^{AB} = \quad 2it_{4,10}^{10}\sin(k_y)$$

$$\begin{aligned}
H_{49}^{AB} = \;& 2t_{49}^{10}\cos(k_x)+2t_{38}^{10}\cos(k_y) \\
&+2t_{49}^{21}\Big\{\Big[\cos(k_1)+\cos(k_2)\Big]\cos(k_x)-\Big[\sin(k_1)-\sin(k_2)\Big]\sin(k_x)\Big\} \\
&+2t_{38}^{21}\Big\{\Big[\cos(k_1)+\cos(k_2)\Big]\cos(k_y)-\Big[\sin(k_1)+\sin(k_2)\Big]\sin(k_y)\Big\} \\
&+4\Big\{t_{49}^{101}\cos(k_x)+t_{38}^{101}\cos(k_y)\Big\}\cos(k_z) \\
&+2t_{49}^{121}\Big\{\cos(k_1+k_x)e^{ik_z}+\cos(k_2-k_x)e^{-ik_z}\Big\} \\
&+2t_{38}^{121}\Big\{\cos(k_1+k_y)e^{ik_z}+\cos(k_2+k_y)e^{-ik_z}\Big\}
\end{aligned}$$

$$H_{4,10}^{AB} = 2it_{4,10}^{10}\sin(k_x)$$

$$H_{5,10}^{AB} = 0$$

Here H^{AA} describes a Hermitian matrix such that $H_{ij}^{AA} = H_{ji}^{AA*}$. Whereas the off diagonal matrix, H^{AB}, is symmetric but not Hermitian $H_{ij}^{AB} = H_{ji}^{AB}$. This ensures that the full Hamiltonian of eq. (A.1) is Hermitian, and producing real Eigenvalues. The DFT-based hopping parameters used in chapter 3 are taken from Ref. [142]. The hopping parameters obtained from the optimization procedure outlined in this thesis are presented below, all in units of eV.

2D parameters

$t_{11}^{11} = 0.01818$ $t_{16}^{10} = -0.03133$ $t_{33}^{11} = 0.02433$
$t_{11}^{20} = 0.00093$ $t_{16}^{21} = -0.00231$ $t_{33}^{20} = 0.00096$
$t_{13}^{11} = -0.01226i$ $t_{18}^{10} = 0.11516i$ $t_{33}^{02} = -0.00717$
$t_{15}^{11} = -0.01817$ $t_{27}^{10} = -0.04988$ $t_{33}^{22} = 0.00758$
$t_{22}^{11} = -0.01669$ $t_{29}^{10} = -0.09492i$ $t_{38}^{10} = 0.00868$
$t_{23}^{11} = 0.01484i$ $t_{2,10}^{10} = 0.059659$ $t_{38}^{21} = -0.00493$
$t_{34}^{11} = 0.01650$ $t_{35}^{11} = 0.00569i$ $t_{4,10}^{10} = -0.00902i$
$t_{49}^{10} = 0.05023$ $t_{49}^{21} = -0.00008$
$\varepsilon_1 = 0.03405$ $\varepsilon_2 = -0.05050$ $\varepsilon_3 = 0.00310$
$\varepsilon_4 = 0.00310$ $\varepsilon_5 = -0.19398$

3D parameters

$t_{16}^{101} = 0.00270$ $t_{11}^{001} = 0$ $t_{14}^{201} = 0.00950i$
$t_{16}^{121} = -0.00283$ $t_{11}^{111} = 0$ $t_{19}^{101} = 0.00333i$
$t_{18}^{101} = 0.00150i$ $t_{11}^{201} = 0.00013$ $t_{19}^{121} = 0.00517i$
$t_{33}^{001} = 0.00183$ $t_{38}^{101} = 0.00300$ $t_{49}^{121} = 0.00100.$
$t_{33}^{201} = -0.00133$ $t_{38}^{121} = -0.00050$ $t_{49}^{101} = 0.00217$
$t_{33}^{021} = 0.00333$ $t_{39}^{101} = 0.00250$

Finally, to introduce spin orbit coupling to the Hamiltonian we use the angular momentum matrices discussed in Ref. [91]. We use a spin orbit coupling strength of $\lambda = 19$ meV in Chapters 3,4 and 6. In Chapter 5 we however modify the in-plane spin orbit coupling strength such that $\lambda_z = 19$ meV, and $\lambda_{x/y} = 5$ meV. Here λ_i is applied to the spin orbit matrix l_i.

$$\hat{l}_x = \begin{pmatrix} 0 & 0 & -i & 0 & 0 \\ 0 & 0 & 0 & i & 0 \\ i & 0 & 0 & 0 & 0 \\ 0 & -i & 0 & 0 & -\sqrt{3}i \\ 0 & 0 & 0 & \sqrt{3}i & 0 \end{pmatrix} \tag{A.2}$$

$$\hat{l}_y = \begin{pmatrix} 0 & 0 & 0 & i & 0 \\ 0 & 0 & i & 0 & 0 \\ 0 & -i & 0 & 0 & \sqrt{3}i \\ -i & 0 & 0 & 0 & 0 \\ 0 & 0 & -\sqrt{3}i & & 0 \end{pmatrix} \tag{A.3}$$

$$\hat{l}_z = \begin{pmatrix} 0 & 2i & 0 & 0 & 0 \\ -2i & 0 & 0 & 0 & 0 \\ 0 & 0 & 0 & -i & 0 \\ 0 & 0 & i & 0 & 0 \\ 0 & 0 & 0 & 0 & 0 \end{pmatrix} \tag{A.4}$$

$\hat{l}_x$, $\hat{l}_y$ and $\hat{l}_z$ describe the angular momentum operators in the x,y, and z directions respectively for a single Fe atom where the rows and columns are defined equivalent to the Hamiltonian as $[d_{xy}, d_{x^2-y^2}, d_{xz}, d_{yz}, d_{z^2}]$. As mentioned in the main text, we include spin orbit coupling via

$$\hat{H}_{SOC}(k) = \begin{pmatrix} H(\mathbf{k}) + \hat{L}_z & \hat{L}_x + i\hat{L}_y \\ \hat{L}_x - i\hat{L}_y & H(\mathbf{k}) - \hat{L}_z \end{pmatrix}. \tag{A.5}$$

Where $\hat{L}_i$ is defined as

$$\hat{L}_i = \frac{\lambda_i}{2} \begin{pmatrix} \hat{l}_i & 0 \\ 0 & \hat{l}_i \end{pmatrix}. \tag{A.6}$$

Finally, the nematic order parameter is defined,

$$\frac{\Delta_{nem}}{4}(n'_{yz} - n'_{xz})(\cos(k_x) + cos(k_y)) + \frac{\Delta_{nem}}{2}(n'_{yz} - n'_{xz})(\cos(k_x) - cos(k_y)). \tag{A.7}$$

We use $\Delta_{nem} = 29$ meV for the nematic phase of FeSe. In the notation of the Hamiltonian defined in this section n'_{yz} means add to the matrix element H_{49}^{AB} and n'_{xz} means add to the matrix element H_{38}^{AB}.

B | Derivation of the spin fluctuation pairing vertex

B.1 Non-interacting spin susceptibility

In order to describe superconductivity mediated by spin fluctuations, we must first introduce the dynamic spin susceptibility. In the Matsubara notation of imaginary time, the dynamic spin susceptibility is defined as a Fourier transform of the spin correlation function,

$$\chi_{ps}(\mathbf{q}, i\omega) = \int_0^\beta d\tau \left\langle T_\tau \vec{S}_p(\mathbf{q},\tau)\vec{S}_s(-\mathbf{q},0)\right\rangle e^{i\omega\tau}. \tag{B.1}$$

Here, the dynamic spin susceptibility (χ) depends on the orbital indices, s and p, the momentum, $\mathbf{q}$, and the imaginary Matsubara frequency, $i\omega$. In the Matsubara formalism this integral is periodic in $\beta = \frac{1}{k_b T}$ where T is the temperature. The spin operator is defined as

$$\vec{S}_s(\mathbf{q},\tau) = \frac{1}{2}\sum_{\mathbf{k},\alpha\gamma} c^\dagger_{s\alpha}(\mathbf{k},\tau)\hat{\sigma}_{\alpha\gamma}c_{s\gamma}(\mathbf{k}+\mathbf{q},\tau). \tag{B.2}$$

The sum in Eq. (B.2) is performed over the first Brillouin zone. $c_{s\alpha(\gamma)}(\mathbf{k},\tau)$ is the creation/annihilation operator for a fermion at time τ in orbital s, with momentum $\mathbf{k}$ and spin $\alpha(\gamma)$. Finally $\hat{\sigma}_{\alpha\gamma}$ is a vector of Pauli matrices. By expanding Eq. B.1 using Eq. B.2 the spin susceptibility becomes.

$$\chi_{ps}(\mathbf{q}, i\omega) = \frac{1}{4}\sum_{\mathbf{k},\alpha\gamma}\sum_{\mathbf{k}',\alpha\gamma}\int_0^\beta d\tau \left\langle T_\tau c^\dagger_{p\alpha}(\mathbf{k},\tau)\hat{\sigma}_{\alpha\gamma}c_{p\gamma}(\mathbf{k}+\mathbf{q},\tau)c^\dagger_{s\alpha}(\mathbf{k}',0)\hat{\sigma}_{\alpha\gamma}c_{s\gamma}(\mathbf{k}'-\mathbf{q},0)\right\rangle e^{i\omega\tau}. \tag{B.3}$$

The Pauli matrices can then be summed over using the relation $\sum_{\alpha\gamma}\hat{\sigma}_{\alpha\gamma}\hat{\sigma}_{\alpha\gamma} = 2\delta_{\alpha\gamma}$ to give,

$$\chi_{ps}(\mathbf{q},i\omega) = \sum_{\mathbf{k}}\sum_{\mathbf{k}'}\int_0^\beta d\tau \left\langle T_\tau c^\dagger_{p\alpha}(\mathbf{k},\tau)c_{p\gamma}(\mathbf{k}+\mathbf{q},\tau)c^\dagger_{s\alpha}(\mathbf{k}',0)c_{s\gamma}(\mathbf{k}'-\mathbf{q},0)\right\rangle e^{i\omega\tau}. \tag{B.4}$$

Next, $\mathbf{k}'$ can be redefined as $\mathbf{k}'=\mathbf{k}+\mathbf{q}$ to give,

$$\chi_{ps}(\mathbf{q},i\omega) = \sum_{\mathbf{k}}\int_0^\beta d\tau \left\langle T_\tau c^\dagger_{p\alpha}(\mathbf{k},\tau)c_{p\gamma}(\mathbf{k}+\mathbf{q},\tau)c^\dagger_{s\alpha}(\mathbf{k}+\mathbf{q},0)c_{s\gamma}(\mathbf{k},0)\right\rangle e^{i\omega\tau}. \tag{B.5}$$

We then apply the time ordering operator T, such that we order the creation and annihilation operators with the lowest time on the left hand side, and largest on the right. Here, we also assume that the Hamiltonian of the many body system is time independent. This is denoted by the subscript "0" next to the expectation value, and changes the spin susceptibility of the interacting system, χ_{ps}, into the non-interacting spin susceptibility.

$$\chi^0_{ps}(\mathbf{q},i\omega) = \sum_{\mathbf{k}}\int_0^\beta d\tau \left\langle c^\dagger_s(\mathbf{k},0)c_s(\mathbf{k+q},0)c^\dagger_p(\mathbf{k+q},\tau)c_p(\mathbf{k},\tau)\right\rangle_0 e^{i\omega\tau}. \tag{B.6}$$

From Wicks theorem, we note that this is simply the product of two non interacting Green's functions,

$$\chi^0_{ps}(\mathbf{q},i\omega) = -\sum_{\mathbf{k}}\int_0^\beta d\tau\ \ G^0_{ps}(\mathbf{k+q},\tau)G^0_{sp}(\mathbf{k},-\tau)e^{i\omega\tau}. \tag{B.7}$$

We can then Fourier transform the Green's function into a Frequency space via,

$$G^0(\mathbf{k},\tau) = \sum_n G^0(\mathbf{k},i\omega_n)e^{-i\omega_n\tau}. \tag{B.8}$$

Applying eq (B.8) to (B.7) and manipulating we obtain

$$\begin{aligned}
\chi^0_{ps}(\mathbf{q},i\omega) &= -\sum_{\mathbf{k}}\int_0^\beta d\tau e^{i\omega\tau}G^0_{ps}(\mathbf{k+q},\tau)\sum_n G^0_{sp}(\mathbf{k},i\omega_n)e^{i\omega_n\tau},\\
\chi^0_{ps}(\mathbf{q},i\omega) &= -\sum_{\mathbf{k}}\int_0^\beta d\tau \sum_n e^{i(\omega+\omega_n)\tau}G^0_{ps}(\mathbf{k+q},\tau)G^0_{sp}(\mathbf{k},i\omega_n),
\end{aligned} \tag{B.9}$$

$$\chi^0_{ps}(\mathbf{q}, i\omega) = -\sum_{\mathbf{k}}\sum_{n} G^0_{ps}(\mathbf{k+q}, i\omega + i\omega_n) G^0_{sp}(\mathbf{k}, i\omega_n). \tag{B.10}$$

Here, the non-interacting Matsubara Green's function in orbital space is defined

$$G^0_{sp}(\mathbf{k}, i\omega_n) = \sum_{\mu} \frac{a^s_\mu(\mathbf{k}) a^{p*}_\mu(\mathbf{k})}{i\omega_n - E_\mu(\mathbf{k})}. \tag{B.11}$$

Here, $a^s_\mu(\mathbf{k})$ corresponds to the eigenvector connecting the orbital space (s) and diagonal band space (μ), from the tight-binding Hamiltonian, and $E_\mu(\mathbf{k})$ is the energy of the band μ at momentum $\mathbf{k}$. Using the Feynman notation, Eq. 6.7 can be expressed as an electron-hole bubble diagram.

$\chi^0_{pq;st}(\mathbf{q}, i\omega_m) =$ 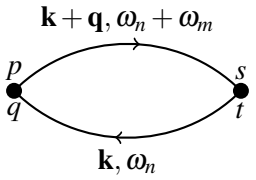

Here the curved lines connecting the two vertices are mathematically equivalent to a Green's function of Eq. B.11. This defines the non-interacting spin susceptibility.

B.2 Random phase approximation

To describe the physics of fluctuating spins we must go beyond the non-interacting spin susceptibility of Eq. (B.10) and include interaction terms which govern the magnetic properties of the system. To do this we include a vertex correction to the non-interacting spin susceptibility, shown diagrammatically on the left hand side of Fig. B.1,

$$\chi^{int} = \Gamma\chi^0. \tag{B.12}$$

Here χ^{int} is the dressed, or interacting spin susceptibility, χ^0 is the non-interacting susceptibility of Eq. (B.10) and Γ is the interacting vertex correction. For the random phase approximation, we define the vertex as the sum of the bubble and ladder diagrams

$$\Gamma = \Gamma_0 + \Gamma\chi^0 U_1 + \Gamma\chi^0 U_2. \tag{B.13}$$

This is shown diagrammatically in Fig. B.1. Here U_1 and U_2 are interaction terms

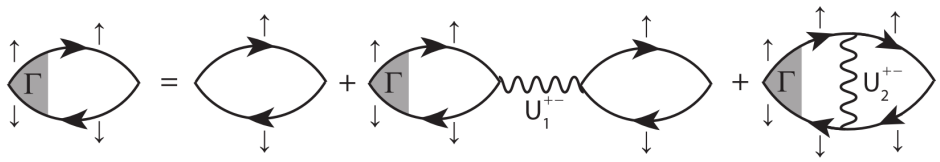

Figure B.1: The three diagrams of the first order perturbative expansion of the spin susceptibility. Figure taken from Ref. [203].

related to the Coulomb repulsion, shown as wavey lines in Fig. B.1. Within the random phase approximation, $\Gamma_0 = 1$. We therefore neglect any contributions beyond the first order of this perturbative expansion, such as the Maki-Thompson or Aslamasov-Larkin second order perturbations [202]. This was shown by Migdal [58] to be a valid approximation assuming that $\frac{\omega}{E_F} << 1$, where ω defines the maximum spin fluctuation energy, and E_F is the Fermi energy of the system.

If we define $U = U_1 + U_2$ then $\Gamma = [1 - \chi^0 U]^{-1}$. We can therefore write the interacting RPA spin susceptibility as

$$\chi^{RPA} = \chi^0 [1 - U\chi^0]^{-1}. \tag{B.14}$$

Which allows us to study spin fluctuations and magnetic instabilities as a function of the interaction variable U.

B.3 Pairing vertex using the FLEX approximation

To describe superconductivity, we must account for an interaction term which can couple two fermions. Mathematically, we can write this equation as a particle-particle pairing vertex. In Chapter 6 we use this vertex to deduce the leading symmetry and momentum dependence of the superconducting gap. In this thesis, we are assuming that the pairing mechanism is spin-singlet, and mediated by fluctuating spins, interacting via electronic interactions.

The fluctuation-exchange approximation (FLEX), originally developed by Bickers and Scalapino [197] is the simplest infinite-order approximation that takes into account both spin and charge fluctuations. This is useful in the description of the properties of materials where magnetism plays a dominant role.

We can construct the analytical form of the FLEX approximation in a single band system by summing up all bubble and ladder diagrams. In Fig. B.2, the first two terms

of the singlet bubble diagrams (Top row) and first two terms of the singlet ladder diagram (bottom row) are shown. Here each solid line refers to a non-interacting Green's function, G_0, with a spin given by the up or down arrow. The dashed lines refer to the interaction between the Green's functions, which in this case is the Coulomb repulsion U.

To determine the form of the pairing vertex, Γ, which is distinct from the vertex used in the RPA approximation, we multiply together all Green's functions and interaction lines present in the Feynman diagrams of Fig. B.2. That is the interaction parameters U with any intermediate Green's functions. We neglect the initial Green's functions (with momentum $\mathbf{k}$ and $-\mathbf{k}$) and final Green's functions (with momentum $\mathbf{k}'$ and $-\mathbf{k}'$). An additional rule of this formulation states that for every intermediate Green's function we must introduce a sum over the entire Brillouin zone, to account for all possible scattering pathways.

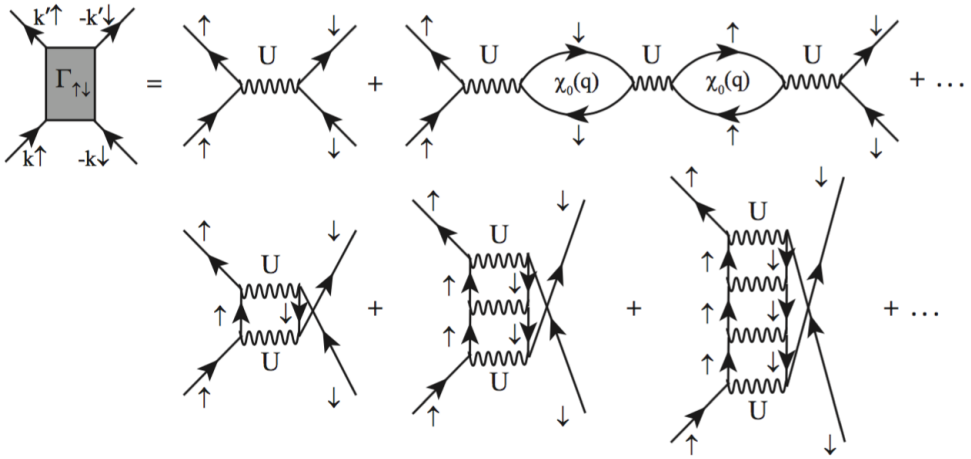

Figure B.2: Pairing vertex in the FLEX approximation. Top row: the first two terms of the infinite series of bubble diagrams. Bottom row: the first three terms of the ladder diagram series. Figure taken from Ref. [203].

The analytical form of the first two terms of the bubble diagram (top row) can then be written as

$$U + \sum_{\mathbf{p}} \sum_{\mathbf{p}'} U G^0_{\downarrow}(\mathbf{p}+\mathbf{q}) G^0_{\downarrow}(\mathbf{p}) U G^0_{\uparrow}(\mathbf{p}'+\mathbf{q}) G^0_{\uparrow}(\mathbf{p}') U + ... \tag{B.15}$$

Here, by using the relationship defined in Eq. 6.7, we notice that the additional summation over the intermediate momenta $\mathbf{p}$ is equivalent to the non-interacting susceptibility. This relationship also holds for higher order terms, such that the infinite series for the bubble diagrams can be written as

$$U + U^3\chi^0(\mathbf{q})^2 + U^5\chi^0(\mathbf{q})^4 + U^7\chi^0(\mathbf{q})^6 + U^9\chi^0(\mathbf{q})^8 + ... \tag{B.16}$$

$$U[1 + U^2\chi^0(\mathbf{q})^2 + U^4\chi^0(\mathbf{q})^4 + U^6\chi^0(\mathbf{q})^6 + U^8\chi^0(\mathbf{q})^8 + ...] \tag{B.17}$$

$$U[1 - U^2\chi^0(\mathbf{q})^2]^{-1}. \tag{B.18}$$

Likewise the ladder diagrams can be summed in a similar way:

$$\begin{aligned} &= \sum_{\mathbf{p}} UG^0_{\uparrow}(\mathbf{p}+\mathbf{q})G^0_{\downarrow}(\mathbf{p})U \\ &+ \sum_{\mathbf{p}}\sum_{\mathbf{p}'} UG^0_{\downarrow}(\mathbf{p}+\mathbf{q})G^0_{\downarrow}(\mathbf{p})UG^0_{\uparrow}(\mathbf{p}'+\mathbf{q})G^0_{\uparrow}(\mathbf{p}')U \\ &+ \sum_{\mathbf{p}}\sum_{\mathbf{p}'}\sum_{\mathbf{p}''} UG^0_{\downarrow}(\mathbf{p}+\mathbf{q})G^0_{\downarrow}(\mathbf{p})UG^0_{\uparrow}(\mathbf{p}'+\mathbf{q})G^0_{\uparrow}(\mathbf{p}')UG^0_{\downarrow}(\mathbf{p}''+\mathbf{q})G^0_{\downarrow}(\mathbf{p}'')U + ... \end{aligned} \tag{B.19}$$

$$U^2\chi^0(\mathbf{q}) + U^3\chi^0(\mathbf{q})^2 + U^4\chi^0(\mathbf{q})^3 + U^5\chi^0(\mathbf{q})^4 + U^6\chi^0(\mathbf{q})^5 + ... \tag{B.20}$$

$$U^2\chi^0(\mathbf{q})[1 + U\chi^0(\mathbf{q}) + U^2\chi^0(\mathbf{q})^2 + U^3\chi^0(\mathbf{q})^3 + U^4\chi^0(\mathbf{q})^4 + ...] \tag{B.21}$$

$$U^2\chi^0(\mathbf{q})[1 - U\chi^0(\mathbf{q})]^{-1}. \tag{B.22}$$

We can then re-express these summations in the charge and spin channel,

$$U[1 - U^2\chi^0(\mathbf{q})^2]^{-1} + U^2\chi^0(\mathbf{q})[1 - U\chi^0(\mathbf{q})]^{-1} = A\chi^S(\mathbf{q}) + B\chi^C(\mathbf{q}) + C. \tag{B.23}$$

Here, the interacting spin susceptibility is defined,

$$\chi^S(\mathbf{q}) = \chi^0(\mathbf{q})[1 - U\chi^0(\mathbf{q})]^{-1}, \tag{B.24}$$

$$\chi^C(\mathbf{q}) = \chi^0(\mathbf{q})[1 + U\chi^0(\mathbf{q})]^{-1}. \tag{B.25}$$

By solving Eq. B.23, the single band pairing vertex may be defined as

$$\Gamma(\mathbf{k},\mathbf{k}') = \frac{3}{2}U^2\chi^S(\mathbf{k}-\mathbf{k}') - \frac{1}{2}U^2\chi^C(\mathbf{k}-\mathbf{k}') + U. \tag{B.26}$$

This can then be generalised to multi-orbital systems as discussed in Sec. 6.4.1.

Bibliography

[1] H.-W. Lee, K.-C. Kim and J. Lee, *IEEE Transactions on Magnetics*, 2006, **42**, 1917–1925.

[2] P. Pugnat and A. Siemko, *IEEE Transactions on Applied Superconductivity*, 2007, **17**, 1091–1096.

[3] R. W. Darbeau, *Appl. Spectrosc. Rev.*, 2006, **41**, 401–425.

[4] J. Minervini, M. Parizh and M. Schippers, *Supercond. Sci. Technol.*, 2018, **31**, 030301.

[5] D. Drung, C. Abmann, J. Beyer, A. Kirste, M. Peters, F. Ruede and T. Schurig, *IEEE Transactions on Applied Superconductivity*, 2007, **17**, 699–704.

[6] P. Moreau, A. Le-Luyer, P. Spuig, P. Malard, F. Saint-Laurent, J. F. Artaud, J. Morales, B. Faugeras, H. Heumann, B. Cantone, M. Moreau, C. Brun, R. Nouailletas, E. Nardon, B. Santraine, A. Berne, P. Kumari and S. Belsare, *Review of Scientific Instruments*, 2018, **89**, 10J109.

[7] M. H. Devoret and R. J. Schoelkopf, *Science*, 2013, **339**, 1169–1174.

[8] W. Buckles and W. V. Hassenzahl, *IEEE Power Eng. Rev.*, 2000, **20**, 16–20.

[9] S. Forner and B. Schwartz, *Superconductor Materials Science: Metallurgy, Fabrication, and Applications*, Springer US, Boston, MA, 1981, pp. 133–199.

[10] A. Ballarino and R. Flükiger, *J. Phys. Conf. Ser.*, 2017, **871**, 12098.

[11] V. L. Ginzburg, *Journal of Superconductivity*, 2000, **13**, 665–677.

[12] I. I. Mazin, *Nature*, 2010, **464**, 183.

[13] P. J. Hirschfeld, M. M. Korshunov and I. I. Mazin, *Reports on Progress in Physics*, 2011, **74**, 124508.

[14] L. N. Cooper, *Phys. Rev.*, 1956, **104**, 1189–1190.

[15] J. Bardeen, L. N. Cooper and J. R. Schrieffer, *Phys. Rev.*, 1957, **108**, 1175–1204.

[16] H. K. Onnes, *KNAW Proc.*, 1911, 113–115.

[17] W. Meissner and R. Ochsenfeld, *Naturwissenschaften*, 1933, **21**, 787–788.

[18] F. London and H. London, *Proc. Roy. Soc. London.*, 1935, **149**, 71.

[19] M. Tinkham, *Introduction to Superconductivity*, Dover, 2nd edn., 1996, p. 17.

[20] J. Bardeen, *Phys. Rev.*, 1955, **97**, 1724–1725.

[21] C. A. Reynolds, B. Serin, W. H. Wright and L. B. Nesbitt, *Phys. Rev.*, 1950, **78**, 487.

[22] H. Fröhlich, *Phys. Rev.*, 1950, **79**, 845–856.

[23] B. Mitrović, H. G. Zarate and J. P. Carbotte, *Phys. Rev. B*, 1984, **29**, 184–190.

[24] W. Ashcroft, *Phys. Rev. Lett.*, 1968, **21**, 1748–1749.

[25] A. P. Drozdov, M. I. Eremets, I. A. Troyan, V. Ksenofontov and S. I. Shylin, *Nature*, 2015, **525**, 73–76.

[26] A. P. Drozdov, V. S. Minkov, S. P. Besedin, P. P. Kong, M. A. Kuzovnikov, D. A. Knyazev and M. I. Eremets, *arXiv:1808.07039v1*, 2018.

[27] M. Somayazulu, M. Ahart, A. K. Mishra, Z. M. Geballe, M. Baldini, Y. Meng, V. V. Struzhkin and R. J. Hemley, *Phys. Rev. Lett.*, 2019, **122**, 027001.

[28] N. W. Ashcroft, *Phys. Rev. Lett.*, 2004, **92**, 187002.

[29] F. Steglich, J. Aarts, C. D. Bredl, W. Lieke, D. Meschede, W. Franz and H. Schäfer, *Phys. Rev. Lett.*, 1979, **43**, 1892–1896.

[30] K. Miyake, S. Schmitt-Rink and C. M. Varma, *Phys. Rev. B*, 1986, **34**, 6554–6556.

[31] J. Bednorz and K. Muller, *Zeitschrift für Phys. B Condens. Matter*, 1986, **64**, 189–193.

[32] P. A. Lee, N. Nagaosa and X.-G. Wen, *Rev. Mod. Phys.*, 2006, **78**, 17–85.

[33] G.-I. Oya and E. J. Saur, *Journal of Low Temperature Physics*, 1979, **34**, 569–583.

[34] C. W. Chu, P. H. Hor, R. L. Meng, L. Gao, Z. J. Huang, Wang and Y. Q, *Phys. Rev. Lett.*, 1987, **58**, 405–407.

[35] M. K. Wu, J. R. Ashburn, C. J. Torng, P. H. Hor, R. L. Meng, L. Gao, Z. J. Huang, Y. Q. Wang and C. W. Chu, *Phys. Rev. Lett.*, 1987, **58**, 908–910.

[36] A. Schilling, M. Cantoni, J. D. Guo and H. R. Ott, *Nature*, 1993, **363**, 56–58.

[37] L. Gao, Y. Y. Xue, F. Chen, Q. Xiong, R. L. Meng, D. Ramirez, C. W. Chu, J. H. Eggert and H. K. Mao, *Phys. Rev. B*, 1994, **50**, 4260–4263.

[38] M. A. Malik and B. A. Malik, *Am. J. Condens. Matter Phys.*, 2012, **2**, 67–72.

[39] B. Batlogg, R. J. Cava, A. Jayaraman, R. B. van Dover, G. A. Kourouklis, S. Sunshine, D. W. Murphy, L. W. Rupp, H. S. Chen, A. White, K. T. Short, A. M. Mujsce and E. A. Rietman, *Phys. Rev. Lett.*, 1987, **58**, 2333–2336.

[40] L. C. Bourne, M. F. Crommie, A. Zettl, H.-C. Z. Loye, S. W. Keller, K. L. Leary, A. M. Stacy, K. J. Chang, M. L. Cohen and D. E. Morris, *Phys. Rev. Lett.*, 1987, **58**, 2337–2339.

[41] G.-M. Zhao, H. Keller and K. Conder, *Journal of Physics: Condensed Matter*, 2001, **13**, R569.

[42] Z. Schlesinger, R. T. Collins, D. L. Kaiser and F. Holtzberg, *Phys. Rev. Lett.*, 1987, **59**, 1958–1961.

[43] Z.-X. Shen, D. S. Dessau, B. O. Wells, D. M. King, W. E. Spicer, A. J. Arko, D. Marshall, L. W. Lombardo, A. Kapitulnik, P. Dickinson, S. Doniach, J. DiCarlo, T. Loeser and C. H. Park, *Phys. Rev. Lett.*, 1993, **70**, 1553–1556.

[44] H. Ding and M. Norman, *Phys. Rev. B - Condens. Matter Mater. Phys.*, 1996, **54**, R9678–R9681.

[45] L. Taillefer, *Annual Review of Condensed Matter Physics*, 2010, **1**, 51–70.

[46] T. Timusk and B. W. Statt, *Rep. Prog. Phys.*, 1999, **61**, 54.

[47] A. A. Kordyuk, *Low Temp. Phys.*, 2015, **41**, 319–341.

[48] G. Ghiringhelli, M. Le Tacon, M. Minola, S. Blanco-Canosa, C. Mazzoli, N. B. Brookes, G. M. De Luca, A. Frano, D. G. Hawthorn, F. He, T. Loew, M. M. Sala, D. C. Peets, M. Salluzzo, E. Schierle, R. Sutarto, G. A. Sawatzky, E. Weschke, B. Keimer and L. Braicovich, *Science*, 2012, **337**, 821–825.

[49] M. J. Lawler, K. Fujita, J. Lee, A. R. Schmidt, Y. Kohsaka, C. K. Kim, H. Eisaki, S. Uchida, J. C. Davis, J. P. Sethna and E.-A. Kim, *Nature*, 2010, **466**, 347.

[50] J. Bok and J. Bouvier, *Int. J. Mod. Phys. B*, 1999, **13**, 3425–3430.

[51] P. W. Anderson, *Science*, 1987, **235**, 1196–1198.

[52] D. J. Scalapino, E. Loh and J. E. Hirsch, *Phys. Rev. B*, 1986, **34**, 8190–8192.

[53] T. Moriya and A. Kawabata, *J. Phys. Soc. Japan*, 1973, **34**, 639–651.

[54] A. J. Millis, H. Monien and D. Pines, *Phys. Rev. B*, 1990, **42**, 167–178.

[55] T. Moriya, Y. Takahashi and K. Ueda, *J. Phys. Soc. Japan*, 1990, **59**, 2905–2915.

[56] T. Moriya and K. Ueda, *Adv. Phys.*, 2000, **49**, 555–606.

[57] H. Kontani, K. Kanki and K. Ueda, *Phys. Rev. B*, 1999, **59**, 19.

[58] A. B. Migdal, *JETP*, 1958, **34**, 996–1001.

[59] D. J. Scalapino, *Phys. Rep.*, 1995, **250**, 329–365.

[60] T. Moriya, *Proc. Jpn. Acad. Ser. B. Phys. Biol. Sci.*, 2006, **82**, 1–16.

[61] Y. Kamihara, T. Watanabe, M. Hirano and H. Hosono, *J. Am. Chem. Soc.*, 2008, **130**, 3296–7.

[62] G. Wu, Y. L. Xie, H. Chen, M. Zhong, R. H. Liu, B. C. Shi, Q. J. Li, X. F. Wang, T. Wu, Y. J. Yan, J. J. Ying and X. H. Chen, *Journal of Physics: Condensed Matter*, 2009, **21**, 142203.

[63] S. He, J. He, W. Zhang, L. Zhao, D. Liu, X. Liu, D. Mou, Y.-B. Ou, Q.-Y. Wang, Z. Li, L. Wang, Y. Peng, Y. Liu, C. Chen, L. Yu, G. Liu, X. Dong, J. Zhang, C. Chen, Z. Xu, X. Chen, X. Ma, Q. Xue and X. J. Zhou, *Nat. Mater.*, 2013, **12**, 605.

[64] S. Tan, Y. Zhang, M. Xia, Z. Ye, F. Chen, X. Xie, R. Peng, D. Xu, Q. Fan, H. Xu, J. Jiang, T. Zhang, X. Lai, T. Xiang, J. Hu, B. Xie and D. Feng, *Nat. Mater.*, 2013, **12**, 634.

[65] J. J. Lee, F. T. Schmitt, R. G. Moore, S. Johnston, Y.-T. Cui, W. Li, M. Yi, Z. K. Liu, M. Hashimoto, Y. Zhang, D. H. Lu, T. P. Devereaux, D.-H. Lee and Z.-X. Shen, *Nature*, 2014, **515**, 245.

[66] J.-F. Ge, Z.-L. Liu, C. Liu, C.-l. Gao, D. Qian, Q.-k. Xue, Y. Liu and J.-F. Jia, *Nat. Mater.*, 2014, **14**, 10.

[67] D. Huang and J. E. Hoffman, *Annu. Rev. Condens. Matter Phys.*, 2017, **8**, 311–336.

[68] A. A. Kordyuk, *Low Temp. Phys.*, 2012, **38**, 888–899.

[69] R. M. Fernandes and J. Schmalian, *Superconductor Science and Technology*, 2012, **25**, 084005.

[70] M. Yi, D. Lu, J.-H. Chu, J. G. Analytis, A. P. Sorini, A. F. Kemper, B. Moritz, S.-K. Mo, R. G. Moore, M. Hashimoto, W.-S. Lee, Z. Hussain, T. P. Devereaux, I. R. Fisher and Z.-X. Shen, *Proceedings of the National Academy of Sciences*, 2011, **108**, 6878–6883.

[71] C. Mirri, A. Dusza, S. Bastelberger, J.-H. Chu, H.-H. Kuo, I. R. Fisher and L. Degiorgi, *Phys. Rev. B*, 2014, **90**, 155125.

[72] A. E. Böhmer and A. Kreisel, *Journal of Physics: Condensed Matter*, 2018, **30**, 023001.

[73] R. M. Fernandes, A. V. Chubukov and J. Schmalian, *Nat. Phys.*, 2014, **10**, 97–104.

[74] M. J. Pitcher, D. R. Parker, P. Adamson, S. J. C. Herkelrath, A. T. Boothroyd, R. M. Ibberson, M. Brunelli and S. J. Clarke, *Chem. Commun.*, 2008, 5918–5920.

[75] A. E. Böhmer, F. Hardy, F. Eilers, D. Ernst, P. Adelmann, P. Schweiss, T. Wolf and C. Meingast, *Phys. Rev. B*, 2013, **87**, 180505(R).

[76] Y. Wang, A. Kreisel, V. B. Zabolotnyy, S. V. Borisenko, B. Büchner, T. A. Maier, P. J. Hirschfeld and D. J. Scalapino, *Phys. Rev. B*, 2013, **88**, 174516.

[77] S. V. Borisenko, V. B. Zabolotnyy, A. A. Kordyuk, D. V. Evtushinsky, T. K. Kim, I. V. Morozov, R. Follath and B. Büchner, *Symmetry*, 2012, **4**, 251–264.

[78] A. Kreisel, B. M. Andersen, P. O. Sprau, A. Kostin and P. J. Hirschfeld, *Phys. Rev. B*, 2017, **95**, 174504.

[79] S. V. Borisenko, V. B. Zabolotnyy, D. V. Evtushinsky, T. K. Kim, I. V. Morozov, A. N. Yaresko, A. A. Kordyuk, G. Behr, A. Vasiliev, R. Follath and B. Büchner, *Phys. Rev. Lett.*, 2010, **105**, 67002.

[80] I. I. Mazin, D. J. Singh, M. D. Johannes and M. H. Du, *Phys. Rev. Lett.*, 2008, **101**, 057003.

[81] I. A. Nekrasov, Z. V. Pchelkina and M. V. Sadovskii, *JETP Lett.*, 2008, **88**, 543–545.

[82] A. Lankau, K. Koepernik, S. Borisenko, V. Zabolotnyy, B. Büchner, J. van den Brink and H. Eschrig, *Phys. Rev. B*, 2010, **82**, 184518.

[83] T. Hajiri, T. Ito, R. Niwa, M. Matsunami, B. H. Min, Y. S. Kwon and S. Kimura, *Phys. Rev. B*, 2012, **85**, 94509.

[84] Z. P. Yin, K. Haule and G. Kotliar, *Nat. Mater.*, 2011, **10**, 932–935.

[85] J. Ferber, K. Foyevtsova, R. Valentí and H. O. Jeschke, *Phys. Rev. B*, 2012, **85**, 94505.

[86] G. Lee, H. S. Ji, Y. Kim, C. Kim, K. Haule, G. Kotliar, B. Lee, S. Khim, K. H. Kim, K. S. Kim, K.-S. Kim and J. H. Shim, *Phys. Rev. Lett.*, 2012, **109**, 177001.

[87] J. M. Tomczak, M. van Schilfgaarde and G. Kotliar, *Phys. Rev. Lett.*, 2012, **109**, 237010.

[88] J. M. Tomczak, *Journal of Physics: Conference Series*, 2015, **592**, 012055.

[89] S. Graser, T. A. Maier, P. J. Hirschfeld and D. J. Scalapino, *New J. Phys.*, 2009, **11**, 025016.

[90] S. V. Borisenko, D. V. Evtushinsky, Z.-H. Liu, I. Morozov, R. Kappenberger, S. Wurmehl, B. Buchner, A. N. Yaresko, T. K. Kim, M. Hoesch, T. Wolf and N. D. Zhigadlo, *Nat. Phys.*, 2016, **12**, 311–317.

[91] T. Saito, Y. Yamakawa, S. Onari and H. Kontani, *Phys. Rev. B*, 2015, **92**, 134522.

[92] D. Altenfeld, P. J. Hirschfeld, I. I. Mazin and I. Eremin, *Phys. Rev. B*, 2018, **97**, 54519.

[93] S. Chi, W. N. Hardy, R. Liang and P. Dosanjh, *arXiv: 1710.09089*, 2018.

[94] H. Kontani and S. Onari, *Phys. Rev. Lett.*, 2010, **104**, 157001.

[95] L. C. Rhodes, M. D. Watson, A. A. Haghighirad, D. V. Evtushinsky, M. Eschrig and T. K. Kim, *Phys. Rev. B*, 2018, **98**, 180503.

[96] A. I. Coldea and M. D. Watson, *Annual Review of Condensed Matter Physics*, 2018, **9**, 125–146.

[97] J. P. Sun, K. Matsuura, G. Z. Ye, Y. Mizukami, M. Shimozawa, K. Matsubayashi, M. Yamashita, T. Watashige, S. Kasahara, Y. Matsuda, J. Q. Yan, B. C. Sales, Y. Uwatoko, J. G. Cheng and T. Shibauchi, *Nat. Comm.*, 2016, **7**, 12146.

[98] S. Kasahara, T. Watashige, T. Hanaguri, Y. Kohsaka, T. Yamashita, Y. Shimoyama, Y. Mizukami, R. Endo, H. Ikeda, K. Aoyama, T. Terashima, S. Uji, T. Wolf, H. von Löhneysen, T. Shibauchi and Y. Matsuda, *Proceedings of the National Academy of Sciences*, 2014, **111**, 16309–16313.

[99] S. Margadonna, Y. Takabayashi, M. McDonald, K. Kasperkiewicz, Y. Mizuguchi, Y. Takano, A. Fitch, E. Suard and K. Prassides, *Chem. Commun.*, 2008, **4**, 5607–5609.

[100] M. D. Watson, T. K. Kim, A. A. Haghighirad, N. R. Davies, A. McCollam, A. Narayanan, S. F. Blake, Y. L. Chen, S. Ghannadzadeh, A. J. Schofield, M. Hoesch, C. Meingast, T. Wolf and A. I. Coldea, *Phys. Rev. B*, 2015, **91**, 155106.

[101] M. D. Watson, S. Backes, A. A. Haghighirad, M. Hoesch, T. K. Kim, A. I. Coldea and R. Valentí, *Phys. Rev. B*, 2017, **95**, 081106.

[102] M. D. Watson, T. K. Kim, L. C. Rhodes, M. Eschrig, M. Hoesch, A. A. Haghighirad and A. I. Coldea, *Phys. Rev. B*, 2016, **94**, 201107.

[103] F.-C. Hsu, J.-Y. Luo, K.-W. Yeh, T.-K. Chen, T.-W. Huang, P. M. Wu, Y.-C. Lee, Y.-L. Huang, Y.-Y. Chu, D.-C. Yan and M.-K. Wu, *Proceedings of the National Academy of Sciences*, 2008, **105**, 14262–14264.

[104] M. Wu, F. Hsu, K. Yeh, T. Huang, J. Luo, M. Wang, H. Chang, T. Chen, S. Rao, B. Mok, C. Chen, Y. Huang, C. Ke, P. Wu, A. Chang, C. Wu and T. Perng, *Physica C: Superconductivity*, 2009, **469**, 340 – 349.

[105] Y. Mizuguchi and Y. Takano, *Journal of the Physical Society of Japan*, 2010, **79**, 102001.

[106] D. J. Singh, *Science and Technology of Advanced Materials*, 2012, **13**, 054304.

[107] L. Malavasi and S. Margadonna, *Chem. Soc. Rev.*, 2012, **41**, 3897–3911.

[108] S. Medvedev, T. M. McQueen, I. A. Troyan, T. Palasyuk, M. I. Eremets, R. J. Cava, S. Naghavi, F. Casper, V. Ksenofontov, G. Wortmann and C. Felser, *Nat. Mater.*, 2009, **8**, 630–633.

[109] M. Burrard-Lucas, D. G. Free, S. J. Sedlmaier, J. D. Wright, S. J. Cassidy, Y. Hara, A. J. Corkett, T. Lancaster, P. J. Baker, S. J. Blundell and S. J. Clarke, *Nat. Mater.*, 2012, **12**, 15.

[110] J. Guo, S. Jin, G. Wang, S. Wang, K. Zhu, T. Zhou, M. He and X. Chen, *Phys. Rev. B*, 2010, **82**, 180520.

[111] T. P. Ying, X. L. Chen, G. Wang, S. F. Jin, T. T. Zhou, X. F. Lai, H. Zhang and W. Y. Wang, *Sci. Rep.*, 2012, **2**, 426.

[112] M. V. Sadovskii, *Physics-Uspekhi*, 2016, **59**, 947–967.

[113] Z. Wang, C. Liu, Y. Liu and J. Wang, *Journal of Physics: Condensed Matter*, 2017, **29**, 153001.

[114] M. A. Tanatar, A. E. Böhmer, E. I. Timmons, M. Schütt, G. Drachuck, V. Taufour, K. Kothapalli, A. Kreyssig, S. L. Bud'ko, P. C. Canfield, R. M. Fernandes and R. Prozorov, *Phys. Rev. Lett.*, 2016, **117**, 127001.

[115] Q. Wang, Y. Shen, B. Pan, Y. Hao, M. Ma, F. Zhou, P. Ste, K. Schmalzl, T. R. Forrest and D. a. Chareev, *Nat. Mater.*, 2015, **15**, 159–164.

[116] Q. Wang, Y. Shen, B. Pan, X. Zhang, K. Ikeuchi, K. Iida, A. D. Christianson, H. C. Walker, D. T. Adroja, M. Abdel-Hafiez, X. Chen, D. A. Chareev, A. N. Vasiliev and J. Zhao, *Nat. Commun.*, 2016, **7**, 12182.

[117] J. Maletz, V. B. Zabolotnyy, D. V. Evtushinsky, S. Thirupathaiah, A. U. B. Wolter, L. Harnagea, A. N. Yaresko, A. N. Vasiliev, D. A. Chareev, A. E. Böhmer, F. Hardy, T. Wolf, C. Meingast, E. D. L. Rienks, B. Büchner and S. V. Borisenko, *Phys. Rev. B*, 2014, **89**, 220506.

[118] K. Nakayama, Y. Miyata, G. N. Phan, T. Sato, Y. Tanabe, T. Urata, K. Tanigaki and T. Takahashi, *Phys. Rev. Lett.*, 2014, **113**, 237001.

[119] T. Shimojima, Y. Suzuki, T. Sonobe, A. Nakamura, M. Sakano, J. Omachi, K. Yoshioka, M. Kuwata-Gonokami, K. Ono, H. Kumigashira, A. E. Böhmer, F. Hardy, T. Wolf, C. Meingast, H. V. Löhneysen, H. Ikeda and K. Ishizaka, *Phys. Rev. B*, 2014, **90**, 121111(R).

[120] P. Zhang, T. Qian, P. Richard, X. P. Wang, H. Miao, B. Q. Lv, B. B. Fu, T. Wolf, C. Meingast, X. X. Wu, Z. Q. Wang, J. P. Hu and H. Ding, *Phys. Rev. B - Condens. Matter Mater. Phys.*, 2015, **91**, 214503.

[121] P. Coleman, in *Introd. to Many-Body Phys.*, Cambridge University Press, 2015, ch. 3, pp. 42–93.

[122] G. D. Mahan, *Many-Particle Physics*, Plenum Publishers, 3rd edn., 2000, pp. 11–26.

[123] J. C. Slater, *Phys. Rev.*, 1929, **34**, 1293–1322.

[124] V. Fock, *Z. Phys.*, 1932, **75**, 622–647.

[125] J. C. Slater and G. F. Koster, *Phys. Rev.*, 1954, **94**, 1498–1524.

[126] A. Damascelli, *Physica Scripta.*, 2004, **T109**, 61–74.

[127] H. Hertz, *Ann. Phys.*, 1887, **267**, 983–1000.

[128] A. Einstein, *Ann. Phys.*, 1906, **325**, 199–206.

[129] M. Planck, *Verhandl. Dtsch. Phys. Ges.*, 1900, **2**, 237.

[130] G. D. Mahan, *Phys. Rev. B*, 1970, **2**, 4334–4350.

[131] S. Hüfner, *Photoeletron Spectroscopy Principles and Applications*, Springer, 3rd edn., 2003, pp. 39–51.

[132] K. Nakayama, T. Sato, K. Terashima, H. Matsui, T. Takahashi, M. Kubota, K. Ono, T. Nishizaki, Y. Takahashi and N. Kobayashi, *Phys. Rev. B*, 2007, **75**, 014513.

[133] V. B. Zabolotnyy, S. V. Borisenko, A. A. Kordyuk, D. S. Inosov, A. Koitzsch, J. Geck, J. Fink, M. Knupfer, B. Büchner, S.-L. Drechsler, V. Hinkov, B. Keimer and L. Patthey, *Phys. Rev. B*, 2007, **76**, 024502.

[134] C. Caroli, D. Lederer-Rozenblatt, B. Roulet and D. Saint-James, *Phys. Rev. B*, 1973, **8**, 4552–4569.

[135] P. J. Feibelman and D. E. Easman, *Phys. Rev. B*, 1974, **10**, 4932–4947.

[136] M. Hoesch, T. K. Kim, P. Dudin, H. Wang, S. Scott, P. Harris, S. Patel, M. Matthews, D. Hawkins, S. G. Alcock, T. Richter, J. J. Mudd, M. Basham, L. Pratt, P. Leicester, E. C. Longhi, A. Tamai and F. Baumberger, *Rev. Sci. Instrum.*, 2017, **88**, 013106.

[137] H. Wang, P. Bencok, P. Steadman and E. Longhi, *J. Synchrotron Rad.*, 2012, **19**, 944–948.

[138] S. Sasaki, *Nucl. Inst. Methods Phys. Res. A*, 1994, **347**, 83–86.

[139] X. Chen, P. Dai, D. Feng, T. Xiang and F. C. Zhang, *Natl. Sci. Rev.*, 2014, **1**, 371–395.

[140] F. Ma, W. Ji, J. Hu, Z.-Y. Lu and T. Xiang, *Phys. Rev. Lett.*, 2009, **102**, 177003.

[141] A. Subedi, L. Zhang, D. J. Singh and M. H. Du, *Phys. Rev. B*, 2008, **78**, 134514.

[142] H. Eschrig and K. Koepernik, *Phys. Rev. B*, 2009, **80**, 104503.

[143] E. M. Nica, R. Yu and Q. Si, *Phys. Rev. B*, 2015, **92**, 174520.

[144] L. C. Rhodes, M. D. Watson, A. A. Haghighirad, M. Eschrig and T. K. Kim, *Phys. Rev. B*, 2017, **95**, 195111.

[145] A. Fedorov, A. Yaresko, T. K. Kim, E. Kushnirenko, E. Haubold, T. Wolf, M. Hoesch, A. Grueneis, B. Buechner and S. V. Borisenko, *Sci. Rep.*, 2016, **6**, 36834.

[146] S. Mukherjee, A. Kreisel, P. Hirschfeld and B. M. Andersen, *Phys. Rev. Lett.*, 2015, **115**, 026402.

[147] V. Brouet, P. H. Lin, Y. Texier, J. Bobroff, A. Taleb-Ibrahimi, P. Le Fèvre, F. Bertran, M. Casula, P. Werner, S. Biermann, F. Rullier-Albenque, A. Forget and D. Colson, *Phys. Rev. Lett.*, 2013, **110**, 167002.

[148] R. S. Dhaka, S. E. Hahn, E. Razzoli, R. Jiang, M. Shi, B. N. Harmon, A. Thaler, S. L. Bud'Ko, P. C. Canfield and A. Kaminski, *Phys. Rev. Lett.*, 2013, **110**, 067002.

[149] M. Abdel-Hafiez, Y. J. Pu, J. Brisbois, R. Peng, D. L. Feng, D. A. Chareev, A. V. Silhanek, C. Krellner, A. N. Vasiliev and X. J. Chen, *Phys. Rev. B*, 2016, **93**, 224508.

[150] A. Heimes, R. Grein and M. Eschrig, *Phys. Rev. Lett.*, 2011, **106**, 047003.

[151] A. Heimes, R. Grein and M. Eschrig, *Phys. Rev. B*, 2012, **86**, 064528.

[152] Y. S. Kushnirenko, A. A. Kordyuk, A. V. Fedorov, E. Haubold, T. Wolf, B. Büchner and S. V. Borisenko, *Phys. Rev. B*, 2017, **96**, 100504.

[153] Y. V. Pustovit, V. V. Bezguba and A. A. Kordyuk, *Metallofiz. Noveishie Tekhnol.*, 2017, **39**, 709–718.

[154] Y. V. Pustovit, V. Brouet, D. Chareev and A. A. Kordyuk, *Metallofiz. Noveishie Tekhnol.*, 2018, **40**, 139–146.

[155] X. Shi, Z.-Q. Han, X.-L. Peng, P. Richard, T. Qian, X.-X. Wu, M.-W. Qiu, S. Wang, J. Hu, Y.-J. Sun and H. Ding, *Nat. Comm.*, 2017, **8**, 14988.

[156] A. E. Böhmer, T. Arai, F. Hardy, T. Hattori, T. Iye, T. Wolf, H. v. Löhneysen, K. Ishida and C. Meingast, *Phys. Rev. Lett.*, 2015, **114**, 027001.

[157] P. O. Sprau, A. Kostin, A. Kreisel, A. E. Böhmer, V. Taufour, P. C. Canfield, S. Mukherjee, P. J. Hirschfeld, B. M. Andersen and J. C. Séamus Davis, *Science*, 2017, **357**, 75–80.

[158] T. Hanaguri, K. Iwaya, Y. Kohsaka, T. Machida, T. Watashige, S. Kasahara, T. Shibauchi and Y. Matsuda, *Science Advances*, 2018, **4**, year.

[159] A. Kostin, P. O. Sprau, A. Kreisel, Y. X. Chong, A. E. Böhmer, P. C. Canfield, P. J. Hirschfeld, B. M. Andersen and J. C. S. Davis, *Nat. Mater.*, 2018.

[160] S.-H. Baek, D. V. Efremov, J. M. Ok, J. S. Kim, J. van den Brink and B. Büchner, *Nat. Mater.*, 2014, **14**, 210–214.

[161] F. Wang, S. A. Kivelson and D.-H. Lee, *Nat Phys*, 2015, **11**, 959–963.

[162] D. Vaknin, *Nat. Mater.*, 2016, **15**, 131–132.

[163] M. D. Watson, A. A. Haghighirad, L. C. Rhodes, M. Hoesch and T. K. Kim, *New J. Phys.*, 2017, **19**, 103021.

[164] E. F. Schwier, H. Takita, W. Mansur, A. Ino, M. Hoesch, M. D. Watson, A. A. Haghighirad and K. Shimada, 2018.

[165] M. D. Watson, A. A. Haghighirad, H. Takita, W. Mansur, H. Iwasawa, E. F. Schwier, A. Ino and M. Hoesch, *J. Phys. Soc. Jpn.*, 2017, **86**, 053703.

[166] Y. Liang, X. Wu and J. Hu, *Chinese Phys. Lett.*, 2015, **32**, 117402.

[167] K. Jiang, J. Hu, H. Ding and Z. Wang, *Phys. Rev. B*, 2016, **93**, 115138.

[168] A. V. Chubukov, M. Khodas and R. M. Fernandes, *Phys. Rev. X*, 2016, **6**, 041045.

[169] J. K. Glasbrenner, I. I. Mazin, H. O. Jeschke, P. J. Hirschfeld and R. Valentí, *Nat. Phys.*, 2015, **11**, 953–958.

[170] J. Kang, R. M. Fernandes and A. Chubukov, *Phys. Rev. Lett.*, 2018, **120**, 267001.

[171] C. Kittel and J. K. Galt, *Solid State Phys.*, 1956, **3**, 437–564.

[172] J.-H. Chu, J. G. Analytis, K. De Greve, P. L. McMahon, Z. Islam, Y. Yamamoto and I. R. Fisher, *Science*, 2010, **329**, 824–826.

[173] M. D. Watson, S. Aswartham, L. C. Rhodes, B. Parrett, H. Iwasawa, M. Hoesch, I. Morozov, B. Büchner and T. K. Kim, *Phys. Rev. B*, 2018, **97**, 035134.

[174] J. D. Wright, T. Lancaster, I. Franke, A. J. Steele, J. S. Möller, M. J. Pitcher, A. J. Corkett, D. R. Parker, D. G. Free, F. L. Pratt, P. J. Baker, S. J. Clarke and S. J. Blundell, *Phys. Rev. B*, 2012, **85**, 054503.

[175] F. Hardy, M. He, L. Wang, T. Wolf, P. Schweiss, M. Merz, M. Barth, P. Adelmann, R. Eder, A.-A. Haghighirad and C. Meingast, *Phys. Rev. B*, 2019, **99**, 035157.

[176] M. D. Watson, T. K. Kim, A. A. Haghighirad, S. F. Blake, N. R. Davies, M. Hoesch, T. Wolf and A. I. Coldea, *Phys. Rev. B*, 2015, **92**, 121108.

[177] T. Terashima, N. Kikugawa, A. Kiswandhi, E.-S. Choi, J. S. Brooks, S. Kasahara, T. Watashige, H. Ikeda, T. Shibauchi, Y. Matsuda, T. Wolf, A. E. Böhmer, F. Hardy, C. Meingast, H. v. Löhneysen, M.-T. Suzuki, R. Arita and S. Uji, *Phys. Rev. B*, 2014, **90**, 144517.

[178] H. Pfau, C. R. Rotundu, J. C. Palmstrom, S. D. Chen, M. Hashimoto, D. Lu, A. F. Kemper, I. R. Fisher and Z.-X. Shen, *Phys. Rev. B*, 2019, **99**, 035118.

[179] M. S. Ikeda, T. Worasaran, J. C. Palmstrom, J. A. W. Straquadine, P. Walmsley and I. R. Fisher, *Phys. Rev. B*, 2018, **98**, 245133.

[180] L. Fanfarillo, J. Mansart, P. Toulemonde, H. Cercellier, P. Le Fèvre, F. Bertran, B. Valenzuela, L. Benfatto and V. Brouet, *Phys. Rev. B*, 2016, **94**, 155138.

[181] L. Benfatto, B. Valenzuela and L. Fanfarillo, *npj Quantum Materials*, 2018, 56.

[182] Y. Yamakawa and H. Kontani, *Phys. Rev. B*, 2017, **96**, 045130.

[183] H. Hu, R. Yu, E. M. Nica, J.-X. Zhu and Q. Si, *Phys. Rev. B*, 2018, **98**, 220503.

[184] J. Bardeen, *Phys. Rev. Lett.*, 1961, **6**, 57–59.

[185] A. J. Macdonald, Y.-S. Tremblay-Johnston, S. Grothe, S. Chi, P. Dosanjh, S. Johnston and S. A. Burke, *Nanotechnology*, 2016, **27**, 414004.

[186] P. Reiss, M. D. Watson, T. K. Kim, A. A. Haghighirad, D. N. Woodruff, M. Bruma, S. J. Clarke and A. I. Coldea, *Phys. Rev. B*, 2017, **96**, 121103.

[187] J. Paglione and R. L. Greene, *Nat. Phys.*, 2010, **6**, 645–658.

[188] D. S. Inosov, J. T. Park, P. Bourges, D. L. Sun, Y. Sidis, A. Schneidewind, K. Hradil, D. Haug, C. T. Lin, B. Keimer and V. Hinkov, *Nat. Phys.*, 2010, **6**, 178–181.

[189] M. Ma, P. Bourges, Y. Sidis, Y. Xu, S. Li, B. Hu, J. Li, F. Wang and Y. Li, *Phys. Rev. X*, 2017, **7**, 021025.

[190] P. J. Hirschfeld, D. Altenfeld, I. Eremin and I. I. Mazin, *Phys. Rev. B*, 2015, **92**, 184513.

[191] Y. Zhang, C. He, Z. R. Ye, J. Jiang, F. Chen, M. Xu, Q. Q. Ge, B. P. Xie, J. Wei, M. Aeschlimann, X. Y. Cui, M. Shi, J. P. Hu and D. L. Feng, *Phys. Rev. B*, 2012, **85**, 085121.

[192] D. V. Evtushinsky, A. A. Kordyuk, V. B. Zabolotnyy, D. S. Inosov, T. K. Kim, B. Büchner, H. Luo, Z. Wang, H.-H. Wen, G. Sun, C. Lin and S. V. Borisenko, *Journal of the Physical Society of Japan*, 2011, **80**, 023710.

[193] H. C. Xu, X. H. Niu, D. F. Xu, J. Jiang, Q. Yao, Q. Y. Chen, Q. Song, M. Abdel-Hafiez, D. A. Chareev, A. N. Vasiliev, Q. S. Wang, H. L. Wo, J. Zhao, R. Peng and D. L. Feng, *Phys. Rev. Lett.*, 2016, **117**, 157003.

[194] D. Liu, C. Li, J. Huang, B. Lei, L. Wang, X. Wu, B. Shen, Q. Gao, Y. Zhang, X. Liu, Y. Hu, Y. Xu, A. Liang, J. Liu, P. Ai, L. Zhao, S. He, L. Yu, G. Liu, Y. Mao, X. Dong, X. Jia, F. Zhang, S. Zhang, F. Yang, Z. Wang, Q. Peng, Y. Shi, J. Hu, T. Xiang, X. Chen, Z. Xu, C. Chen and X. J. Zhou, *Phys. Rev. X*, 2018, **8**, 031033.

[195] T. Hashimoto, Y. Ota, H. Q. Yamamoto, Y. Suzuki, T. Shimojima, S. Watanabe, C. Chen, S. Kasahara, Y. Matsuda, T. Shibauchi, K. Okazaki and S. Shin, *Nat. Commun.*, 2018, **9**, 282.

[196] Y. S. Kushnirenko, A. V. Fedorov, E. Haubold, S. Thirupathaiah, T. Wolf, S. Aswartham, I. Morozov, T. K. Kim, B. Büchner and S. V. Borisenko, *Phys. Rev. B*, 2018, **97**, 180501.

[197] N. E. Bickers and D. J. Scalapino, *Ann. of Phys.*, 1989, **193**, 206–251.

[198] K. Matsuura, Y. Mizukami, Y. Arai, Y. Sugimura, N. Maejima, A. Machida, T. Watanuki, T. Fukuda, T. Yajima, Z. Hiroi, K. Y. Yip, Y. C. Chan, Q. Niu, S. Hosoi, K. Ishida, K. Mukasa, T. Watashige, S. Kasahara, J. G. Cheng, S. K. Goh, Y. Matsuda, Y. Uwatoko and T. Shibauchi, *Nat. Comm.*, 2017, **8**, 1143.

[199] O. V. Dolgov, I. I. Mazin, D. Parker and A. A. Golubov, *Phys. Rev. B*, 2009, **79**, 060502.

[200] C. Wang, L. Li, S. Chi, Z. Zhu, Z. Ren, Y. Li, Y. Wang, X. Lin, Y. Luo, S. Jiang, X. Xu, G. Cao and Z. Xu, *A Lett. J. Explor. Front. Phys.*, 2008, **67006**, 4.

[201] A. V. Chubukov, I. Eremin and M. M. Korshunov, *Phys. Rev. B*, 2009, **79**, 220501.

[202] H. Kontani, in *Transport Phenomena in Strongly Correlated Fermi Liquids*, Springer, 2013, ch. 2, pp. 15–27.

[203] M. M. Korshunov, in *Perturbation Theory: Advances in Research and Applications*, ed. Z. Pirogov, Nova Science Publishers Inc., New York, 2018, ch. 2, pp. 61–138.